Ultrafast Dynamics of Water in Aqueous Solutions Studied Through Ultrafast Optical Kerr Effect

Kamila Mazur

School of Chemistry

University of East Anglia

Norwich

UK

2011

A thesis submitted in partial fulfilment of the requirements for the degree of Doctor of Philosophy of the University of East Anglia.

Declaration

I declare that the work contained in this thesis submitted by me for the degree of Doctor of Philosophy is my work, except where due reference is made to other authors, and has not previously been submitted by me for a degree at this or any other university.

Kamila Mazur

Acknowledgment

First of all, I would like to thank my supervisor Prof. Steve Meech for giving me this opportunity. I am grateful for his constant support, encouragement and guidance. I also thank Dr Ismael Heisler for building the DOE-OKE experimental set up and writing LabVIEW programs for data analysis. I appreciate his help and support during my time at UEA.

I also thank Prof. David Andrews for his advice as my second supervisor.

Thank you to the wonderful members of the Meech research group, past and present: Ismael, Jamie, Andras, Leo, Minako and Kiri for their hospitality and friendship. I also thank Prof. Keisuke Tominaga and Sayuri Yamaguchi for their cooperation.

My infinite thanks to my family, especially my parents for their encouragement and support.

Finally, I would like to thank University of East Anglia for my scholarship.

Abstract

It is established that interfacial water differs from bulk water in a number of ways. To gain a new perspective on interfacial water, its dynamics in the hydration shells of a variety of molecules, from simple ions to complex proteins, have been investigated by means of ultrafast optical Kerr effect (OKE) spectroscopy. The OKE reveals both structural information (spectra) and picosecond relaxation dynamics.

A number of hydrophilic and amphiphilic solutes in aqueous solutions were studied including simple molecules, peptides and proteins. Two different concentration regimes were observed. At the low solute concentration, when there are more than two hydration shells per solute, the tetrahedral structure of water was largely preserved. However, the water dynamics were significantly retarded compared to bulk water. A two state model was applied to separate bulk water from hydration water dynamics. It was found that the hydrophilic solutes slowed down water dynamics to a greater extent than hydrophobic ones.

In more concentrated solutions, where there were insufficient waters to form one complete solvation shell, the water structure was perturbed and the picosecond relaxation times were long. This may reflect slow dynamics for water molecules shared between solute solvation shells. However, at these high concentrations the solutes themselves might contribute to the observed signal. A new mode at ~ 90 cm^{-1} was found in solutions with amide bonds. This mode is associated with an out of plane bend of the H-bonded solute.

Aqueous salt solutions revealed a low frequency mode associated with a symmetric H-bond stretch of water-anion complexes. The increase in frequency of this mode with increasing concentration was associated with cation charge, indicating cooperative effects. The studies also revealed that the Cl^- disrupts the water structure much less than the relatively large I^-.

Contents

Abbreviations

OKE	Optical Kerr Effect
LO	local oscillator
R_{OKE}	material response function
α	isotropic part of the polarizability
β	anisotropic part of the polarizability
$<\tau>$	average relaxation time
$D(\omega)$	spectral density
BL	Bucaro-Litovitz function
ASG	antisymmetrized Gaussian function
G	Gaussian function
n_{sw}	molar ratio
FA	formamide
UA	urea
TMAO	trimethylamine N-oxide
TMU	tetramethylurea
TBA	tert-butanol
NAGMA	N-acetyl-glycine-methylamine
NALMA	N-acetyl-leucine-methylamine
NAAMA	N-acetyl-alanine-methylamine

Chapter 1

Introduction

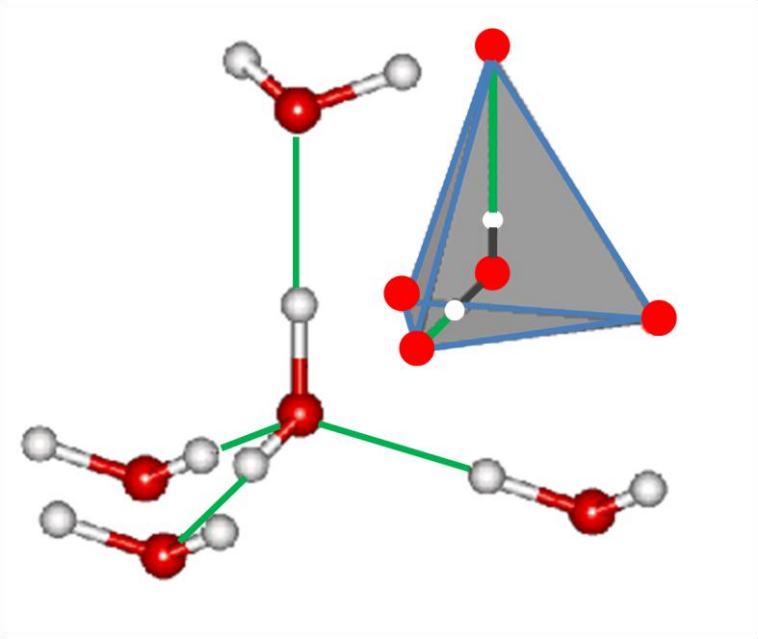

Figure 1.1 Tetrahedral structure of water

Water is the most ubiquitous liquid on Earth. It covers more than 70 % of the Earth's surface. A significant fraction of the human body (>60%) is water. It can exist in three states of matter: ice, liquid and vapour, and ice can adapt many crystalline forms. Due to its ability to form H-bonds water has a number of anomalous properties: decrease of viscosity with pressure, large heat capacity, melting with pressure among many others.[1, 2] One of the most interesting properties is the density maximum at 4 ºC. This maximum can be thought of as resulting from the competition of an ordered ice like

structure with a disordered liquid structure. Below 4 ºC the ice like structure starts to dominate and above the liquid structure is dominant.[3]

Water molecules form an extended three dimensional hydrogen bond network. This network is highly dynamic as H-bonds break, form and stretch on the picosecond timescale.[4] It is known that in the ice like I_h (hexagonal form) a water molecule is H-bonded to four other water molecules in a tetrahedral arrangement (Figure 1.1), with each central water molecule acting as a double acceptor (oxygen having two lone pairs) and double donor (hydrogen). In the liquid phase the tetrahedral structure is largely preserved. However it acquires some degree of disorder as revealed by neutron diffraction and X-ray data.[5-7] Thermodynamic studies showed that approximately 13 % of hydrogen bonds are broken upon transition from ice to a liquid structure.[8] However, in the last decade some new studies appeared which challenged the existence of a tetrahedral structure of water.[9-11] Nilsson *et al.*[9-11] using X-ray absorption and Raman spectroscopy (XAS and XRS) together with studies modelling core electron excitations concluded that the water network is composed mainly from strongly hydrogen bonded chains or rings. This interpretation was strongly criticized by Soper[12] and Head-Gordon *et al.*[13] Soper[12] argued that interpretation of the data supported by computer spectra presented by Nilsson *et al*.[9] is not correct. Three other groups used XRS and X-ray emission spectroscopy (XES) to study liquid water[14-16] and found no evidence for the water chain structure. The XES studies showed that the region that was associated with chain structure by Nilsson *et al.*[9] is in fact dominated by three- hydrogen bonded species not two as in the chain structure.

Water has been a subject of extensive studies, but despite such large interest, the structural and dynamical properties of water, in particular in the presence of a solute, are still not fully understood.[3, 17-31] It is now established that water actively engages

and interacts with biomolecules, e.g. membranes, proteins in a number of ways. Water molecules, by forming directional, weak bonding allow the reorientation and reconfiguration of the protein's three dimensional structure.[3] Water not only governs the structure and dynamics of biomolecules, but also their function and stability.[3, 28] Hydrophobic and hydrophilic interactions were especially widely studied. From these studies different interpretations and models emerged.[32, 33] For example Bakker *et al.*[34] using midinfrared pump-probe spectroscopy suggested that water in the vicinity of hydrophobic groups is immobilized, whereas no immobilized water molecules were found in molecular dynamics simulations by the group of Laage *et al.*[35] This disagreement is significant as the structure and dynamics of water near hydrophobic and hydrophilic residues is critical in the mechanism of protein folding (details in Chapters 2 and 4).

In this work structural and dynamical properties of water are investigated in aqueous solutions of a broad range of solutes, from purely hydrophilic molecules through peptides and proteins to the almost entirely hydrophobic tert-butanol. The experimental technique used is ultrafast Optical Kerr Effect spectroscopy (OKE). OKE is a nonlinear four wave mixing spectroscopy which implements femtosecond pulses to study molecular dynamics through polarizability relaxation. It has been widely applied to study the liquid state for almost 30 years.[36-56] It was successfully used to study water dynamics by Vohringer *et al.*[50, 51] and Righini *et al.*[52] and protein solutions by Wynne *et al.*[36, 37] and Tokmakoff *et al.*[56] Different experimental geometries are used to access the anisotropic and isotropic response of the sample.[41, 42, 55] In this work the conventional pump-probe geometry with optical heterodyne detection (OHD-OKE) is employed to study the anisotropic signal.[53, 55] To access the

isotropic component of the signal, the diffractive optic element transient grating geometry was implemented (DOE-OKE).[42]

1.1 Thesis Overview

Experimental and theoretical conditions required for the OKE spectroscopy are described in **Chapter 2**. The two experimental set ups used in this study are described: (1) OHD-OKE using the pump-probe geometry and (2) TG-OKE based on the diffractive optic element. These two experiments are used to measure the anisotropic and isotropic response, respectively. The data analysis procedures are explained using pure liquid water as an example. In **Chapter 3** both the anisotropic and isotropic responses of salt solutions are described. This chapter is based on the publication: *Heisler, I.A.; Mazur, K.; Meech, S.R.; 2011, Low-Frequency Modes of Aqueous Alkali Halide Solutions: An Ultrafast Optical Kerr Effect Study, Journal of Physical Chemistry B, 115, 1863-1873.* In **Chapter 4** the anisotropic response of five simple solutes is analysed. A two-state hydration model for dilute solutions is described. The different effect of hydrophobic and hydrophilic interactions on the response are described. This chapter is based on the publication: *Mazur, K.; Heisler, I.A.; Meech, S.R.; 2011, THz Spectra and Dynamics of Aqueous Solutions Studied by the Ultrafast Optical Kerr Effect, Journal of Physical Chemistry B, 115, 2563-2573.* In **Chapter 5** solutions of three model peptides are described. Particular attention was paid to water behaviour in the vicinity of hydrophilic and hydrophobic moieties. This chapter is based on the publication: *Mazur, K.; Heisler, I.A.; Meech, S.R.; 2010, Ultrafast Dynamics and Hydrogen-Bond Structure in Aqueous Solutions of Model Peptides, Journal of Physical Chemistry B, 114, 10684-10691.* The aqueous solutions of three globular proteins are analysed in **Chapter 6**. The water dynamics observed

are correlated with surface hydrophobicity of the protein. This chapter is based on the paper: *Mazur, K.; Heisler, I.A.; Meech, S.R.; Water dynamics at protein interfaces: Ultrafast Optical Kerr effect study*, which is accepted for publication in the Journal of Physical Chemistry A.

1.2 References

1. D. Eisenberg and W. Kauzmann, *The Structures and Properties of Water*, Oxford: London, 1969.
2. H. E. Stanley and O. Mishima, *Nature*, 1998, **396**, 329-335.
3. P. Ball, *Chem. Rev.*, 2008, **108**, 74-108.
4. I. Ohmine and S. Saito, *Acc. Chem. Res.*, 1999, **32**, 741-749.
5. J. C. Dore, *J. Mol. Struct.*, 1991, **250**, 193-211.
6. A. H. Narten, W. E. Thiessen and L. Blum, *Science*, 1982, **217**, 1033-1034.
7. P. G. Kusalik and I. M. Svishchev, *Science*, 1994, **265**, 1219-1221.
8. S. W. Benson and E. D. Siebert, *J. Am. Chem. Soc.*, 1992, **114**, 4269-4276.
9. A. Nilsson, P. Wernet, D. Nordlund, U. Bergmann, M. Cavalleri, M. Odelius, H. Ogasawara, L. A. Naslund, T. K. Hirsch, L. Ojamae, P. Glatzel and L. G. M. Pettersson, *Science*, 2004, **304**, 995-999.
10. L. G. M. Pettersson, M. Leetmaa, K. T. Wikfeldt, M. P. Ljungberg, M. Odelius, J. Swenson and A. Nilsson, *J. Chem. Phys.*, 2008, **129**.
11. A. Nilsson, C. Huang, K. T. Wikfeldt, T. Tokushima, D. Nordlund, Y. Harada, U. Bergmann, M. Niebuhr, T. M. Weiss, Y. Horikawa, M. Leetmaa, M. P. Ljungberg, O. Takahashi, A. Lenz, L. Ojamae, A. P. Lyubartsev, S. Shin and L. G. M. Pettersson, *P. Natl. Acad. Sci. USA*, 2009, **106**, 15214-15218.
12. A. K. Soper, *Pure Appl. Chem.*, 2010, **82**, 1855-1867.
13. T. Head-Gordon and M. E. Johnson, *P. Natl. Acad. Sci. USA*, 2006, **103**, 7973-7977.
14. D. T. Bowron, M. H. Krisch, A. C. Barnes, J. L. Finney, A. Kaprolat and M. Lorenzen, *Physical Review B*, 2000, **62**, R9223-R9227.
15. P. Feulner, R. Romberg, S. P. Frigo, R. Weimar, M. Gsell, A. Ogurtsov and D. Menzel, *Surf. Sci.*, 2000, **451**, 41-52.
16. J. H. Guo, Y. Luo, A. Augustsson, J. E. Rubensson, C. Sathe, H. Agren, H. Siegbahn and J. Nordgren, *Phys. Rev. Lett.*, 2002, **89**, 137402.
17. A. R. Bizzarri and S. Cannistraro, *J. Phys. Chem. B*, 2002, **106**, 6617-6633.
18. B. Born, H. Weingartner, E. Brundermann and M. Havenith, *J. Am. Chem. Soc.*, 2009, **131**, 3752-3755.
19. I. Brovchenko and A. Oleinikova, *Chemphyschem*, 2008, **9**, 2695-2702.
20. M. F. Colombo, D. C. Rau and V. A. Parsegian, *Science*, 1992, **256**, 655-659.

21. L. P. DeFlores and A. Tokmakoff, *J. Am. Chem. Soc.*, 2006, **128**, 16520-16521.
22. S. Ebbinghaus, S. J. Kim, M. Heyden, X. Yu, U. Heugen, M. Gruebele, D. M. Leitner and M. Havenith, *P. Natl. Acad. Sci. USA*, 2007, **104**, 20749-20752.
23. B. Halle, *Philosophical Transactions of the Royal Society of London Series B-Biological Sciences*, 2004, **359**, 1207-1223.
24. K. Hallenga, J. R. Grigera and H. J. C. Berendsen, *J. Phys. Chem.*, 1980, **84**, 2381-2390.
25. V. Helms, *Chemphyschem*, 2007, **8**, 23-33.
26. M. Heyden and M. Havenith, *Methods*, 2010, **52**, 74-83.
27. M. E. Johnson, C. Malardier-Jugroot and T. Head-Gordon, *Phys Chem Chem Phys*, 2010, **12**, 393-405.
28. I. D. Kuntz and W. Kauzmann, *Adv. Protein Chem.*, 1974, **28**, 239-345.
29. G. A. Papoian, J. Ulander, M. P. Eastwood, Z. Luthey-Schulten and P. G. Wolynes, *P. Natl. Acad. Sci. USA*, 2004, **101**, 3352-3357.
30. J. Qvist and B. Halle, *J. Am. Chem. Soc.*, 2008, **130**, 10345-10353.
31. J. Qvist, E. Persson, C. Mattea and B. Halle, *Faraday Discuss.*, 2009, **141**, 131-144.
32. A. D. J. Haymet, N. T. Southall and K. A. Dill, *J. Phys. Chem. B*, 2002, **106**, 521-533.
33. L. R. Pratt, *Annu. Rev. Phys. Chem.*, 2002, **53**, 409-436.
34. Y. L. A. Rezus and H. J. Bakker, *Phys. Rev. Lett.*, 2007, **99**, 148301.
35. D. Laage, G. Stirnemann and J. T. Hynes, *J Phys Chem* 2009, **113**, 2428-2435.
36. G. Giraud, J. Karolin and K. Wynne, *Biophys. J.*, 2003, **85**, 1903-1913.
37. N. T. Hunt, L. Kattner, R. P. Shanks and K. Wynne, *J. Am. Chem. Soc.*, 2007, **129**, 3168-3172.
38. E. W. Castner, Y. J. Chang, Y. C. Chu and G. E. Walrafen, *J. Chem. Phys.*, 1995, **102**, 653-659.
39. Y. J. Chang and E. W. Castner, *J. Chem. Phys.*, 1993, **99**, 113-125.
40. Y. J. Chang and E. W. Castner, *J. Phys. Chem.*, 1994, **98**, 9712-9722.
41. C. J. Fecko, J. D. Eaves and A. Tokmakoff, *J Chem Phys*, 2002, **117**, 1139-1154.
42. G. D. Goodno, G. Dadusc and R. J. D. Miller, *Journal of the Optical Society of America B-Optical Physics*, 1998, **15**, 1791-1794.
43. G. D. Goodno and R. J. D. Miller, *J. Phys. Chem. A*, 1999, **103**, 10619-10629.
44. N. T. Hunt, A. A. Jaye and S. R. Meech, *PCCP*, 2007, **9**, 2167-2180.
45. N. T. Hunt, A. R. Turner, H. Tanaka and K. Wynne, *J. Phys. Chem. B*, 2007, **111**, 9634-9643.
46. H. Shirota, T. Fujisawa, H. Fukazawa and K. Nishikawa, *Bull. Chem. Soc. Jpn.*, 2009, **82**, 1347-1366.
47. H. Shirota and H. Ushiyama, *J. Phys. Chem. B*, 2008, **112**, 13542-13551.
48. D. A. Turton, J. Hunger, G. Hefter, R. Buchner and K. Wynne, *J. Chem. Phys.*, 2008, **128**, 161102.
49. D. A. Turton and K. Wynne, *J. Chem. Phys.*, 2009, **131**, 201101.

50. K. Winkler, J. Lindner, H. Bursing and P. Vohringer, *J. Chem. Phys.*, 2000, **113**, 4674-4682.
51. K. Winkler, J. Lindner and P. Vohringer, *PCCP*, 2002, **4**, 2144-2155.
52. R. Torre, P. Bartolini and R. Righini, *Nature*, 2004, **428**, 296-299.
53. N. A. Smith and S. R. Meech, *Int. Rev. Phys. Chem.*, 2002, **21**, 75-100.
54. W. T. Lotshaw, D. McMorrow, N. Thantu, J. S. Melinger and R. Kitchenham, *J. Raman Spectrosc.*, 1995, **26**, 571-583.
55. D. McMorrow, W. T. Lotshaw and G. A. Kenneywallace, *IEEE J Quantum Elect*, 1988, **24**, 443-454.
56. J. D. Eaves, C. J. Fecko, A. L. Stevens, P. Peng and A. Tokmakoff, *Chem. Phys. Lett.*, 2003, **376**, 20-25.

Chapter 2

Polarization Resolved Optical Kerr Effect Spectroscopy

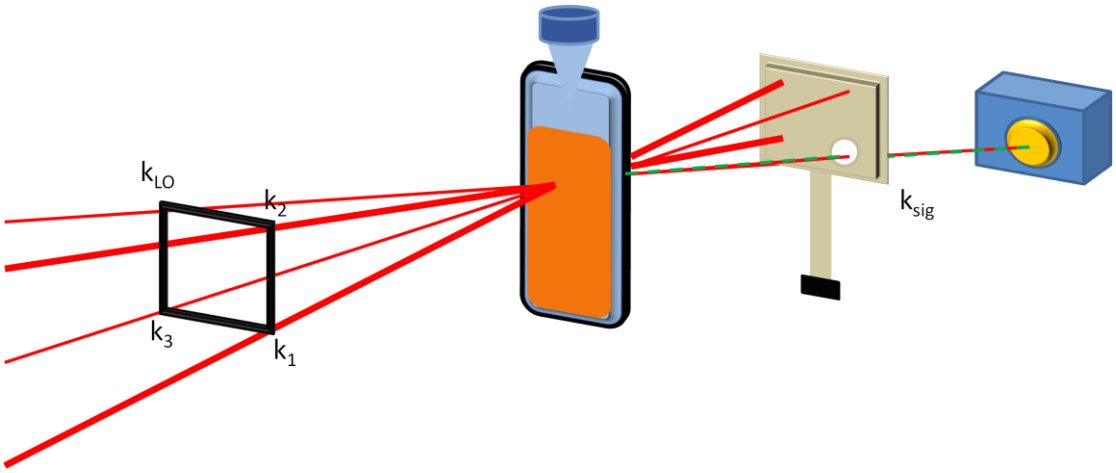

The earliest ultrafast OKE spectroscopy was performed by Farrow *et al.* in 1984.[1] Since then it was used successfully by many groups to study the ultrafast dynamics of a great variety of samples.[2-11] In this chapter the principles of OKE spectroscopy are outlined. Two experimental set-ups, OHD-OKE and DOE-OKE are described. The former is used to access the anisotropic depolarized part of the polarizability response function and the latter to access the isotropic polarized part. The procedure for analysing the data is explained using as an example the response of liquid water, which serves to illustrate the methods and is the basis for later studies of aqueous solutions.

2.1. Introduction

The optical Kerr effect is a nonlinear optical phenomenon occurring when intense light propagating through a medium results in a modification of the refractive index. This effect arises from deformation of electronic orbitals of atoms or molecules or, for gases and liquids, from molecular reorientation in the field. The net polarization, P induced in the medium by a strong electric field of frequency ω, E_ω may in general be given:

$$P = \varepsilon_0 \left(\chi^{(1)} + \chi^{(2)} |E_\omega| + \chi^3 |E_\omega|^2 + \cdots \right) E_\omega \cos(\omega t) \qquad (2.1)$$

where ε_0 is the free space permittivity and $\chi^{(n)}$ is the n-th order susceptibility. The first term denotes linear polarization and describes linear absorption and emission. Isotropic media, like liquids, posses a centre of symmetry, thus under the parity transformation $P \to -P$ and $E_\omega \to -E_\omega$ all even orders of susceptibility must vanish ($\chi^{(2)} = 0$). Therefore the second term in liquids is equal to zero. The third term leads to a change in the refractive index of the medium proportional to the square of the applied electric field.

In general the refractive index, *n*, of the medium can be written in terms of the susceptibility: $n = \sqrt{1+\chi_{TOT}}$, where $\chi_{TOT} = \chi^{(1)} + \chi^{(3)}|E_\omega|^2$, therefore:

$$n = \sqrt{1+\chi^{(1)}+\chi^{(3)}|E_\omega|^2} = \sqrt{n_0^2+\chi^{(3)}|E_\omega|^2} = n_0\sqrt{1+\frac{\chi^{(3)}|E_\omega|^2}{n_0^2}} \qquad (2.2)$$

and using the Taylor series $\sqrt{1+x} = 1+\frac{1}{2}x-\frac{1}{8}x^2+\frac{1}{16}x^3+\cdots$, the following relation was obtained:

$$n = n_0 + \frac{\chi^{(3)}}{2n_0}|E_\omega|^2 = n_0 + n_2 I \qquad (2.3)$$

where $\chi^{(3)}/2n_0$ is n_2, n_0 is the linear refractive index, which is time independent and *I* is the time averaged intensity of the optical field. In cases where only the time dependent part of the refractive index is relevant, $n_2 \propto \chi^{(3)}$.

The quantity $\chi^{(3)}$ is a 4th rank tensor. It possesses 81 elements, but due to the symmetry of the isotropic liquid medium only 21 are nonzero.[12] Four of these elements include the description of third order polarization in the sample:[13] χ_{ZYYZ}, χ_{ZZZZ}, χ_{ZZYY} and χ_{ZYZY}, where z and y are the direction of polarization and the light beam is assumed to propagate along x. Three of these elements are independent: $\chi_{ZZZZ} = \chi_{ZZYY} + \chi_{ZYZY} + \chi_{ZYYZ}$. For the Raman experiments, the symmetry to interchange of indices yields the relationship: $\chi_{ZYZY} = \chi_{ZYYZ;}$ the remaining 17 elements might be obtained by permutation of χ indices.[14] See below for details on relevance of various tensor elements.

The refractive index in general can also be written in a complex form: $n^* = n + i\kappa$, where the imaginary part, κ, indicates absorption loss (dichroism) when the

electromagnetic field propagates through the medium. The OKE measurement performed here is, however, a non-resonant experiment and therefore the absorption contribution to the change of the refractive index is negligible.

OKE spectroscopy belongs to a family of third order nonlinear spectroscopies like coherent antiStokes Raman spectroscopy (CARS) or general four wave mixing techniques.

2.2 Optically Heterodyne Detected Optical Kerr Effect Spectroscopy (OHD-OKE)

2.2.1 Experimental Set-Up

OKE is a pump-probe spectroscopy. Both pump and probe pulses originate from the same source and have the same frequency. The source used here was a home built Ti:Sapphire laser based on a non symmetrical two-folded cavity[15] and pumped with a Nd:YVO_4 laser (Coherent Verdi, λ = 532nm, pumping power = 5W). Generated pulses had a 220 mW average power and were centred at ~815 nm. The repetition rate was 68 MHz and the energy per pulse 3.3 nJ. The intensity autocorrelation measured at the sample position gave a value for the pulse FWHM of 54 fs yielding a pulse duration of 40 fs. After dispersion compression by a prism pair; assuming a Gaussian lineshape, the time-bandwidth product is ~ 0.5. The scheme of the OHD-OKE set-up is shown in Figure 2.1. The output of the laser is divided into two beams with a beam splitter (Newport, 10RQ00UB.2): pump and probe. The pump carries 80% of the fundamental beam intensity while the probe has 20%. The pump is directed onto a delay stage (PI, M-505.4DG, design resolution 0.0164µm/count), which controls the time separation between the pulses. Both beams are polarized at 45º relative to each other. A lens (10 cm focal length) is introduced to focus the pump and probe beams

(to a common spot) into the sample. The strong pump enters the sample first and induces a birefringence in the initially isotropic sample by distorting the electron clouds of molecules. This leads to an electronic response. The pump also induces a torque on molecules with induced dipole moment, causing the molecules to tend to align with the field, in such a way as to have their most polarizable axis along the pump polarization vector. The probe beam, which is not strong enough to induce nonlinear response on its own, enters the sample at different time delays and probes

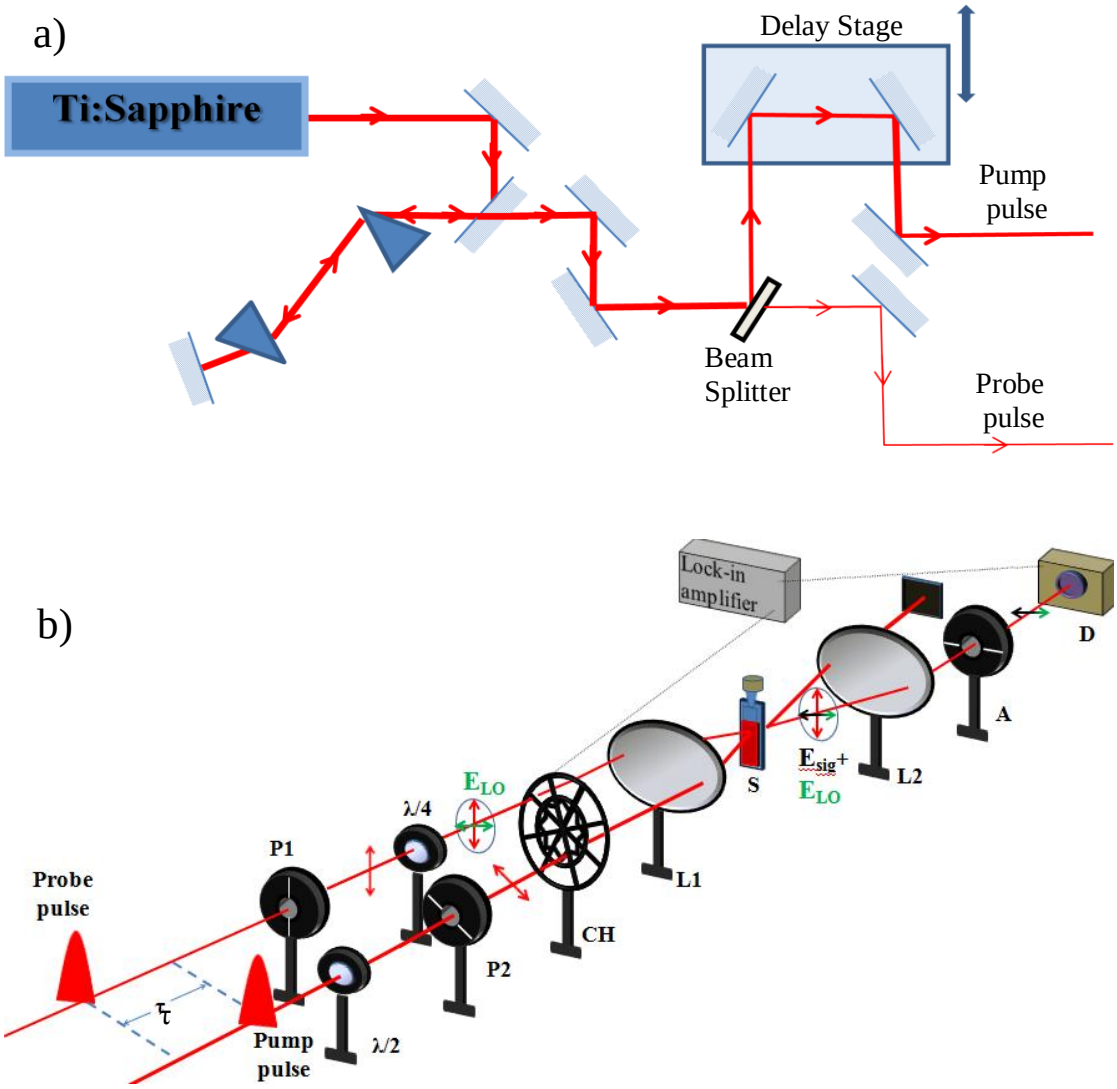

Figure 2.1 Experimental set-up for the OHD-OKE experiment. P denotes polarizer, CH-chopper, L-lens, S-sample, A-analyser, D-detector, λ/4-quarter wave plate. τ is a delay time between pump and probe pulses.

the induced birefringence at that time. Its projected components (parallel and perpendicular to the pump polarization direction) experience a phase difference due to birefringence[16] as they propagate through the sample resulting in a change of the output polarization from linear to elliptical. The depolarized part of the signal is 90º out of phase with the original polarization of the probe. The analyser (Karl Lambrecht Corporation, Glan-Thompson MGT25A8), which is placed in the signal pathway, is crossed with the probe polarizer (Karl Lambrecht Corporation, Glan-Thompson MGT25A8) and as a result only depolarized light is detected on the photodiode. This description is consistent with a homodyne detection scheme. In order to achieve both signal amplification and linearization, heterodyne detection is implemented[5, 17] by inserting a quarter-wave plate (λ/4, Bernhard Halle) in the probe pathway aligned in such a manner to have its fast axis aligned with the probe polarization direction. In heterodyne detection the signal is superimposed with an extra field, called local oscillator, on the detector. If the probe polarizer is rotated by a small angle, θ (typically one to three degrees in either direction), the fast axis of the λ/4 polarizer is no longer aligned with probe polarization (P2, Figure 2.1). Thus the λ/4 generates a small out of phase component (LO) that is, a slightly elliptical probe polarization. As a consequence of this rotation some light leaks through the analyser and reaches the photodiode. This leakage is 90^0 out of phase with the rest of the probe and in phase with the OKE signal. Both LO contribution and signal are detected after the analyser. To eliminate the strong contribution which comes explicitly from the LO, lock in detection is implemented. In this technique a mechanical chopper is inserted into both beams in such a manner that the pump passes through the inner ring and the probe through the outer, Figure 2.1. The chopper interrupts each beam with a different frequency. The lock-in amplifier (SR830 Stanford Research) which is connected to a

detector is set to register only the signal which appears at the sum of the chopping frequencies. Therefore the LO which has the same chopping frequency as the probe beam is discarded. Due to lock in detection the signal has very good signal to noise ratio and its heterodyne term is linear. Details will be given in section 2.2.3.

2.2.2 Connection to Stimulated Raman Scattering

The OHD-OKE technique is also called Raman induced Kerr effect spectroscopy (RIKES) as origin of the change in refractive index arises through the molecular polarizability through the Raman interaction process.

In the Figure 2.2a the energy conservation diagram for OKE/RIKES for a single excitation is depicted. The v_1 and v_2 represent Raman vibrational or librational levels of the ground state. The dashed line represents the virtual state, created by the laser interacting with electrons. Two laser fields at wavenumbers ω_{pu1} and ω_{pu2}, both from the pump beam, are applied to the sample. If $\left|\omega_{pu1} - \omega_{pu2}\right|$ is on resonance with a vibrational or librational mode of the material coherent excitation of Raman mode is achieved. The probe beam, typically at wavenumber ω_S, then stimulates emission of the signal from this coherent excitation. The intensity of the observed signal is a function of the time separation between pump and probe, τ. Therefore, control of delaying times allows for the mapping out of the time evolution of the vibrational or librational excitation. The net excitation is given by a superposition of all wavenumber combinations $\left|\omega_{pu1} - \omega_{pu2}\right|$, with ω_{pu1} and ω_{pu2} contained within the laser bandwidth, Figure 2.2b. All modes that are associated with a change of polarizability with respect to normal coordinates (changes in the positions of atoms in the molecule) can be excited.

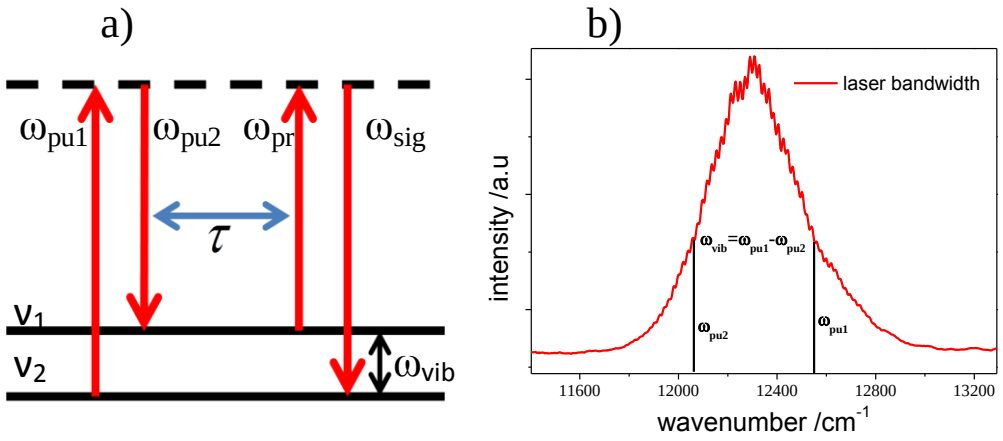

Figure 2.2 a) Excitation mechanism in OKE/RIKES and b) spectrum showing possible excitation frequencies. Centre frequency is 815nm=12270cm^{-1}.

In Figure 2.3 the OKE anisotropic and isotropic response of chloroform in both, time and frequency domain is shown. The time domain response is dominated by an oscillatory feature. These oscillations correspond to modes above 200 cm^{-1} in the frequency domain.

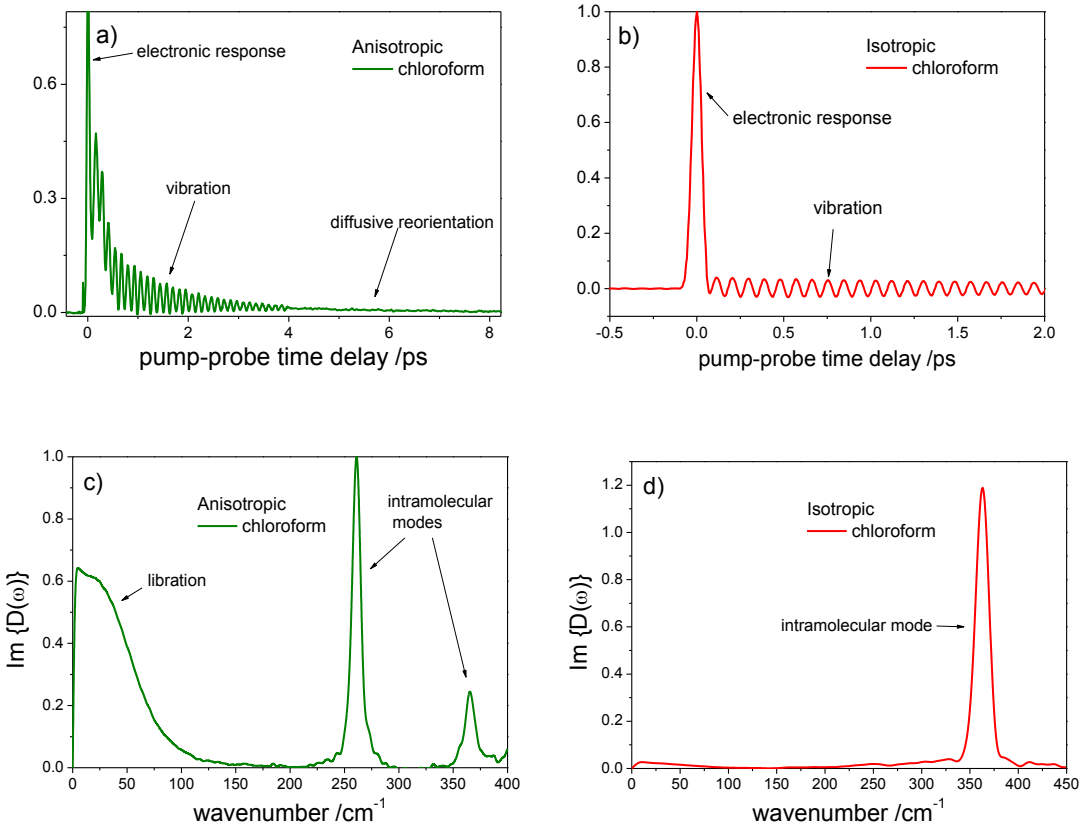

Figure 2.3 a),c) Anisotropic and b),d) isotropic OKE response of neat chloroform.

The pump-probe geometry for the OKE experiments yields the exact phase-matching condition, with signal scattered in the probe direction: $k_{sig} = k_{pu1} - k_{pu2} + k_{pr}$. The phase matching diagram for OHD-OKE experiment is shown in Figure 2.4.

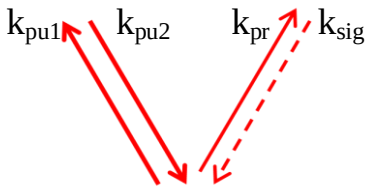

Figure 2.4 Propagation directions in OHD-OKE. k_{pu1}, k_{pu2}, denote pump, k_{pr} probe and k_{sig} signal wavevectors.

2.2.3 Theoretical Description of OKE Spectroscopy

The processes describing field-matter interactions in an OKE experiment can be fully described by nonlinear optics equations and are given in detail in a number of books.[12, 18, 19] Here the principles of OKE response will be described.[17, 20]

The strong pump pulse, which is linearly polarized in the z direction and propagating in the x direction introduces an anisotropic index of refraction in the sample. This change of refractive index is described by Eq. 2.2.

The electric field of probe beam after the sample can be written as:[20]

$$E'_{probe}(t) = E_{probe}(t)\exp\left[i\omega\left(\frac{n_0}{c}x - t\right)\right]\left\{1 + \frac{i\omega n_2(\tau)x}{c} + \ldots\right\} \qquad (2.4)$$

If $|n_2(\tau)| << 1$ the power series expansion in the above equation might be approximated by up to the first order with respect to $n_2(\tau)$. In Eq. 2.4 the first and second term in the braces denote in phase and out of phase components of the probe pulse. Therefore

optical Kerr effect is only responsible for the appearance of the out of phase, $i\omega n_2(\tau)/c$ term.

The nonlinear refractive index can be expressed as:[21]

$$n_2(\tau) \propto \int_{-\infty}^{t} dt' R_{OKE}(\tau - t') I_{pump}(t') \tag{2.5}$$

where I_{pump} is the intensity of the pump pulse and R_{OKE} is the material response function. R_{OKE} is related to nonlinear susceptibility with the relation:

$$R_{OKE} \propto \frac{d}{dt}\chi^{(3)} \tag{2.6}$$

In general the electric field of the probe pulse which is polarized in the analyser direction, Figure 2.5, can be written as:[20]

$$\mathrm{E}_{\psi} = \cos\psi\left\{\mathrm{E}_z(\mathrm{t}-\tau)\mathrm{e}^{\mathrm{i}\omega\left(\frac{\mathrm{n}_0\mathrm{x}}{\mathrm{c}}-\mathrm{t}+\tau\right)}\left[1+\mathrm{i}\left(\frac{\omega\mathrm{x}}{\mathrm{c}}\right)\int_{-\infty}^{\mathrm{t}}\mathrm{dt'R}_{zzzz}(\mathrm{t}-\mathrm{t'})\mathrm{E}_{\mathrm{pump}}(\mathrm{t'})\mathrm{E}_{\mathrm{pump}}(\mathrm{t'})\right]\right\} \tag{2.7}$$

$$+\sin\psi\left\{E_y(t-\tau)e^{i\omega\left(\frac{n_0x}{c}-t+\tau\right)}\left[1+i\left(\frac{\omega x}{c}\right)\int_{-\infty}^{t}dt' R_{zzyy}(t-t')E_{pump}(t')E_{pump}(t')\right]\right\}$$

where ψ is the angle between pump and polarization set on analyser and E_z and E_y are z and y components of the probe electric field and are given by:

$$E_z = E_{probe}(\cos\theta\cos\phi - i\sin\theta\sin\phi) \tag{2.8}$$

$$E_y = E_{probe}(\cos\theta\sin\phi + i\sin\theta\cos\phi) \tag{2.9}$$

where ϕ is the angle between pump and probe polarization and the θ is an angle of rotation of a polarizer from the optic axis of the quarterwave plate in order to introduce local oscillator, (typically <1º) see section 2.2.1 for details. After

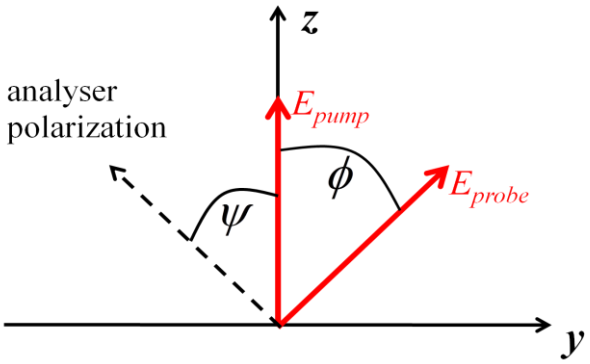

Figure 2.5 Direction of pump and probe polarization.

substituting Eq. 2.9 and 2.8 into 2.7:

$$E_{\psi} = E_p(t-\tau)e^{i\omega\left(\frac{n_0 x}{c}-t+\tau\right)}[\cos\theta\cos(\psi-\phi)+i\sin\theta\sin(\psi-\phi)$$
$$+i\cos\theta\left(\frac{\omega x}{c}\right)\int_{-\infty}^{t}dt' R_{OKE}(t-t')I_e(t')+ \qquad (2.10)$$
$$\sin\theta\left(\frac{\omega x}{c}\right)\int_{-\infty}^{t}dt'[R_{zzzz}(t-t')\sin\phi\cos\psi - R_{ZZYY}(t-t')\cos\phi\sin\psi]I_{pump}(t')]$$

where $R_{OKE}(t) = R_{zzzz}(t)\cos\phi\cos\psi + R_{zzyy}(t)\sin\phi\sin\psi$, Figure 2.5. The intensity after the analyzer for OKE experiment ($\phi = -\psi$):

$$I(\tau) = E_{\psi}E_{\psi}^{*} = \left\langle I_p \sin^2\theta\right\rangle_t + \left\langle\left|E_p(t-\tau)\frac{\omega x}{c}\int_{-\infty}^{t}dt' R_{OKE}(t-t')I_{pump}(t')\right|^2\right\rangle_t$$
$$2\left\langle I_p(t-\tau)\frac{\omega x}{c}\sin\theta\cos\theta\sin(\psi-\phi)\int_{-\infty}^{t}dt' R_{OKE}(t-t')I_{pump}(t')\right\rangle_t \qquad (2.11)$$

The first term in the above equation denotes intensity of the transmitted probe (local oscillator) and is removed from the signal by lock-in detection, Figure 2.1. The second term is the homodyne contribution to the signal. Usually the magnitude of LO is adjusted (by increasing θ) such that the heterodyne signal dominates over the homodyne one. In this case the detected signal is dominated by the third term, which

is the heterodyne term and is of principle interest in OHD-OKE spectroscopy. It contributes to high signal to noise ratio and it is also linear in the intensity which enables conversion of the data by Fourier Transform to the frequency domain.

2.2.3.1 The Response Function

All the information about molecular dynamics in the sample are contained in the third order response function, $R_{OKE}(t)$. $R_{OKE}(t)$ describes the interactions of the electromagnetic field with the sample and how they are modified by the structural and dynamical properties of the medium. In the simplest approximation and in case of the non-resonant OKE experiment, this function can be separated into electronic, R_{OKE}^{el} and nuclear contributions, $R_{OKE}^{nuclear}$ (Born-Oppenheimer approximation):

$$R_{OKE}(t) = R_{OKE}^{el} + R_{OKE}^{nuclear} \tag{2.12}$$

Making use of the Born-Oppenheimer approximation we can describe the material response function, taking only the nuclear contribution into account. In such a case, $R_{OKE}(t)$ is proportional to the first time derivative of the correlation function of the collective system polarizability, Π,[2, 19] ($R_{OKE}^{nuclear}(t) = R_{ijkl}^{(3)}(t)$):

$$R_{ijkl}^{(3)}(t) \propto -\frac{1}{k_B T}\frac{\partial}{\partial t}\left\langle \Pi_{ij}(t)\Pi_{kl}(0)\right\rangle \tag{2.13}$$

where, k_B is the Boltzman constant, T is the temperature and i, j, k, l indicate the components of Π in the laboratory frame (x ,y, z). Angle brackets denote ensemble average.

The response function can be transformed to the frequency domain by Fourier Transform:

$$\chi^{(3)}_{ijkl}(\omega) = \int_0^\infty R_{OKE}(\tau)\exp(i\omega\tau)d\tau \tag{2.14}$$

The imaginary part of $\chi^{(3)}(\omega)$ is the susceptibility, the spectral density for polarizability relaxation. Under the Born-Oppenheimer approximation the third order susceptibility can be written in analogy to Eq. 2.12, using quantum mechanical representation, as follows:

$$\chi^{(3)}_{ijkl} = \sigma_{ijkl} + \frac{iV}{2\hbar}\left\langle[\Pi_{ij}(t),\Pi_{kl}(0)]\right\rangle \tag{2.15}$$

where σ_{ijkl} is the ensemble averaged non-resonant electronic hyperpolarizability and $[\Pi_{ij}(t),\Pi_{kl}(0)]$ is the commutator. The above equation can be related with Eq. 2.13 by fluctuation-dissipation theorem:[19] $\frac{iV}{2\hbar}\left\langle[\Pi_{ij}(t),\Pi_{kl}(0)]\right\rangle \propto -\frac{1}{k_B T}\frac{\partial}{\partial t}\left\langle\Pi_{ij}(t)\Pi_{kl}(0)\right\rangle$.

2.2.3.2 Anisotropic and Isotropic Polarizability

In the condensed phase the collective polarizability is a sum of the individual molecule contributions (M) and interaction-induced contributions (II), which arise from interactions of induced molecular dipoles which modify the polarizability:[4, 22]

$$\Pi(t) = \Pi^M(t) + \Pi^{II}(t). \tag{2.16}$$

where $\Pi^M(t)$ is the sum of the single molecule molecular polarizabilities, $\sum_{n=1}^{N}\boldsymbol{\alpha}_n^M(t)$.

Each molecule has an isotropic, α, and an anisotropic, $\boldsymbol{\beta}$(t), part of the polarizability:

$$\boldsymbol{\alpha}_n^M(t) = \alpha\mathbf{I} + \boldsymbol{\beta}(t), \tag{2.17}$$

where ***I*** is the unit matrix and the anisotropic part is a product of gas phase anisotropy with the molecular orientational tensor: $\boldsymbol{\beta}(t)=\gamma Q(t)$. For definition of α and γ see Figure 2.6.

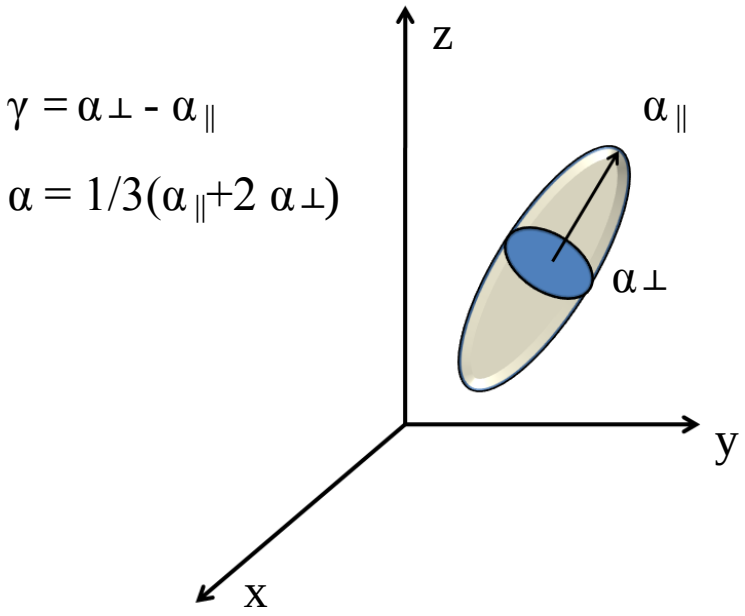

Figure 2.6 Illustration of polarizabilites of a molecule.

The II term is a complex phenomenon and molecular dynamics simulations (atom-atom Lennard-Jones potential model with Verlet and Singer algorithms)[23] showed that it is properly described by the dipole-induced-dipole (DID) approximation:

$$\Pi^{II}(t) = \sum_{n=1}^{N} \sum_{m \neq n} \boldsymbol{\alpha}_n^M(t) \cdot T(r_{nm}) \cdot \tilde{\boldsymbol{\alpha}}_m^M(t) \qquad (2.18)$$

where $T(r_{nm}) = \nabla_i \nabla_j (r_{nm})^{-1}$ is the dipole interaction tensor between molecule *n* and *m* and $\tilde{\boldsymbol{\alpha}}_m^M(t)$ is the effective polarizability of molecule, *m*, which includes local field contribution from all other molecules:

$$\tilde{\boldsymbol{\alpha}}_m^M(t) = \boldsymbol{\alpha}_m^M(t) + \sum_{p=1}^{N}\sum_{p\neq m}\boldsymbol{\alpha}_m^M(t)\cdot T(r_{mp})\cdot\boldsymbol{\alpha}_p^M(t) + \ldots \tag{2.19}$$

In the first order DID approximation $\tilde{\boldsymbol{\alpha}}_m^M(t)$ can be replaced by the polarizability of an isolated molecule. The Eq. 2.17 can be used to expand Eq. 2.18 in order to determine which polarizability components contribute to the anisotropic and isotropic response:[4, 22]

$$\Pi = \Pi^{M,\alpha} + \Pi^{M,\beta} + \Pi^{II,\alpha\alpha} + \Pi^{II,\beta\beta} + \Pi^{II,\alpha\beta+\beta\alpha} \tag{2.20}$$

The first term is constant in time and is therefore not observed in the time resolved Raman signal. The second term describes purely orientational scattering. The other terms can be ascribed to isotropic and anisotropic contributions in the following way:[4]

$$\Pi^{iso} = a_{iso}\Pi^{II,\alpha\beta+\beta\alpha} + b_{iso}\Pi^{II,\beta\beta} \tag{2.21}$$

$$\Pi^{aniso} = \Pi^{M,\beta} + \Pi^{II,\alpha\alpha} + (1-a_{iso})\Pi^{II,\alpha\beta+\beta\alpha} + (1-b_{iso})\Pi^{II,\beta\beta} \tag{2.22}$$

The expressions for constants *a* and *b* are given by Frenkel and McTague.[22] It is important to note that the isotropic part of the polarizability contains only II contributions, whereas the anisotropic one contains both molecular and II.

However, the range of validity of the first order approximation just described is questionable. De Santis *et al.*[24] and Elliasmine *et al.*[25] suggested that in order to calculate the collective polarizability, the inclusion of higher order multipole terms (e.g. dipole-quadrupole) is necessary.

2.3 Optical Kerr Effect Spectroscopy Based on a Diffractive Optic Element (DOE-OKE)

The spectra obtained from the OHD-OKE technique may be difficult to interpret because of contributions from different molecular and II processes (Eq. 2.20). The isotropic response, which resolves some of these components can be accessed with conventional OKE spectroscopy by modifying the polarization of the pump and probe beams. However, the observed signal would be very weak because the lack of the heterodyne detection, and thus almost indistinguishable from the noise. The polarization requirements for the isotropic response are that the signal radiated has the same direction and polarization as the probe beam, making it impossible to introduce the local oscillator by simply rotating the polarizer in the probe pathway. In this case, in order to separate the single molecule contribution to the polarizability from the interaction induced part, a different technique is required. Two different OKE techniques to measure the isotropic response were developed, one called spatially masked optical Kerr effect (SMOKE)[4] and the second based on the diffractive optical element (DOE-OKE).[6, 10, 26] Although the SMOKE method is easy to implement in the pump-probe geometry it has lower signal to noise ratio which makes this technique inferior to DOE-OKE. This is probably because in SMOKE both probe and signal propagate in the same direction exposing the detector to high intensity. In this geometry heterodyning is obtained from the phase shift between the signal and probe wave fronts. The phase difference arises from the smaller beam waist of the signal compared to the probe, which is optimized by selecting the central portion. The DOE-OKE method was implemented here and this technique will be described here in detail. A diagram of the experimental setup is shown in Figures 2.7a and b.

Figure 2.7a presents the part of experimental setup which contains the laser source, pulse recompression stages, delay stage and beam splitter, which divides the beam into pump and probe beams. The source for the ultrashort pulses was a commercial

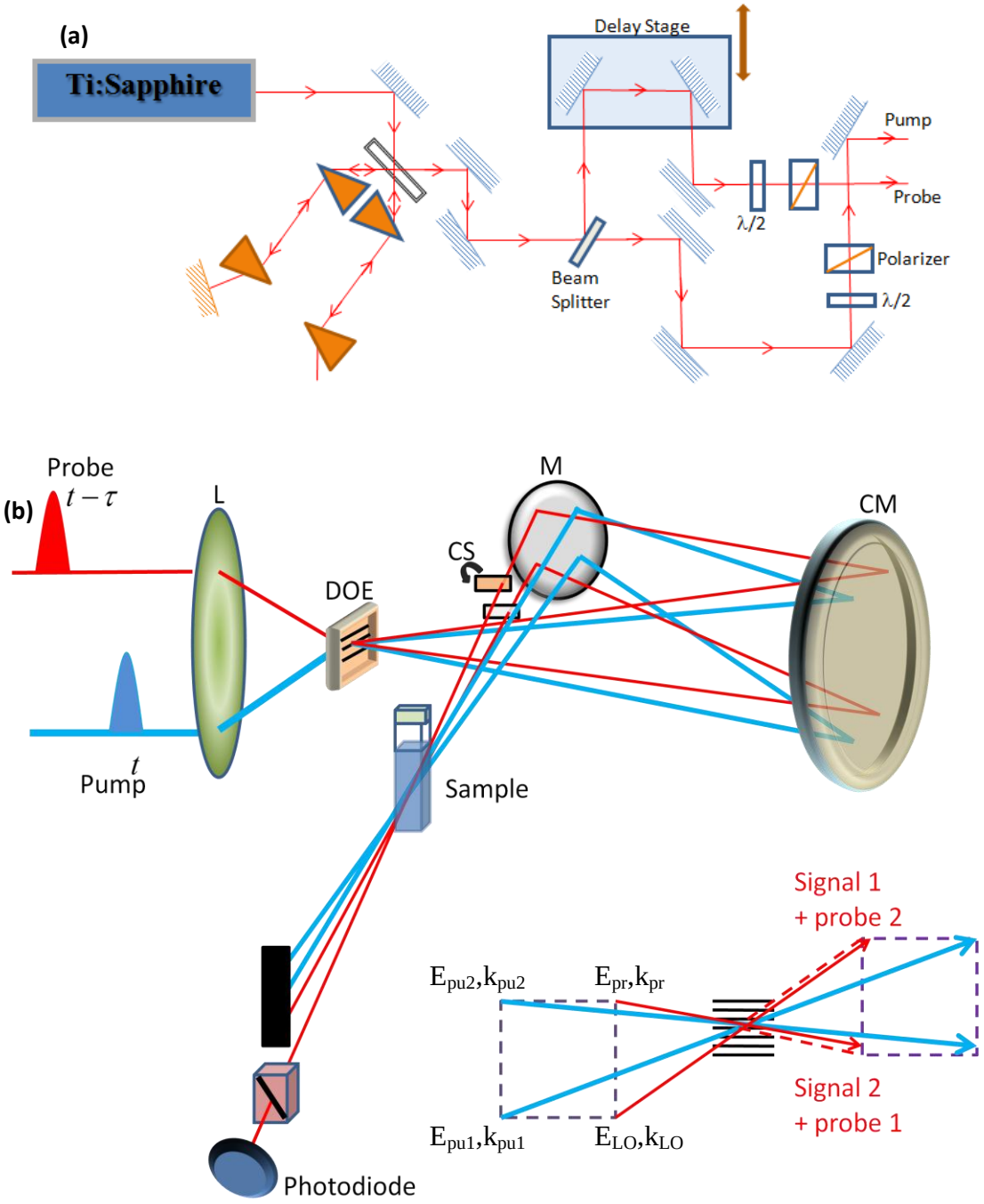

Figure 2.7 Outline of OKE experiment with diffractive optics element. L=lens; DOE= diffractive optic element; CS = cover slip; M= mirror; CM= concave mirror

Kerr-lens mode-locked Ti:Sapphire laser (Micra 10, Coherent) pumped by a 10 W (CW) intracavity-doubled diode-pumped Nd:YVO_4 laser (Coherent Verdi). The output had an approximately 800 nm centre wavelength, an average power of 800mW and a bandwidth of 85nm, the repetition rate was 76 MHz. The pulse recompression

was performed in two stages consisting of two pairs of fused silica prisms, in a folded geometry arrangement.[27] The prism stages were mounted "back to back" (Figure 2.7a) in order to compensate for any spatial chirp introduced by the recompression process.[28] The first prism stage is necessary to compensate for the chirp present on the output of the laser, typically around 800 fs^2. The second prism stage compensates for the chirp introduced by the optical elements used for the OKE experiments, which amounts to approximately 1000 fs^2 (the main source of dispersion are the Glan polarizers which have around 16mm pathlength). Measuring the autocorrelation at the sample position (including transmission through an amount of glass equivalent to the cell window) with a 50 μm BBO crystal revealed typical pulse durations of 17 fs (i.e. an autocorrelation width equal to 26 fs and an assumed hyperbolic secant function resulted in time bandwidth product ~0.6). Laser bandwidth is shown in Figure 2.8.

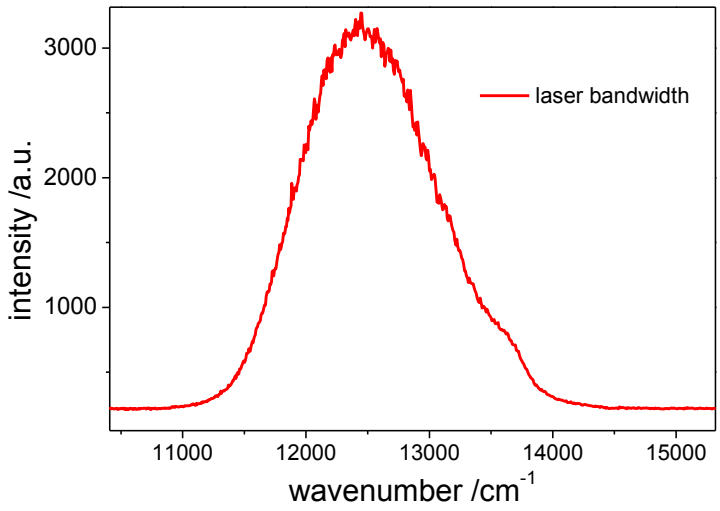

Figure 2.8 Micra laser bandwidth.

The pump and probe beams were obtained with a broadband beam splitter (Femtolasers, OA078) which divided the intensity into a 50:1 ratio. Both beams were

routed through separate but identical achromatic half wave plates (λ/2, Bernhard Halle, RAC 5.2.10) and polarizers (Karl Lambrecht Corporation, Glan-Thompson MGT25A8, extinction 10^{-5}) in order to define the relative polarization directions. To access the isotropic χ_{ISO}, polarized χ_{ZZZZ} and depolarized χ_{ZZYY} responses, the probe pulse was aligned relative to the pump at 54.7^{o} (magic angle at which orientational contributions disappear), 0^{o} and 90^{o} (Figure 2.9), respectively.

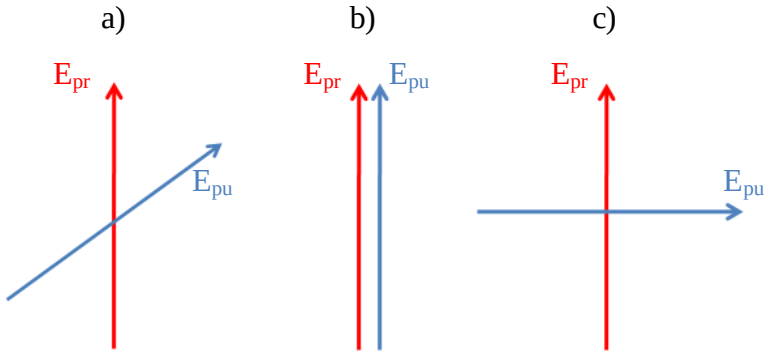

Figure 2.9 Direction of polarization of pump, E_{pu} and probe, E_{pr} beams for a) χ_{ISO}, b) χ_{ZZZZ} and χ_{ZZYY}

The pump and probe beams were focused to a common spot with a 150 mm focal-length lens. The initial alignment consists of the positioning of a BBO crystal at the focal position. The spatial and temporal overlap of the pulses can be found by looking for the emitted second harmonic signal (Figure 2.10). With the BBO in place, a

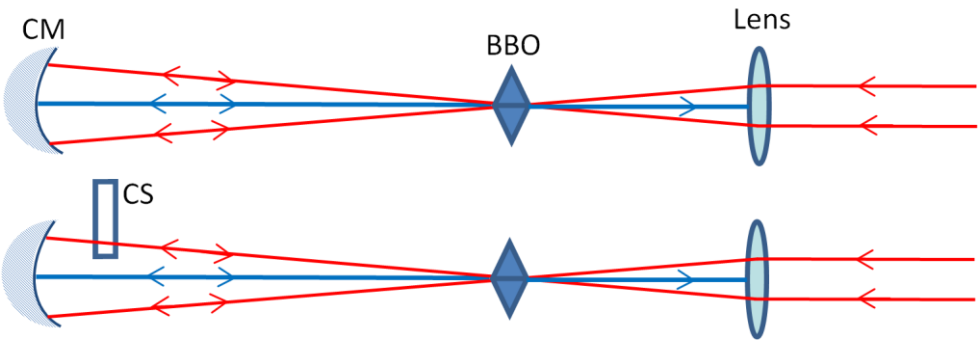

Figure 2.10 Alignment with BBO crystal

concave mirror with a focal length of 150 mm was placed one radius of curvature (R= 2f = 300mm) away from the BBO position (or the focal point of the lens) in order to refocus the beams to the focal spot of the first lens. In order to align the concave mirror properly, the refocusing is done with a slight vertical offset so that the reflected second harmonic beam can be observed with a card behind the lens. By inserting a thin glass window (microscope cover slip, CS, 150 μm thickness) to increase the optical path length, it is possible to separate temporally the second harmonic being generated by the lens focal spot from the second harmonic generated by the beams reflected from the concave mirror. If the beams are properly overlapped spatially and temporally inside the BBO crystal it is possible to observe (with a card positioned above the incoming beams on the back of the lens) two second harmonic spots by changing the delay stage, one coming from the incoming beams and the other created from beams reflected from concave mirror. Once this alignment was finished, the concave mirror was tilted slightly off-axis to separate the incident and reflected beams horizontally, so that it was possible to steer the beams into the sample cell (Figure 2.7b). The BBO crystal was then removed and the diffractive optical element (National Optics Institute, Canada) was positioned at the focal spot. This element, which was specifically designed for efficient diffraction into first order, consisted of a diffraction grating etched in a fused silica substrate with a period of 23.2 μm. The diffraction efficiency for the ±1 orders was greater than 75% and the angle between the diffracted beams was 5.72^{o}. There was virtually no variation in either the diffraction efficiency or the phase of a given diffraction order with respect to input polarization. After the DOE, multiple beams were observed, but the first order was selected by a mask. Thus the four beams obtained consisted of two pump beams (k_{pu1}, k_{pu2}) and two probe beams (k_{pr1}, k_{pr2}). The pump beams (k_{pu1}, k_{pu2}) were crossed at the

sample position and create an interference pattern, which leads to a transient index grating (i.e. a special dependence of n_2), from which probe induced signal is diffracted following the phase matching condition: $k_{sig} = k_{pr1} + k_{pu1} - k_{pu2}$ (Figure 2.7). The box geometry of the experiment, Figure 2.7, ensures that this signal is radiated along the same direction as the k_{pr2} probe beam, so this probe beam may be used as a local oscillator (LO) to heterodyne the signal ($k_{pr2} = k_{LO}$).[29] The cover slip inserted into the LO pathway is used to control the phase between probe and LO beams.

The measured intensity at the detector can be written as:

$$I = \left|E_{sig}(t) + E_{LO}(t)\right|^2 = \left|E_{sig}\exp\left(i\left(\omega_{sig}t + \varphi_{sig}\right)\right) + E_{LO}\exp\left(i\left(\omega_{LO}t + \varphi_{LO}\right)\right)\right|^2 \qquad (2.23)$$

where ω_{sig} and ω_{LO} are the signal and local oscillator electric field frequencies with their respective phase, φ_{sig} and φ_{LO}. For OKE experiments, $\omega_{sig} = \omega_{LO}$, so that the above expression can be written, retaining only the real part, as:

$$I = \left|E_{sig}(t)\right|^2 + \left|E_{LO}(t)\right|^2 + 2\left|E_{sig}(t)E_{LO}(t)\right|\cos(\varphi_{sig} - \varphi_{LO}) \qquad (2.24)$$

which resembles Eq. 2.11. However in the DOE-OKE attention is paid to the phase relationship between the probe and LO, $\cos(\varphi_{sig} - \varphi_{LO})$, which is adjusted by the cover slip. The electric field of the signal, $E_{sig}(t)$ under phase-matching conditions, can further be written in terms of the material response function and pump and probe electric fields as:[30]

$$E_l^{sig}(t) = i\sum_{ijk}\chi_{ijkl}^{(3)}(t)E_i^{pu1}E_j^{pu2*}E_k^{pr} \qquad (2.25)$$

where E_i^{pu} and E_k^{pr} are components of the pump and probe electric field vectors. By writing explicitly the electric field phases, the above expression becomes:

$$E_l^{sig}(t) = \sum_{ijk}\left|\chi_{ijkl}^{(3)}(t)\right|\left|E_i^{pu1}\right|\left|E_j^{pu2*}\right|\left|E_k^{pr}\right|\exp\left(i\left(\frac{\pi}{2} + \varphi_{\chi}(t) + \varphi_{pu1} - \varphi_{pu2} + \varphi_{pr}\right)\right) \qquad (2.26)$$

where $\varphi_{pu1}, \varphi_{pu2}, \varphi_{pr}$ and $\varphi_{\chi}(t)$ are the pump, probe and material response electric field phases, respectively. The $\pi/2$ factor accounts for the non-resonant 90º phase retardation. By writing an effective material response function, $\chi^{(3)}_{eff}(t) = \sum_{ij} \chi^{(3)}_{ijkl}(t) E_i^{pu1} E_j^{pu2*}$, the above expression can be simplified:

$$E_l^{sig} = \left|\chi^{(3)}_{eff}(t)\right| E^{pr} \left| \exp\left(i\left(\frac{\pi}{2} + \varphi_{\chi}(t) + \varphi_{pu1} - \varphi_{pu2} + \varphi_{pr} \right)\right)\right. \tag{2.27}$$

Substituting the above expression into Eq. 2.24 and retaining only the interferometric term, (the other terms are small or not detected by the lock in detection) the resulting expression is:

$$I = 2\left|\chi^{(3)}_{eff}(t)\right| E^{pr} \left| E_{LO} \right| \cos\left(\frac{\pi}{2} + \varphi_{\chi}(t) + \varphi_{pu1} - \varphi_{pu2} + \varphi_{probe} - \varphi_{LO} \right) \tag{2.28}$$

Using the trigonometric identity, $\cos(\alpha+\beta) = (\cos\alpha)(\cos\beta) - (\sin\alpha)(\sin\beta)$ the above equation is rewritten in terms of real and imaginary components of $\chi^{(3)}_{eff}$:

$$I = 2\left|E^{pr}\right| E_{LO} \left| \left(\mathrm{Re}\left\{\chi^{(3)}_{eff}(t)\right\} \sin(\phi) + \mathrm{Im}\left\{\chi^{(3)}_{eff}(t)\right\} \cos(\phi) \right)\right. \tag{2.29}$$

where the overall phase is defined as $\phi = \varphi_{pu1} - \varphi_{pu2} + \varphi_{probe} - \varphi_{LO} \equiv \varphi_{sig} - \varphi_{LO}$. In order to access the real part of the material response function related to variation of the refractive index, *i.e.* the material birefringence, the phase has to be set to $\phi = \pi/2$. Since we have no experimental access to the individual phases, but only to the overall phase ϕ, in order to measure the real or imaginary components of the nonlinear susceptibility unambiguously, an initial adjustment with some reference material with a well known strong birefringence response has to be done.[29] A good sample for this is carbon disulfide, as it has a strong OKE signal and is transparent in the 800nm region, *i.e.* the dichroism (imaginary contribution) can be assumed to be zero. To adjust the phase a pair of cover slips were inserted separately into the LO and probe

pathways. One of the cover slips has a ~60nm thick gold film and therefore attenuates the beam by approximately 1000 times. The LO beam is attenuated in order to avoid saturation of the photodiode. This beam will serve as a local oscillator. The cover slips were mounted on a common holder (Newport, HVM-1) to avoid relative motion

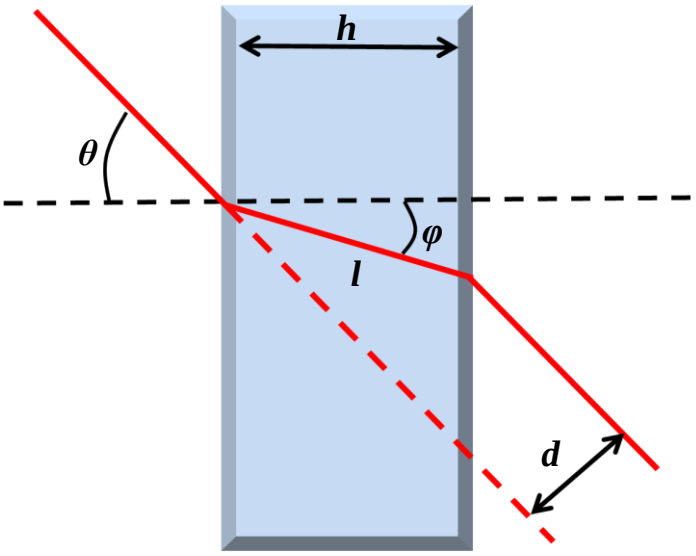

Figure 2.11 Beam propagation through the cover slip.

fluctuations which could deteriorate the phase stability. The mount rotation range was ±3.5° with a sensitivity of 2.5 arc sec. By rotating one of the cover slips, the effective pathlength traversed by one of the beams changes such that it is possible to fine tune the phase difference (Figure 2.11). The expression for the pathlength difference is $\Delta l = nh\left(1-\cos^{-1}\varphi\right)$, where $\varphi = \arcsin\left(\sin\theta / n\right)$ and n is the refractive index of the cover slip material. The lateral dislocation of the beam is given by $d = h\sin(\theta-\varphi)/\cos(\varphi)$ and can be minimised by working with thin glass windows. In this study cover slips with thickness of 200 µm were used. The phase difference is then given by $\Delta\varphi = 2\pi\Delta l/\lambda$. A phase of 180° can be achieved rotating the cover slip by 4.57°. This results in a lateral displacement of only 5.6 µm and a relative temporal mismatch of the signal and local oscillator pulses of 1 fs.

By rotating the cover slip one can maximize the signal for a fixed delay time position. This will ensure the correct phase setting, *i.e.* $\pi/2$. After the sample the pump beams and the probe beam were blocked with a screen (Figure 2.12). A small hole in the

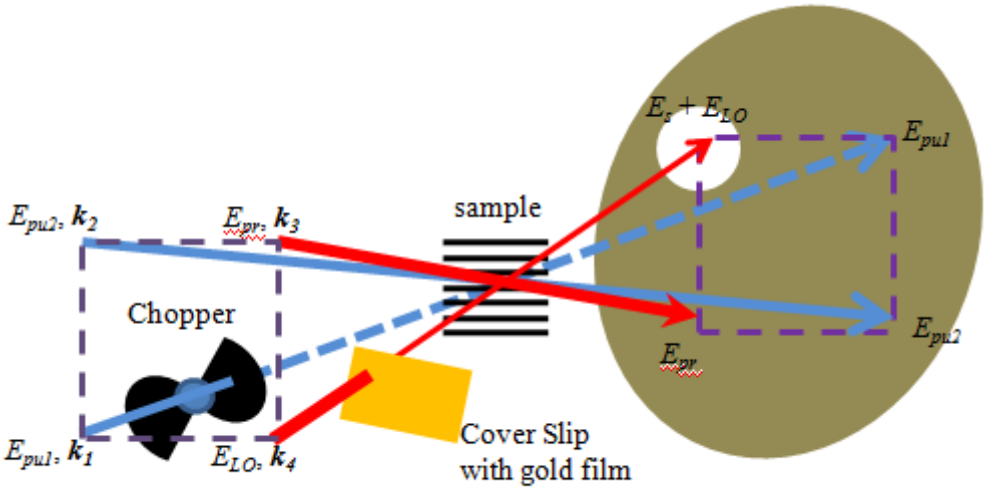

Figure 2.12 Scheme of beams propagating through the sample.

screen lets the local oscillator plus signal propagate through to the analysing polarizer which is oriented to pass only the component of polarization parallel to the probe polarization. The transient grating signal measured by the photodiode was routed to a lock-in amplifier (SR830 Stanford Research). The optical chopper was positioned between the DOE and the sample and modulated one of the pump beams (Figure 2.12). The signals which are emitted in wavevector direction k_{LO} (or signal wavevector direction, k_{sig}) are given by the following expressions: transient grating, TG, $k_{sig} = k_{pu1} - k_{pu2} + k_{pr}$; pump-probe signals: PP1, $k_{sig} = k_{pu1} - k_{pu1} + k_{LO}$; PP2, $k_{sig} = k_{pu2} - k_{pu2} + k_{LO}$; PP3, $k_{sig} = k_{pr} - k_{pr} + k_{LO}$. The pump-probe signals PP2 and PP3 are not detected by the lock-in because these beams are not modulated. Only PP1 and TG are detected by the lock-in, however PP1 signal is negligible for nonresonant (transparent) samples, *i.e.* the dichroism signal is very small.

2.4 Data Analysis and Interpretation

The OKE signal can be due to diffusive reorientation, libration or interaction induced contributions. The libration can be thought of as non-diffusive nuclear reorotational motion of a molecule on a potential surface defined by interaction with a cage formed by its nearest neighbour molecules. The interaction induced response is due to "collision induced" and dipole-induced-dipole interaction which a molecule experiences from its nearest neighbours, details in section 2.2.3.2.

2.4.1 Relaxation Process

In general, the time domain OKE trace can be divided into slow (picosecond) and fast (subpicosecond) components. For a single molecule in a liquid the reorientational time can be connected to the liquid viscosity of the medium, η by the Debye-Stokes-Einstein (DSE) relation:[31]

$$\tau_n = \frac{\eta V_{eff}}{k_B T} + \tau_n^0 \tag{2.30}$$

where τ_n is a relaxation time, V_{eff} is the effective hydrodynamic volume of the molecule, k_B denotes the Boltzmann constant, T is temperature and τ_n^0 is a reorientational time at zero viscosity, which can also be equal to the free rotor time.[31] However the relaxation time observed in OKE is due to collective motion of molecules and can be written as:

$$\tau_{OKE} = \frac{\tau_n g}{j} \tag{2.31}$$

where g is called the static orientational pair correlation parameter and j accounts for dynamic orientational pair correlation. Parameter j is assumed to be unity in simple liquids[31] and g is given by $g = 1 + n\frac{\langle P_2(1)P_2(2)\rangle}{\langle P_2(1)P_2(1)\rangle}$, where n is the number of scattering

molecules and P_2(i) is a second rank Legendre function of the orientation of molecule *i*.[31]

The fast component describes dynamics which are non-diffusive in nature. It contains information about intermolecular and intramolecular modes. It reflects the librations/vibrations of the molecules.

The slow relaxation tail can be fit with different functions. We employed two different fitting procedures:

(1) First time-derivative, *r(t)*, of the correlation function represented by a stretched exponential (Kohlrauch-William-Watts)[32] function: $\psi_{xz}(t) \propto \exp(-t/\tau)^{\beta}$, in which case:

$$r(t) = \frac{\beta t^{\beta-1}}{\tau^{\beta}} \exp\left[-\left(\frac{t}{\tau}\right)^{\beta}\right] \tag{2.32}$$

where β is stretching exponent. For this function the mean relaxation time is given from the relation:

$$\langle\tau\rangle = (\tau/\beta)\Gamma(1/\beta) \tag{2.33}$$

where Γ(x) is the gamma function.

(2) a sum of exponential functions:

$$r(t) = \sum_i a_i \exp(-t/t_i)][1-\exp(-t/t_r)] \tag{2.34}$$

where a_i is amplitude and t_r is a risetime. Different values of the rise time were tried in the range 1 -100 fs and other fitting parameters in the above equation were found to be insensitive to the exact value of the ultrafast risetime, as previously observed.[33] Therefore, for all fittings the risetime was kept constant at 10 fs. Mean relaxation times were calculated from the recovered fitting parameters using the relation:

$$\langle \tau \rangle = \frac{a_1}{a_1 + a_2} \tau_1 + \frac{a_2}{a_1 + a_2} \tau_2 \tag{2.35}$$

The quality of fit to both functions is shown in Figure 2.13. Criteria for the choice of fitting functions, was the chi square value obtained from each fit.

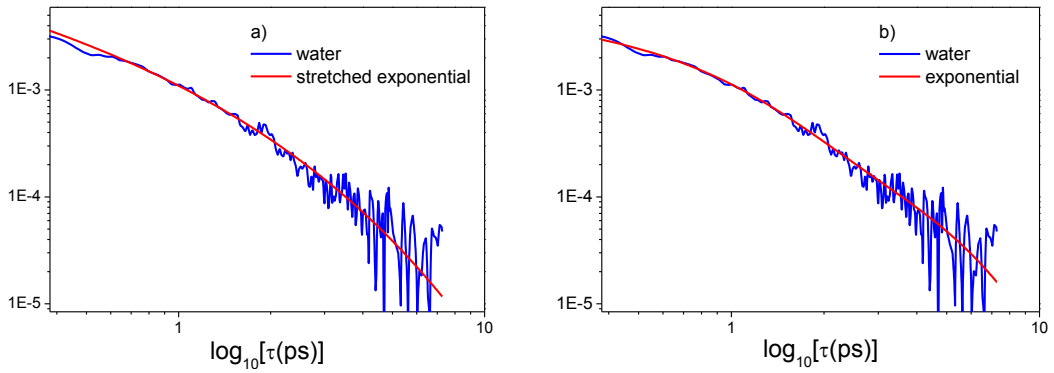

Figure 2.13 Quality of fit of a) the stretched exponential to water and b) biexponential to water.

In the Figure 2.13a, the fit to the data in the range 0.3 ps – 0.6 ps is of poor quality. As a result, after the stretched exponential is subtracted, negative intensity is obtained within given range. This results in lowering of the amplitude of the RSD spectrum.

2.4.2 Fourier Transform Analysis: THz Spectra and Fitting Procedure

The frequency representation of the OKE response contains the same information as the low frequency Raman spectrum obtained by traditional Raman techniques when corrected for the Bose-Einstein thermal factor, $n(E) = 1/[\exp(E/k_B T) - 1]$. As the ultrashort pulses are not instantaneous the measured signal, $S_{OKE}(t)$ is a convolution of second order autocorrelation,[34] $G_2(t) = \int_{-\infty}^{\infty} I(t) I(t-\tau) dt$ with the material response,

$S_{OKE}(t) \propto \int dt R_{OKE}(t-\tau) G_2(t)$. To obtain $R_{OKE}(t)$ in the frequency domain undistorted by convolution the deconvolution relationship:

$$\frac{FT\{S_{OKE}(\tau)\}}{FT\{G_2(\tau)\}} = D(\omega) \tag{2.36}$$

is used. This yields the spectral density, $D(\omega)$ independent of pulse width.[5] A valid spectrum is obtained only if $t = 0$ (zero delay between pump and probe pulses) of both the signal and the autocorrelations are identical. As both cannot be measured simultaneously, an empirical correction to the zero delay time is performed. This is done by ensuring that the spectral density from 0 cm^{-1} to the highest possible wavenumber has positive values.

The imaginary part of the spectral density, $\mathrm{Im}\, D(\omega)$ reflects only the nuclear response. The Fourier transform of the electronic response which is fitted with a Gaussian function that is symmetric around zero, has only a real part. The nuclear response in the frequency domain can be reconverted to the time domain by taking the inverse Fourier transform of $\mathrm{Im}\, D(\omega)$. To focus on the high frequency part of the spectral density, the long time response given by Eq. 2.32 or 2.34 is subtracted from the signal prior to the Fourier Transform. The spectrum with its long tail subtracted is called the reduced spectral density (RSD). Comparison of the spectrum with and without the relaxation tail is shown in Figure 2.14. Prior to the Fourier transform, the time domain data were zero padded in order to decrease the spacing of points in the frequency domain.

The spectral density of water with the long component included (red in Figure 2.14b)

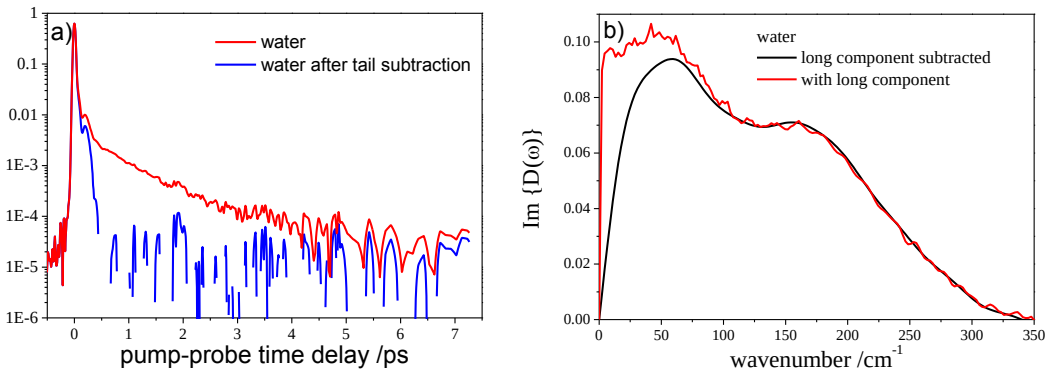

Figure 2.14 OKE water response with and without the picosecond component.

is noisy due to the noise present in the tail. The noise can be removed by replacing the experimental tail with the fitted function, or as in case of RSD, the tail after subtraction is replaced by zeros.

The low frequency water spectrum is very well known[35-37] (see below) and consists of three modes (45 cm^{-1}, 175 cm^{-1} and 400 cm^{-1}) The highest frequency mode was not resolved with our time resolution, instead amplitude of the spectrum above 350 cm^{-1} was found to increase, therefore 350 cm^{-1} wavenumber was set to have zero amplitude of RSD water spectrum. This was done by changing t = 0 ps of autocorrelation.

The spectral density typically reveals a multicomponent lineshape. To quantitatively compare spectra, we fit the spectral densities with a variety of functions previously successfully applied by our own and a number of other groups.[38-40] To fit the RSD of water only two functions were needed. The low frequency mode at ~45 cm^{-1}, Figure 2.15, was fitted by the Bucaro-Litovitz (BL) function[41], given by:

$$I_{BL} = A_{BL}\,\omega^{\alpha}\exp[-(\omega/\omega_{BL})] \qquad (2.37)$$

where A_{BL} is the amplitude, ω_{BL} is a characteristic frequency and α is a fitting parameter. The higher frequency ~180 cm^{-1} mode was fitted with an antisymmetrized Gaussian (ASG):

$$I_{ASG} = A_{ASG}\left[\exp\left[-\frac{\omega-\omega_{ASG}}{\Delta\omega_{ASG}}\right]^2 - \exp\left[-\frac{\omega+\omega_{ASG}}{\Delta\omega_{ASG}}\right]^2\right] \qquad (2.38)$$

where A_{ASG} denotes the amplitude, ω_{ASG} is the central frequency and $\Delta\omega_{ASG}$ is the full with at half-maximum. Figure 2.15 shows the water spectrum and the two fitting functions.

The fit of the Im $D(\omega)$ to a series of Brownian oscillators[19] was also tried. However this fit was of worse quality than the sum of BL and ASG. The BL function is generally associated with collision induced dynamics,[41] however it gave relatively good quality fit to low frequency water mode. It is possible to fit the 45 cm^{-1} mode with ASG function or Brownian oscillator, or BL and some additional function. However these additional functions would have no physical meaning. In some cases, spectral densities were much more complex and additional functions were needed to fit them.

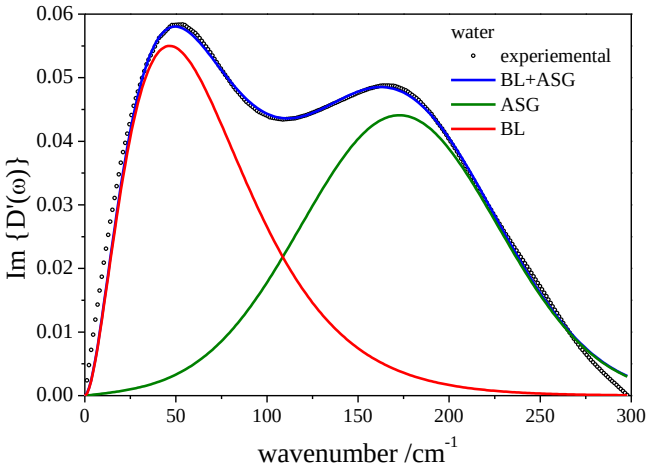

Figure 2.15 Fit to water spectrum, black dots denote experimental data, BL-Bucaro-Litovitz, ASG-Antisymmetrized Gaussian, and the blue line is a sum of recovered spectral shape from fitting functions.

The extra function used in these cases was generally a Gaussian shape and given by:

$$I_G = A_G \exp\left[-\frac{\omega-\omega_G}{\Delta\omega_G}\right]^2 \tag{2.39}$$

where A_G denotes the amplitude, ω_G denotes the central frequency and $\Delta\omega_G$ is the full with at half-maximum.

2.4.3 Water Signal

Water is one of the most important and most studied liquids and its spectrum will be the basis of our studies of aqueous solutions. It was studied in the past through various techniques: dielectric relaxation,[42] infrared,[43-46] NMR,[47] Raman,[48] terahertz spectroscopy[49] and optical Kerr effect.[32, 50] Dielectric relaxation and NMR experiments provide information on the molecular reorientational time of water molecules. With ultrafast 2DIR one can measure spectral diffusion of the OH/OD stretch vibrations of water,[45] while IR pump-probe resolves molecular reorientation. The THz spectroscopy probes the collective water network motions such as translational and rotational diffusion and librational motion. Despite such extensive studies water is still one of the least understood liquids and some conflicts exist between these experiments.

The polarizability of water is nearly isotropic, $\beta \approx 0$,[51] (Eq. 2.17) therefore according to Eq. 2.22 the term $\Pi^{M,\beta}$ has a negligible contribution to the anisotropic response. Thus pure rotations make only a minor contribution to the observed signal, and water dynamics are dominated by the $\Pi^{II,\alpha\alpha}$ (translational) contribution. Thus the relaxation time observed in OKE must be defined as a structural reorganization (translational motion) of the H-bonded network. The time domain water OKE trace is shown in

Figure 2.14a and its frequency representation is shown in Figure 2.14b. The water spectrum has three characteristic bands at ~45 cm^{-1}, 175 cm^{-1} and 400 cm^{-1}. The latter one originates from inertial and librational dynamics of a single molecule and should contribute at 20 fs.[52, 53] This mode however was not resolved with the time resolution of our OHD-OKE experiment. The other low frequency modes were assigned earlier by analogy with ice[35, 54] and on the basis of molecular dynamics simulations.[53, 55] The 175 cm^{-1} mode was assigned to an intermolecular H-bond stretch,[56, 57] albeit one delocalized over several water molecules.[53] The 45 cm^{-1} band was assigned to the H-bond bending mode.[56, 57] However the role of H-bonds in this mode is still a matter of discussion. The Raman measurement of H_2S, structurally similar to water but unable to form intermolecular H-bonds, showed no difference compared to water in the low frequency spectra, but the 175 cm^{-1} mode was absent in the H_2S spectrum.[58] Therefore both modes cannot be associated with H-bond. It was suggested that the 45 cm^{-1} band originates from the bend of a central molecule within the cage formed by its neighbours.[56] Nakayama,[59] on the basis of a simple model analysis of low energy excitations in water, concluded that the low frequency mode is a strongly localized one, whereas the 175 cm^{-1} mode can be associated with motion mesoscopically distributed in the H-bonded water network as also shown by Ohmine.[53] Previous studies have linked the 45 cm^{-1} mode to the TA (transverse) phonon mode and restricted translation perpendicular to OH···O, whereas 175 cm^{-1} was linked to a LA (longitudinal) phonon mode and restricted translation parallel to OH···O.[54, 57, 60] None of the above designations for a given mode contradict any other and the designation may be a matter of preference.

There are also different interpretations of the water picosecond response. Castner *et al*.[36] associated the long relaxation time to the diffusive rotational motion of the water

molecules. In contrast Palese *et al.*[61] argued that the long component is due to diffusive translational and rotational motions of large water aggregates within the hydrogen-bonded network spanning large length scale. Laage and Hynes[62] proposed an extended molecular jump mechanism model of water reorientation. Using their

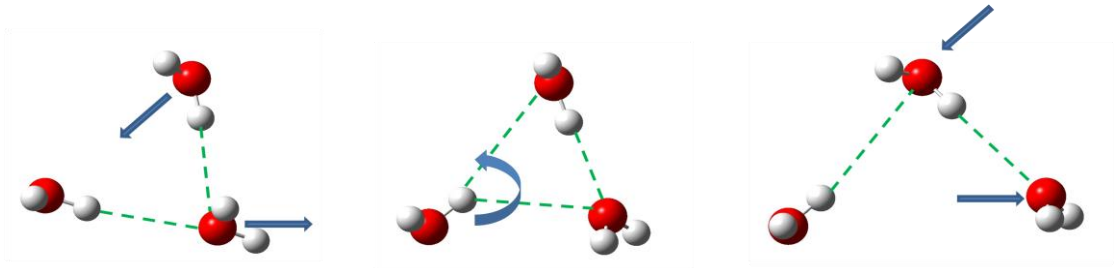

Figure 2.16 Scheme of the different steps in molecular jump mechanism as proposed by Laage et al.[62] The green dashed lines denote H-bonds and blue arrows show motion of water molecules.

model they found that water orientational dynamics are non-diffusive but also that the rotational and translational motions are strongly coupled. In their model, the reorienting water OH group forms H-bond with another water molecule, Figure 2.16. When another water molecule approaches, this H-bond elongates and symmetric bifurcated H-bonds with two water molecules are formed. The initial H-bond breaks and the H-bond with second water molecules stabilizes.

The isotropic OKE trace of water in both the time and frequency domain is shown in Figure 2.17. The time domain response is characterized by a dominant electronic response and a small fast decaying component, which extrapolates to zero at 300 fs. Its isotropic spectrum consists of two modes, at 80 cm^{-1} and 800 cm^{-1}. The presence of an intermolecular mode in the isotropic response at 800 cm^{-1} makes the water molecules unique, as this region is generally associated with intramolecular modes. In

addition the small signal intensity indicates that β is finite or that the signal arises from higher order terms, Eq.2.19.

The isotropic response of pure water was studied previously by Tokmakoff *et al.*[4] (SMOKE spectroscopy) and Mazzacurati *et al.*[63, 64] (polarized Raman spectroscopy). Mazzacurati *et al.*[24, 63, 64] concluded that the second order DID contributions ($\Pi^{II,\alpha\alpha\alpha}$)

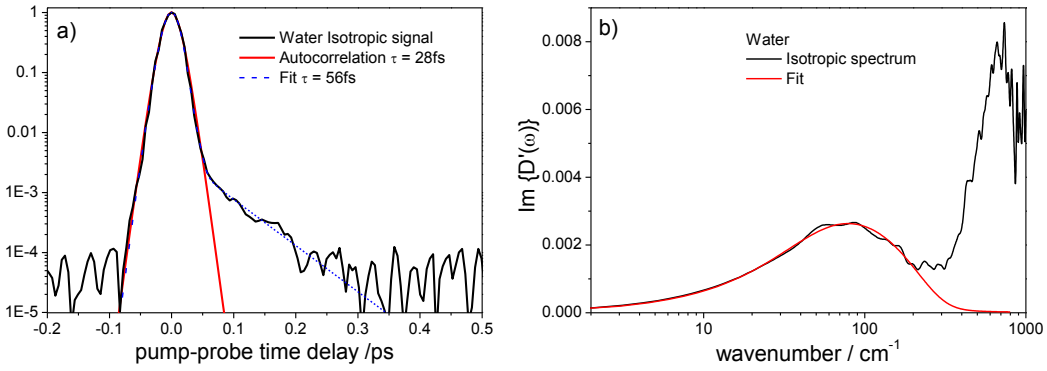

Figure 2.17 a) Isotropic time domain Kerr transient of pure water and b) its corresponding frequency domain.

and the effects of the fluctuating dipoles through the second order hyperpolarizability are responsible for the observed isotropic modes. These terms contain only translational variables, i.e. consistent with $\beta = 0$.

In contrast the two modes at 45 cm^{-1} and 180 cm^{-1} in the anisotropic response were assigned to $\Pi^{II,\alpha\alpha}$ by Mazzacurati *et al.*[24] and Madden *et al.*[65]

2.4.4 Depolarization Ratio

Isotropic and anisotropic OKE response can be written in terms of polarized and depolarized components as:[13]

$$R_{ISO} = R_{ZZZZ} + 2R_{ZZYY}$$

$$R_{ANISO} = R_{ZZZZ} - R_{ZZYY} = R_{ZYYZ} + R_{ZYZY} \tag{2.40}$$

The water signal measured in three configurations, relative pump probe polarization of 0^0, 90^0 and 54.7^0 for R_{zzzz}, R_{zzyy} and R_{ISO}, respectively (for definition see Figure 2.9), are shown in Figure 2.18.

In linear polarization resolved Raman scattering symmetry, a Raman active mode is described in terms of its depolarization ratio:

$$\rho = \frac{I_{VH}}{I_{VV}} = \frac{3\beta^2}{45\alpha^2 + 4\beta^2} \tag{2.41}$$

where V and H describe directions that are vertical and horizontal to the plane of scattering. For a totally symmetric vibration, $\rho \approx 0$ and a for non-totally symmetric vibration, ρ takes values between 0 and 0.75. Quantities I_{VH} and I_{VV} can be related to the present OKE measurement:[66]

$$I_{VH} = \frac{1}{2}\left(R_{ZZZZ} - R_{ZZYY}\right) \tag{2.42}$$

$$I_{VV} = R_{ZZZZ} \tag{2.43}$$

We can thus write the depolarization ratio in the frequency domain as:

$$\rho(\omega) = \frac{1}{2}\left(1 - \frac{\chi_{ZZYY}(\omega)}{\chi_{ZZZZ}(\omega)}\right) = \frac{3}{2}\left(2 + \frac{\chi_{ISO}(\omega)}{\chi_{ANISO}(\omega)}\right) \tag{2.44}$$

The depolarization ratio obtained from Eq. 2.44 is also plotted in Figure 2.18. The depolarization ratio in the region between 0 - 500 cm^{-1} remains between 0.67 and

0.71. Above 500 cm^{-1} the depolarized ratio decreases significantly, this is accompanied by the growth of the 800 cm^{-1} mode in the isotropic response, Figure 2.18b. Previous depolarization ratio values, obtained from SMOKE, were found to be between 0.70 and 0.75 in the 0-250 cm^{-1} spectral region.[4] Walrafen, using Raman spectroscopy, found depolarization ratio < 0.75 in the region below 250 cm^{-1}.[67]

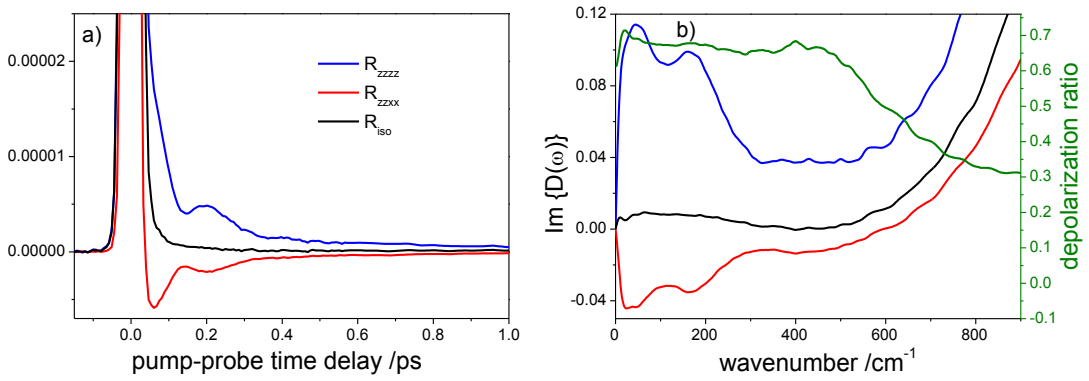

Figure 2.18 OKE response at different pump-probe polarization angles a) time domain and b) its frequency representation. Green line denotes depolarization ratio.

The spectrum above 600 cm^{-1} (Figure 2.18b) was found to depend on the right choice of t = 0 ps of the autocorrelation, therefore this region is characterized with large error.

2.5. Samples

Sample handling techniques for the samples described in subsequent chapters are collected here.

Chapter 3. Water and salts were purchased from Sigma Aldrich, and were used as received. The salt solutions were injected into the 2 mm path length quartz cuvette through a 0.2 μm micropore filter. All solutions were prepared in concentration 1 M - 6 M or to saturation concentration.

Chapter 4. All samples used in the study, FA, UA, TMAO, TBA and TMU were purchased from Sigma Aldrich. Samples were used as received and aqueous solutions were prepared between concentrations of <0.1 M and the maximum possible concentration (4 M saturated solution for TMAO, 8 M UA, neat FA, TBA and TMU). To reduce light scattering, from dust particles, all samples were filtered through a 0.2 μm Millipore filter. The viscosities of all aqueous solutions, except for the temperature dependence of TBA and TMAO solutions, were taken from the literature.[68-71] The viscosities of TMAO and TBA in the range of temperature 20 - 80 ºC were measured using an Oswald type viscometer, with the viscometer constant 0.01019. Each measurement was performed three times and then the average was taken (error 5%).

Chapter 5. The three peptides were obtained from Bachem (Germany) and used as received. They were dissolved in water at pH 4 and contained in 2 mm fused silica cells. All samples were filtered through a 0.2 μm Millipore filter to remove any particulate matter. Viscosities were measured in a separate experiment using a rotating conical plate rheometer (Bohlin Instruments). All measurements were made at concentrations between 0.1 M and 3 M (mol fraction 0.002 to 0.051) except for NALMA where maximum solubility was limited to 2 M.

Chapter 6. Lysozyme from chicken egg white (mol. wt. 14.3 kDa), trypsin from bovine pancreas (mol. wt. 23.8 kDa) and albumin from bovine serum (BSA, mol. wt. 66 kDa) were purchased from Sigma Aldrich. All samples were used as received. Aqueous solutions were prepared with concentrations between 0 wt. % up to the maximum possible concentrations of 15 wt. %, 25 wt. % and 30 wt. % for trypsin, BSA and lysozyme, respectively. In order to remove any undissolved matter, all

samples were filtered through a 0.2 µm Millipore filter. Viscosity measurements were carried out using an Ostwald type viscometer, with the viscometer constant 0.01019. Each measurement was repeated three times, at a temperature of 19 ±1 °C and an average was taken, (error 5%).

2.5. References

1. B. I. Greene, P. A. Fleury, H. L. Carter and R. C. Farrow, *Physical Review A*, 1984, **29**, 271-274.
2. B. M. Ladanyi and Y. Q. Liang, *J. Chem. Phys.*, 1995, **103**, 6325-6332.
3. K. Mazur, I. A. Heisler and S. R. Meech, *J. Phys. Chem. B*, 2010, **114**, 10684-10691.
4. C. J. Fecko, J. D. Eaves and A. Tokmakoff, *J Chem Phys*, 2002, **117**, 1139-1154.
5. W. T. Lotshaw, D. McMorrow, N. Thantu, J. S. Melinger and R. Kitchenham, *J. Raman Spectrosc.*, 1995, **26**, 571-583.
6. Q. H. Xu, Y. Z. Ma and G. R. Fleming, *Chem. Phys. Lett.*, 2001, **338**, 254-262.
7. G. Giraud, J. Karolin and K. Wynne, *Biophys. J.*, 2003, **85**, 1903-1913.
8. H. Shirota and H. Ushiyama, *J. Phys. Chem. B*, 2008, **112**, 13542-13551.
9. B. J. Loughnane, A. Scodinu and J. T. Fourkas, *J. Phys. Chem. B*, 2006, **110**, 5708-5720.
10. G. D. Goodno, G. Dadusc and R. J. D. Miller, *J Opt Soc Am B*, 1998, **15**, 1791-1794.
11. Y. J. Chang and E. W. Castner, *J. Chem. Phys.*, 1993, **99**, 113-125.
12. P. N. Butcher and D. Cotter, *The Elements of Nonlinear Optics*, Cambridge University Press, 1990.
13. A. Tokmakoff, *J. Chem. Phys.*, 1996, **105**, 1-12.
14. M. D. Levenson and S. S. Kano, *Introduction to Nonlinear Laser Spectroscopy*, Academic Press, INC., 1988.
15. J. Garduno-Mejia and S. R. Meech, *Optics Communications*, 2006, **259**, 840-847.
16. E. Hecht, *Optics*, San Francisco; London; Addison-Wesley, 2002.
17. N. A. Smith and S. R. Meech, *Int. Rev. Phys. Chem.*, 2002, **21**, 75-100.
18. R. W. Boyd, *Nonlinear optics*, Elsevier, 2008.
19. S. Mukamel, *Principles of Nonlinear Optical Spectroscopy*, Oxford University Press, 1995.
20. S. Kinoshita, Y. Kai, T. Ariyoshi and Y. Shimada, *Int. J. Mod Phys B*, 1996, **10**, 1229-1272.
21. D. McMorrow, W. T. Lotshaw and G. A. Kenneywallace, *IEEE J Quantum Elect*, 1988, **24**, 443-454.
22. D. Frenkel and J. P. Mctague, *J. Chem. Phys.*, 1980, **72**, 2801-2818.
23. L. C. Geiger and B. M. Ladanyi, *J. Chem. Phys.*, 1987, **87**, 191-202.
24. A. Desantis, R. Frattini, M. Sampoli, V. Mazzacurati, M. Nardone, M. A. Ricci and G. Ruocco, *Mol. Phys.*, 1987, **61**, 1199-1212.

25. A. Elliasmine, J. L. Godet, Y. LeDuff and T. Bancewicz, *Physical Review A*, 1997, **55**, 4230-4237.
26. S. R. Meech and I. A. Heisler, *J. Phys. Chem. B*, 2008, **112**, 12976-12984.
27. C. Newport, *Prism Compressor for Ultrashort Laser Pulses*, Application Note.
28. S. Akturk, X. Gu, E. Zeek and R. Trebino, *Opt. Express*, 2004, **12**, 4399-4410.
29. G. D. Goodno and R. J. D. Miller, *J. Phys. Chem. A*, 1999, **103**, 10619-10629.
30. A. M. Nagy, V. Raicu and R. J. D. Miller, *Biochimica Et Biophysica Acta-Proteins and Proteomics*, 2005, **1749**, 148-172.
31. D. Kivelson and P. A. Madden, *Annu. Rev. Phys. Chem.*, 1980, **31**, 523-558.
32. R. Torre, P. Bartolini and R. Righini, *Nature*, 2004, **428**, 296-299.
33. E. L. Quitevis and M. Neelakandan, *J. Phys. Chem.*, 1996, **100**, 10005-10014.
34. J.-C. Diels and W. Rudolph, *Ultrashort Laser Pulse Phenomena*, Elsevier Inc., 2006.
35. G. E. Walrafen, *J. Chem. Phys.*, 1964, **40**, 3249.
36. E. W. Castner, Y. J. Chang, Y. C. Chu and G. E. Walrafen, *J. Chem. Phys.*, 1995, **102**, 653-659.
37. S. Saito and I. Ohmine, *J. Chem. Phys.*, 1997, **106**, 4889-4893.
38. N. A. Smith, S. J. Lin, S. R. Meech, H. Shirota and K. Yoshihara, *J. Phys. Chem. A*, 1997, **101**, 9578-9586.
39. Y. J. Chang and E. W. Castner, *J. Chem. Phys.*, 1993, **99**, 7289-7299.
40. M. Neelakandan, D. Pant and E. L. Quitevis, *J. Phys. Chem. A*, 1997, **101**, 2936-2945.
41. J. A. Bucaro and T. A. Litovitz, *J. Chem. Phys.*, 1971, **54**, 3846.
42. U. Kaatze and V. Uhlendorf, *Z Phys Chem Neue Fol*, 1981, **126**, 151-165.
43. M. N. Afsar and J. B. Hasted, *J Opt Soc Am*, 1977, **67**, 902-904.
44. C. J. Fecko, J. D. Eaves, J. J. Loparo, A. Tokmakoff and P. L. Geissler, *Science*, 2003, **301**, 1698-1702.
45. H. J. Bakker and J. L. Skinner, *Chem. Rev.*, 2010, **110**, 1498-1517.
46. A. Tokmakoff, R. A. Nicodemus, K. Ramasesha and S. T. Roberts, *J Phys Chem Lett*, 2010, **1**, 1068-1072.
47. J. Jonas, T. Defries and W. J. Lamb, *J. Chem. Phys.*, 1978, **68**, 2988-2989.
48. G. E. Walrafen, M. S. Hokmabadi and W. H. Yang, *J. Chem. Phys.*, 1986, **85**, 6964-6969.
49. C. Ronne, P. O. Astrand and S. R. Keiding, *Phys. Rev. Lett.*, 1999, **82**, 2888-2891.
50. K. Winkler, J. Lindner, H. Bursing and P. Vohringer, *J. Chem. Phys.*, 2000, **113**, 4674-4682.
51. W. F. Murphy, *J. Chem. Phys.*, 1977, **67**, 5877-5882.
52. K. Winkler, J. Lindner and P. Vohringer, *PCCP*, 2002, **4**, 2144-2155.
53. I. Ohmine and S. Saito, *Acc. Chem. Res.*, 1999, **32**, 741-749.
54. J. E. Bertie and E. Whalley, *J. Chem. Phys.*, 1967, **46**, 1271-&.
55. E. W. Lang and H. D. Ludemann, *Angew Chem Int Edit*, 1982, **21**, 315-329.
56. J. Marti, J. A. Padro and E. Guardia, *J. Chem. Phys.*, 1996, **105**, 639-649.
57. G. E. Walrafen, Y. C. Chu and G. J. Piermarini, *J Chem Phys*, 1996, **100**, 10363-10372.
58. A. Desantis, M. Sampoli, V. Mazzacurati and M. A. Ricci, *Chem. Phys. Lett.*, 1987, **133**, 381-384.
59. T. Nakayama, *Phys. Rev. Lett.*, 1998, **80**, 1244-1247.
60. G. E. Walrafen, *J. Phys. Chem.*, 1990, **94**, 2237-2239.

61. S. Palese, L. Schilling, R. J. D. Miller, P. R. Staver and W. T. Lotshaw, *J Phys Chem*, 1994, **98**, 6308-6316.
62. D. Laage and J. T. Hynes, *Science*, 2006, **311**, 832-835.
63. M. A. Ricci, G. Signorelli and V. Mazzacurati, *J Phys-Condens Mat*, 1990, **2**, Sa183-Sa187.
64. P. Benassi, V. Mazzacurati, M. Nardone, M. A. Ricci, G. Ruocco, A. Desantis, R. Frattini and M. Sampoli, *Mol. Phys.*, 1987, **62**, 1467-1481.
65. P. A. Madden and R. W. Impey, *Chem. Phys. Lett.*, 1986, **123**, 502-506.
66. M. Khalil, O. Golonzka, N. Demirdoven, C. J. Fecko and A. Tokmakoff, *Chem. Phys. Lett.*, 2000, **321**, 231-237.
67. G. E. Walrafen, *Water:A Comprehensive Treastise*, Plenum, New York, 1972.
68. *Handbook of Chemistry and Physics*, CRC Press, 2004.
69. C. Okpala, A. Guiseppielie and D. M. Maharajh, *J. Chem. Eng. Data*, 1980, **25**, 384-386.
70. R. Sinibaldi, C. Casieri, S. Melchionna, G. Onori, A. L. Segre, S. Viel, L. Mannina and F. De Luca, *J. Phys. Chem. B*, 2006, **110**, 8885-8892.
71. S. Taniewskaosinska, A. Piekarska and A. Kacperska, *J. Solution Chem.*, 1983, **12**, 717-727.

Chapter 3

Ultrafast Dynamics of Aqueous Alkali Halide Solutions

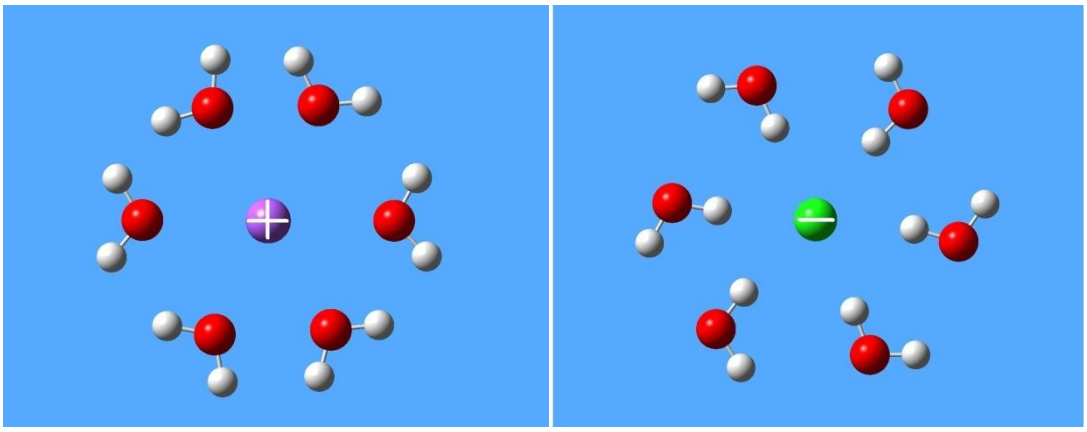

In this chapter anisotropic and isotropic responses of a variety of aqueous salt solutions in both the time and frequency domain are described. Vibrational modes associated with solvation structure are observed in the isotropic response. These modes are assigned with the help of density functional theory, DFT.

3.1 Introduction

The understanding of ion solvation is of great importance in chemistry and biology.[1-4] The addition of salt to water changes many of its macroscopic properties: viscosity increases, melting and boiling points change.[5, 6] When electrolytes are added to water they dissociate into ions. The electric field of the ions causes water molecules to rearrange themselves in the hydration shell. The hydration shell differs from the structure of bulk water. Neutron diffraction measurements[7, 8] of ionic liquids showed that the cation binds to the water oxygen atom while the water hydrogen atoms point away from the ion. Anions on the other hand form a hydrogen bond with water's hydrogen.

In recent years many theoretical and experimental techniques were used to investigate the solvation structure of ions in water and the dynamics of water in salt solutions.[9-14] Still however, the structure and dynamics of salt solutions are not fully understood. There is currently no uniform view on the number of water molecules in the first hydration shell of ions, as different experimental techniques give different results,[15, 16] e.g. coordination number of I^- varies from approximately 4 obtained by Monte Carlo simulation[12] to 6-9 obtained by X-ray diffraction.[17, 18] The effect of ions on the water structure is probably not only restricted to the rearrangement of water in the first hydration shells of ions. Mancinelli *et al.*[19, 20] using neutron diffraction data showed that ions can affect the structure of water well outside their first hydration shell (up to

third hydration shell), either enhancing or weakening water structure. In contrast Bakker *et al.*[21] using IR spectroscopy established a negligible effect of ions beyond the first hydration shell on the water structure. However this result is still a matter of debate. Molecular dynamics simulations[22] showed that water molecules beyond the first hydration shell of the ion are significantly influenced by the presence of ions, supporting the neutron diffraction data.[19] The effect of ions on water structure has lead to the idea of structure making or breaking properties. Small and multiple charged ions are denoted as structure makers as it is believed that they induce strengthening of the water H-bonds. In contrast large, monovalent ions are believed to cause a weakening of water H-bonds and are therefore classified as structure breakers.[23] The structure making and breaking ability is largely based on the measurements of viscosity *B*-coefficients.[5, 24] The *B*-coefficients in the Jones-Dole equation: $\eta/\eta_0 = 1 + A\sqrt{c} + Bc$, where c denotes concentration, η/η_0 is the concentration-dependent viscosity, can be determined experimentally or estimated theoretically.[5] A describes interionic forces and B depends on the ion-solvent interactions and is related to the ion volume.[5] The sign of the *B*-coefficient determines whether the ion is a structure breaker or maker, with negative (positive) *B*-coefficients indicating structure breaking (making) abilities, respectively.[5] Jenkins *et al.*[5] found the following *B*-coefficients for cations: Li^+; 0.146, Na^+; 0.085, K^+; -0.009, Mg^{2+}; 0.385, Ca^{2+}; 0.284, Al^{3+}; 0.744, and anions: Cl^-; -0.005, Br^-; -0.033, I^-; -0.073. From these values it is immediately evident that the I^- is expected to disrupt water structure to the greatest extent while triply charge Al^{3+} has the largest water structure making capability.

Recently, 2DIR spectroscopy studies[23] of electrolyte solutions revealed the existence of relaxation times spanning from hundreds of femtoseconds to several picoseconds.

The fastest response observed was assigned to local fluctuations in the H-bond length.[23, 25] The relaxation dynamics revealed a dependence on ion concentration. As concentration increases, the water-ion H-bond dynamics became dominant over water-water H-bond dynamics. However, the H-bond mode itself, its concentration dependence and the effect of cation is not yet fully characterized.

Many important low frequency Raman measurements of aqueous salt solutions have been reported. The key assignment of the low frequency part of the depolarized spectra was made by the groups of Walrafen[26] and Tominaga.[27] Walrafen *et al.*[26] reported that addition of salt induces the breakdown of intermolecular structure, *i.e.* of O-H···O bonds. Tominaga *et al.*[28] found that the relaxation time, τ (defined by Cole-Cole type relaxation $\chi(\omega) = 1/\left[1 + (i\omega\tau)^{\beta}\right]$) and viscosity of electrolyte solutions are strongly correlated. They associated the relaxation time recovered in their studies with structural relaxation motion of the bulk water clusters consisting of five water molecules. Furthermore it was concluded that O···H-O stretching vibrations become weaker with the addition of salt, but the bending mode of O···H-O is hardly affected. Salt solutions however have intrinsically low scattering intensities, which means that many of the reported spectra are noisy. Furthermore low frequency Raman spectra are distorted by the thermal population of low frequency modes, which can lead to signal-to-noise degradation, particularly below 100 cm^{-1}. The salt solutions with differently charged cations were also studied recently by means of dielectric relaxation and OKE spectroscopy by Turton *et al.*[9] They found that the salt solutions exhibit the behaviour of supercooled liquids approaching a glass transition, in which the translational and rotational relaxations are decoupled. In this chapter isotropic and anisotropic OKE data for a great variety of alkali halide salt solutions are presented. One series of measurements contained the sodium ion as a cation and the halide anion was varied

(Na^+X^- where X=Cl, Br and I). In the second group of measurements the chloride anion was fixed and the cation varied ($M^{n+}Cl_n^-$, where M=Li, Na, K, Mg, Ca and Al).

3.2. Time Domain Analysis

Here the time domain data of both the anisotropic and the isotropic OKE response are presented. The anisotropic response is characterized by slow picosecond dynamics and the fast H-bonded modes of water, while in the isotropic response the dominant feature constitutes a subpicosecond oscillation.

3.2.1. Anisotropic Response

The time domain data of NaCl as a function of concentration and a comparison of NaCl, NaBr, NaI at 6 M concentration are shown in Figure 3.1. All data were normalized to the electronic response at t = 0 ps. The concentration dependence of NaBr and NaI is similar to that of NaCl and is therefore not shown. It is clear that with the addition of salts the picosecond relaxation time increases. To quantify this, each trace beyond 1 ps was fit to the biexponential function (Eq. 2.34) and the averaged relaxation time was calculated (Eq. 2.35). Average relaxation time results are plotted in Figure 3.1c and the individual fitting parameters are listed in Table 3.1. Immediately evident is that for salt solutions having the same cation (Na^+) averaged relaxation times are similar at a given concentration, independent of the halide ion. A difference in relaxation times between salt solutions at the same concentration was observed when the chloride anion remained fixed, and cations varied, Figure 3.1d. Monovalent K^+ and Na^+ exhibit similar relaxation times. Divalent Mg^{2+} and Ca^{2+} also exhibit similar dynamics but are markedly slower than monovalent cations. The slowest relaxation was observed for trivalent Al^{3+}. The relaxation times observed here have an intermolecular interaction induced (II) origin, see chapter 2 for details.

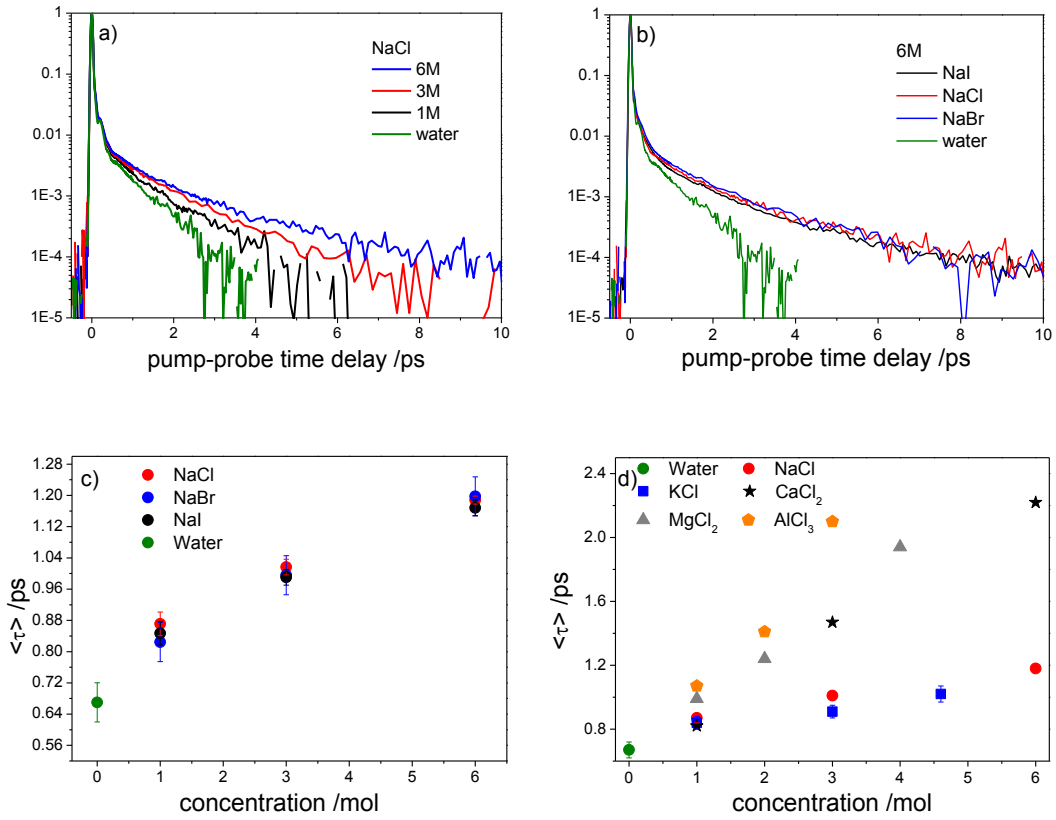

Figure 3.1 Time domain response of pure water (green) with a) increasing concentration of NaCl and b) comparison of NaCl, NaBr, NaI at 6 M, c) and d) mean relaxation time plotted against concentration.

This means that the observed signal is due to translational and translational-rotational intermolecular interactions. Turton *et al.*[9] and Tominaga *et al.*[28] showed that such slow dynamics are correlated with solution viscosity, with $AlCl_3$ having the largest viscosity and so being expected to show the slowest dynamics. Similarly, KCl having the lowest viscosity[28] is expected to exhibit the fastest dynamics, Figure 3.1d. Turton *et al.*[9] in their comparison of OKE data with dielectric relaxation, proposed that salt solutions behave like supercooled liquids approaching a glass transition. In this state, rotational and translational motions are decoupled and the "jamming" process was assigned as being responsible for the viscosity increase and slow dynamics.

	$a_1/(a_1+a_2)$	τ_1/ps	$a_2/(a_2+a_1)$	τ_2/ps	$\langle\tau\rangle$/ps
water	0.80	0.46	0.20	1.42	0.67
NaCl 1M	0.87	0.70	0.13	2.07	0.87
NaCl 3M	0.85	0.77	0.15	2.42	1.01
NaCl 6M	0.79	0.77	0.21	2.81	1.18
KCl 1M	0.88	0.68	0.12	2.16	0.84
KCl 3M	0.87	0.69	0.13	2.46	0.91
KCl 4.6M	0.87	0.75	0.13	2.65	1.02
NaBr 1M	0.88	0.65	0.12	2.11	0.82
NaBr 3M	0.85	0.76	0.15	2.41	0.99
NaBr 6M	0.80	0.82	0.20	2.77	1.19
NaI 1M	0.84	0.63	0.16	2.00	0.84
NaI 3M	0.84	0.72	0.16	2.46	0.99
NaI 6M	0.79	0.77	0.21	2.71	1.16
$MgCl_2$ 1M	0.83	0.67	0.17	2.67	0.99
$MgCl_2$ 2M	0.75	0.69	0.25	2.95	1.24
$MgCl_2$ 4M	0.72	0.86	0.28	4.80	1.94
$CaCl_2$ 1M	0.78	0.54	0.22	1.85	0.82
$CaCl_2$ 3M	0.79	0.73	0.21	4.31	1.47
$CaCl_2$ 6M	0.70	0.91	0.30	5.40	2.22
$AlCl_3$ 1M	0.79	0.65	0.21	2.71	1.07
$AlCl_3$ 2M	0.75	0.71	0.25	3.09	1.41
$AlCl_3$ 3M	0.73	0.90	0.27	5.39	2.10

Table 3.1 Fitting parameters to Eq. 2.34.

3.2.2 Isotropic Response

The isotropic OKE traces for NaCl with increasing concentration are shown in Figure 3.2a and the comparison of Na^+ with different anions in Figure 3.2b. After addition of NaCl to water, a well defined under-damped oscillation appears, which grows in amplitude with increasing concentration. This oscillation is absent in the bulk water response, Figure 3.2a. Thus, the new mode must be associated with the structures which ions and water form in the solution. Solutions of Na^+ and different anions also showed existence of such a mode. Earlier studies established[29] that the observed mode is due to $OH\cdots X^-$ stretching, where X = F, Cl, Br or I.

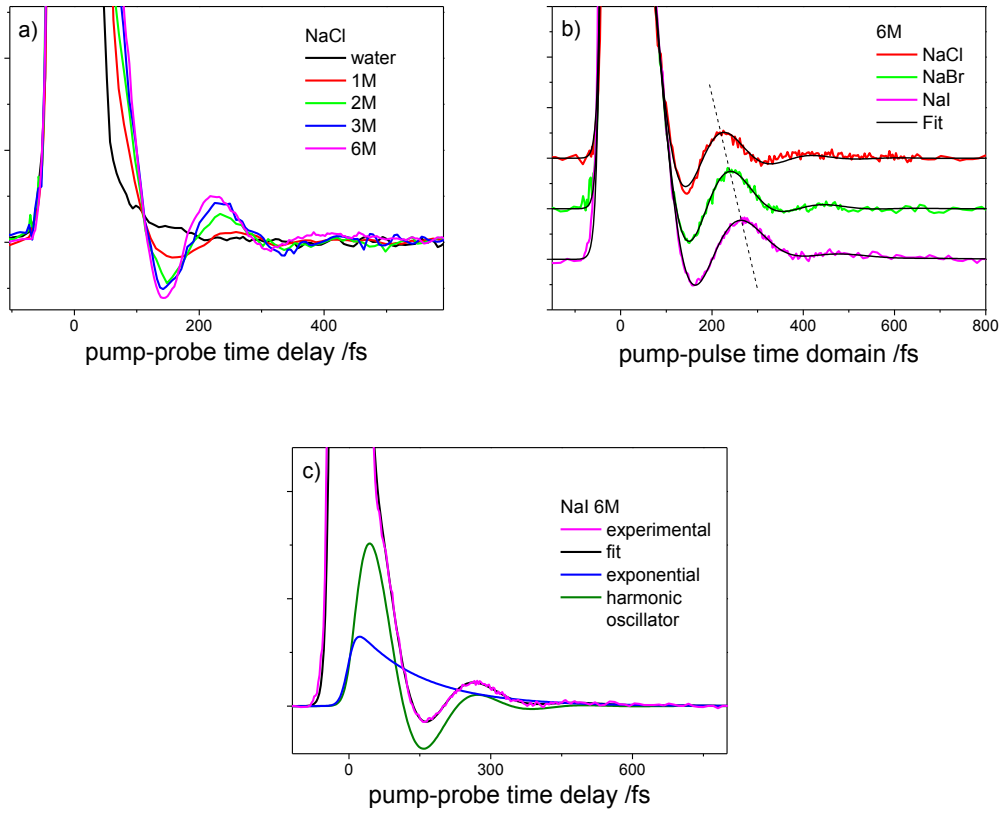

Figure 3.2 Isotropic response of salt solutions, a) concentration dependence of NaCl, and b)6 M solutions of NaCl, NaBr and NaI.c) Quality of fit to NaI 6M.

The time domain data were fitted with the sum of a damped harmonic oscillator and an exponential function:

$$r(t) = A\exp\left(-t/\tau_r\right) + B\exp(-t/\tau_D)\sin\omega t \qquad (3.1)$$

where A, B are relative amplitudes, the exponential relaxation time is denoted by τ_r, τ_D is the harmonic oscillator damping constant, and ω denotes the frequency. The quality of the fit is shown in Figure 3.2b and c. All fitting parameters, except ω are given in Table 3.2. ω will be discussed in the frequency domain in section 3.3.2.

The exponential relaxation times (τ_r) recovered from the fit gave values significantly longer than for bulk water, with the shortest time observed for NaCl solutions and the

longest for NaI. The relaxation times recovered from the anisotropic response gave similar values for all NaX^- solutions, indicating that the relaxation times observed in isotropic and anisotropic measurements are of different origin. One possibility might be that the isotropic response of water originates from a higher order of DID interactions, whereas the anisotropic response arises from the first order of DID interactions. The other possibility is that the anisotropic part of the polarizability β is nonzero, with the result that the $\Pi^{M,\beta}$ term of the collective anisotropic polarizability contributes to the anisotropic OKE response, while $\alpha\beta$ coupling contributes to the isotropic, see chapter 2.

The harmonic oscillator damping constants, τ_D have values between 53 fs and 91 fs for different alkali halide solutions. These times approximately match the ultrafast component reported for the spectral diffusion of the OH oscillator, which arises from fluctuations in the ion-water H-bond.[25]

	NaCl			**NaBr**			**NaI**		
	1M	3M	6M	1M	3M	6M	1M	3M	6M
τ_D **/fs**	72	99	92	87	86	90	74	91	85
τ_r **/fs**	56	63	60	71	96	95	122	107	138
A/(A+B)	0.39	0.49	0.90	0.35	0.22	0.04	0.13	0.22	0.21
B/(B+A)	0.61	0.51	0.10	0.65	0.78	0.96	0.87	0.78	0.79

Table 3.2 Fitting parameters to isotropic time domain, with water τ_r=47 fs.

3.3. Frequency Domain Analysis

The subpicosecond response of anisotropic OKE data is more conveniently analysed in the frequency domain. Therefore the ultrafast response of salt solutions will be described in the frequency domain applying the FT procedure described in section 2.4.2. The concentration dependence of the mode associated with the oscillation due

to water-ion interaction is discussed in the frequency domain of the isotropic response.

3.3.1. Anisotropic Response

As the picosecond response was already analysed in the time domain, the long tail associated with this response was subtracted from OKE data prior to transformation to the frequency domain, as described in section 2.4. This was done to highlight the intermolecular mode in the low frequency part of the spectrum. The resulting reduced spectral densities of water and NaCl solutions at different concentrations are shown in Figure 3.3a. It is immediately evident that with an increase in concentration the integrated spectral amplitude at wavenumbers below 200 cm^{-1} increases. To compare the effect of different anions on the water spectra, peak normalized spectra of NaCl, NaBr and NaI data are plotted in Figure 3.3b.

With replacement of the anion the mode at around 172 cm^{-1}, which is assigned to a H-bond stretching mode in pure water changes dramatically. This mode appears to shift to a lower frequency, with the biggest shift observed for the heaviest iodide ion. Tominaga *et al.*[28] suggested that this red shift is due to weakening of the water-water H-bonds and disruption of tetrahedral water structure. The effect of the anions on the water structure is in line with the structure breaking ability of large anions, with I^- having the largest B coefficient.[5] B-coefficient indicates that the iodide will affect the water structure the most and chloride the least.[5]

To obtain some more details about the magnitude of the mode shift, we fitted the spectral densities with three functions (BL, G, ASG) (Eq. 2.37-2.39). The quality of fit and the frequency components are shown in Figure 3.4 and fitting parameters are listed in Table 3.3. The highest frequency mode was fitted with an antisymmetrized

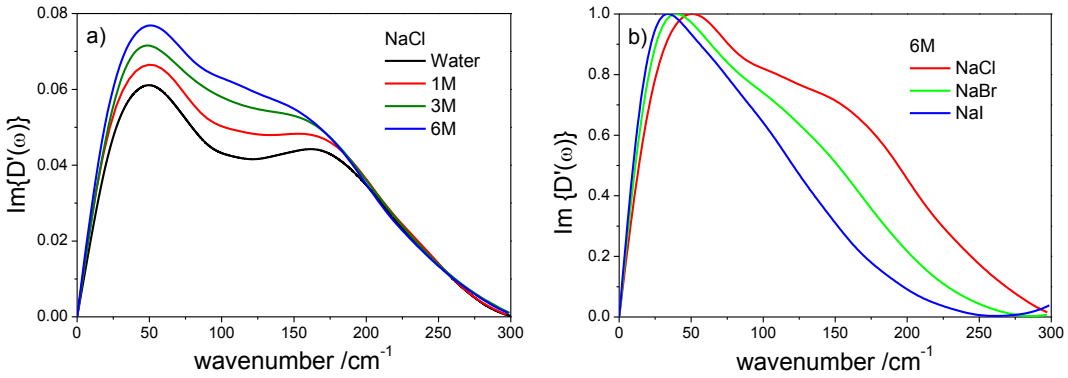

Figure 3.3. Spectral density of a) NaCl solutions at different concentration and b) normalized NaCl, NaBr and NaI at 6 M.

Gaussian (ASG) mode. This mode was fixed for fitting at the water frequency of 172 cm^{-1} with a bandwidth of 127 cm^{-1}, allowing only the amplitude to vary. This component was thus associated with the unperturbed water structure in the solution and was kept fixed in order to assess if there is a new contribution appearing, which has its origin in ion-water interactions. Depolarized ion-water mode was previously observed by means of Raman spectroscopy by Walrafen *et al.*[30]

The lowest frequency mode fitted with the Bucaro-Litovitz (BL) function shifts to the red with increasing concentration, with the biggest shift observed for the halide ion

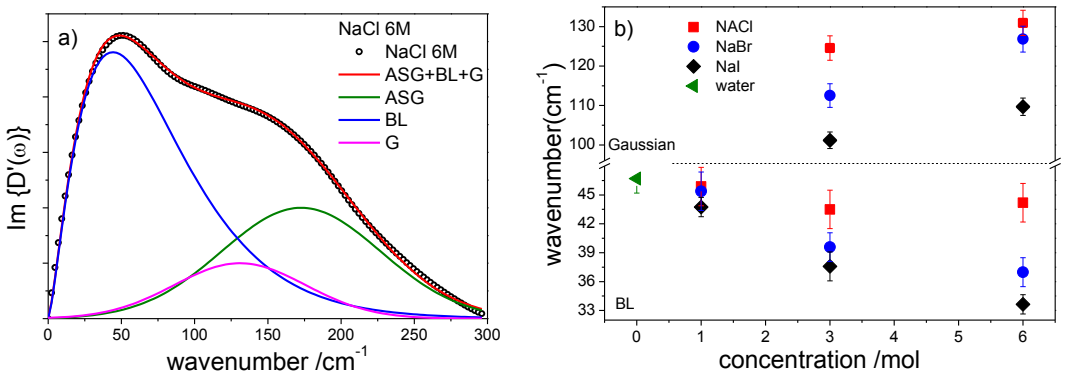

Figure 3.4. a) Quality of fit to NaCl 6M solution, b) wavenumber plotted against concentration.

	NaCl			NaBr			NaI			water
	1M	3M	6M	1M	3M	6M	1M	3M	6M	
BL										
A_{BL}	0.065	0.070	0.090	0.070	0.090	0.120	0.086	0.12	0.18	0.055
α	1.51	1.40	1.41	1.24	1.25	1.22	1.35	1.10	1.17	1.80
ω_{BL}/cm^{-1}	30.3	31.0	31.3	36.6	31.6	30.3	32.4	34.1	28.7	25.57
G										
A_G	-	0.016	0.020	-	0.021	0.049	-	0.021	0.056	-
ω_G /cm^{-1}	-	124.5	130.9	-	112.5	126.8	-	101.1	109.6	-
$\Delta\omega_G$ /cm^{-1}	-	131.1	105.5	-	103.1	115.7	-	102.8	99.4	-
ASG										
A_{ASG}	0.040	0.037	0.040	0.039	0.036	0.008	0.042	0.022	0.007	0.040
ω_{ASG} /cm^{-1}	172.7	172.7	172.7	172.7	172.7	172.7	172.7	172.7	172.7	172.7
$\Delta\omega_{ASG}$ /cm^{-1}	127.9	127.9	127.9	127.9	127.9	127.9	127.9	127.9	127.9	127.9
integrated areas										
I_{BL}	0.56	0.45	0.56	0.58	0.63	0.56	0.60	0.69	0.64	0.45
I_G	-	0.12	0.18	-	0.09	0.37		0.12	0.31	-
I_{ASG}	0.44	0.43	0.26	0.42	0.28	0.07	0.40	0.19	0.05	0.55

Table 3.3 Fitting parameters to spectral densities of salts. Integrated areas are the relative weights of integrated areas given by : $I_i = \frac{I_i}{I_{TOT}}$ *, where i is either BL, ASG or G and* I_{TOT} *is the total integrated area of the RSD.*

with the highest atomic weight. This shift is clear if we compare normalized spectra at a given concentration, Figure 3.3b.

The middle component fitted with a Gaussian function we associate with ion-water interactions. This component appears only at 3M concentration and above, indicating that at low (1M) concentration the anisotropic signal is dominated by the water-water contribution. We performed DFT calculations using Gaussian03 at the level of theory B3LYP/6-311++G for $Br^-(H_2O)_5$ and $Cl^-(H_2O)_5$ complexes. One such structure is shown in Figure 3.5a. We found depolarized Raman modes at 113 and 109 cm^{-1} for Cl^- and Br^-, Figure 3.5b. These frequencies are consistent with the frequency of the Gaussian component recovered from the fit. Again, the lowest frequency is observed for the heavier iodide ion. Amplitudes of fitted functions are listed in Table 3.3. As DFT calculations performed using Gaussian03 do not provide direct anisotropic

spectra, but instead give the depolarization ratio and Raman activity values, the Raman anisotropic intensity was calculated from the relation:[31]

$$I_{ANISO} = \left(1 - \frac{3-4\rho}{3(1+\rho)} I_{RA}\right) \tag{3.2}$$

where ρ is the depolarization ratio and I_{RA} is the Raman activity.

DFT calculations were performed for various configurations of ion-water complexes (different number of water molecules and different positions of water molecules around ion). The correct ion-water structure was chosen as the one for which frequency of isotropic mode was the closest to the frequency obtained experimentally and which had the largest intensity, see below.

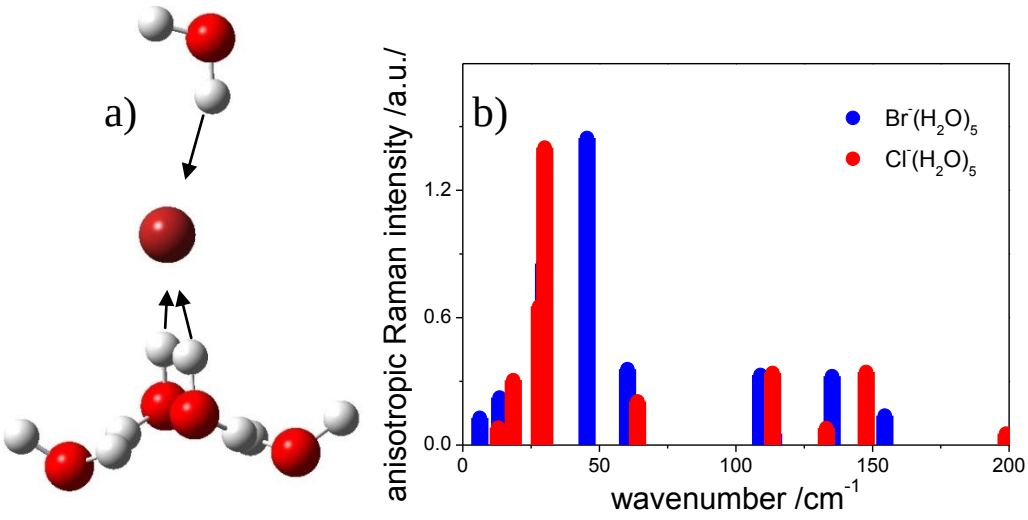

Figure 3.5. a) Optimized structure of $Br^-(H_2O)_5$ complex, obtained from DFT calculations, b) anisotropic Raman frequencies for $Br^-(H_2O)_5$ and $Cl^-(H_2O)_5$ obtained from DFT. Arrows denote water displacement during vibration.

There is a number of low frequency anisotropic modes observed in the calculated Raman spectrum, Figure 3.5b. However the calculation was performed for the gas

phase while experiment was carried out for the solution. It is possible that in the solution, the relative amplitude between modes is different than in the gas phase. The strong band in Figure 3.5b might also not be observed in OKE as it overlaps with the ~ 45 cm^{-1} band associated with H-bond bend of water molecules.

3.3.2 Isotropic Response

The isotropic spectra of water and NaCl solutions are shown in Figure 3.6. The mode present in solutions spectral densities at ~(140 cm^{-1} – 170 cm^{-1}) is associated with the new oscillatory feature observed in the time domain (Figure 3.2), which is in turn associated with a water-ion mode. The DFT calculation for the asymmetric solvated $Br^{-}(H_2O)_5$ structure (Figure 3.5) showed one clear isotropic mode at 135 cm^{-1} associated with a H-bond stretching mode, Figure 3.7.

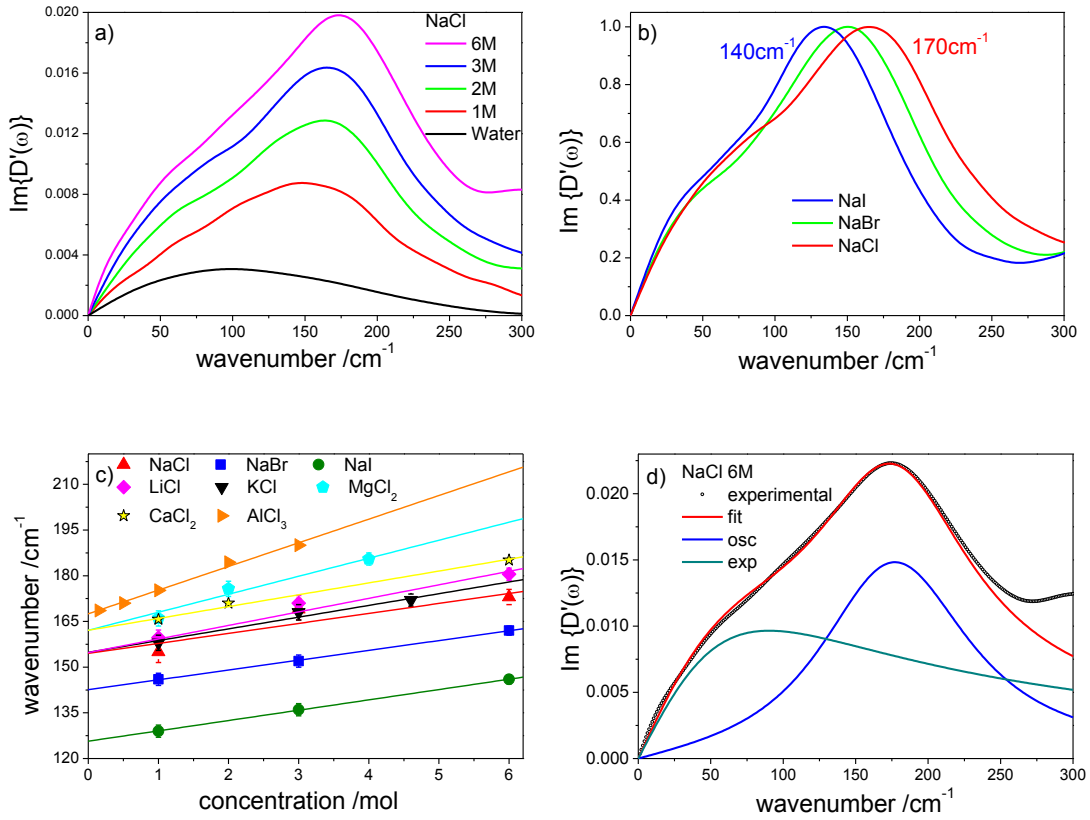

Figure 3.6 a) comparison of water spectrum with NaCl solution spectra, b) comparison of 6 M solutions of NaCl, NaBr and NaI and c) frequency parameter obtained from fitting and d) quality of fit to Eq.3.1.

Raman isotropic intensity was calculated from the relations:[31]

$$I_{ISO} = \frac{3-4\rho}{3(1+\rho)} I_{RA} \tag{3.3}$$

where ρ is the depolarization ratio and I_{RA} is the Raman activity.

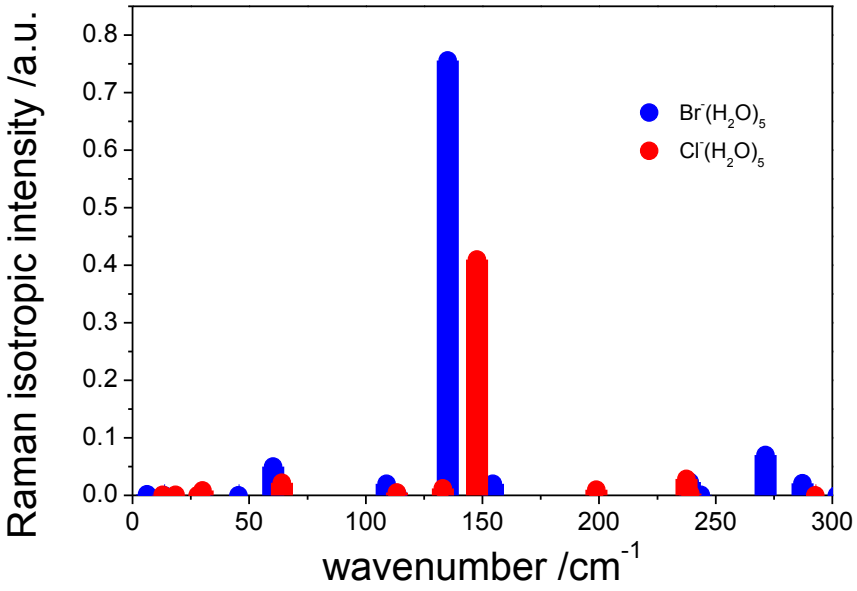

Figure 3.7 Isotropic frequencies for $Br^-(H_2O)_5$ and $Cl^-(H_2O)_5$ complex obtained from DFT calculations.

This isotropic anion-water H-bond mode grows in amplitude with addition of salt (Figure 3.6a). Frequency parameters obtained from the fit to the time domain data are plotted in Figure 3.6c. Two trends are immediately evident. Firstly, the mode frequency increases with increasing concentration and secondly the observed frequency decreases with increasing atomic weight of the anion. However, extrapolation to a zero concentration value is cation and anion dependent. This arises in the manner that monovalent K^+, Na^+ and Li^+ share a common zero concentration frequency, and bivalent Mg^{2+}, and Ca^{2+} also share a common zero concentration frequency (higher frequency than the monovalent cations). No common zero

concentration frequency was observed for NaCl, NaBr and NaI and linear fit to the frequencies of these solutions are almost parallel.

An important question to be addressed is whether the lower frequency of the $X^-\cdots HOH$ stretch for heavier anions is due to a mass effect or to a weaker H-bond. Two models were applied to estimate the force constant of the ion-water H-bond.

In the first model, we assumed that the anion and water act as a diatomic-like harmonic oscillator system with a calculated force constant from $2\pi\nu = (k/\mu)^{1/2}$, where μ is the reduced mass and water is treated as an atom of mass 18 amu. The frequency taken for the calculation was the frequency at infinite dilution. Calculated values are given in Table 3.4. The isotropic water spectrum does not have a well defined mode, so to calculate a force constant for pure water, the frequency from the depolarized spectrum was used, 172 cm^{-1}. This gave a value of 15.7 Nm^{-1}, which is in a good agreement with previously published results,[32] where the force constant of the water-water stretching mode was estimated to be 10-20 Nm^{-1}. From the calculated values it is clear that the force constant for anion-water H-bonds are of the same magnitude as for pure water. The chloride values are somewhat larger and iodide slightly smaller than the water value. This indicates that chloride ions form stronger H-bonds and iodide ions slightly weaker H-bonds than water-water. This is in agreement with previous studies.[33, 34]

The second model investigated was a linear XYZ system in which X = Cl^-, Br^-, I^- and Y and Z are H and O, respectively.[35] The force constants were calculated from the following relations:

$$4\pi^2(\nu_1^2+\nu_3^2)=k_1\left(\frac{1}{m_X}+\frac{1}{m_Y}\right)+k_2\left(\frac{1}{m_Y}+\frac{1}{m_Z}\right) \quad (3.4)$$

$$16\pi^4\nu_1^2\nu_3^2=\frac{m_X+m_Y+m_Z}{m_Xm_Ym_Z}k_1k_2 \quad (3.5)$$

where m_i denotes atomic mass of X, Y or Z atom. k_1 and is the force constant of the H-bond formed between the anion and water, k_2 is the force constant of the O-H bond. ν_1 is the frequency of $X^-\cdots OH$ mode and ν_2 is the stretching frequency of the O-H bond, 3480 cm^{-1}. The results obtained from this analysis are listed in Table 3.4. The values obtained are similar to those recovered from the diatomic model. Similarly the same trend was observed, the force constant decreases with increasing anion weight and size, indicating weakening of the anion-water H-bonds.

It is clear that the linear fit to the chloride frequency extrapolates to different values at the infinite dilution (Figure 3.6c), and that the infinite dilution value is a function of the cation's charge. The frequency shift caused by different cations is reflected in the slope of the fitting line. The largest slope was recovered for Al^{3+} which also has the highest charge, indicating that Al^{3+} affect the ion-water frequency the most. The cation with the second biggest effect is the doubly charged Mg^{2+} followed by Ca^{2+}. The smallest effect on the frequency shift is exerted by K^+ and Na^+.

At concentrations greater than 1M, there are less than 27 water molecules per ion, and the first hydration shell of each ion consists of about 6 water molecules. At 6M concentration there are between four and five water molecules per ion, thus most water molecules in the first hydration shell will be H-bonded to water molecules in the first hydration shell of another ion. It is possible that the cation affects the

	reduced mass μ/amu	***frequency ν/cm^{-1}***	***diatomic model k/Nm^{-1}***	***XYZ model k/Nm^{-1}***	***slope Δ/cm^{-1}M^{-1}***
$Li^+\cdots H_2O\cdots Cl^-$	11.9	155	16.9	16.6	4.4±0.3
$Na^+\cdots H_2O\cdots Cl^-$	11.9	155	16.9	16.6	3.3±0.6
$K^+\cdots H_2O\cdots Cl^-$	11.9	155	16.9	16.6	3.8±0.3
$Ca^{2+}\cdots H_2O\cdots Cl^-$	11.9	162	18.5	18.2	3.9±0.2
$Mg^{2+}\cdots H_2O\cdots Cl^-$	11.9	162	18.5	18.2	5.9±0.4
$Al^{3+}\cdots H_2O\cdots Cl^-$	11.9	167	19.6	19.4	7.8±0.4
$Na^+\cdots H_2O\cdots Br^-$	14.7	143	17.7	17.3	3.2±0.1
$Na^+\cdots H_2O\cdots I^-$	15.7	126	14.6	14.3	3.4±0.1
$H_2O\cdots H_2O$	9.0	172	15.7	14.7	

Table 3.4 Calculated force constants adapting the diatomic and XYZ model. See text for details.

properties of the anion-ion mode in a number of ways. As the charge of the cation increases the electric field exerted on the anion-water mode increases. This may lead to a shifting of the anion-water mode to higher frequency.

The influence of the electric field of a dissolved ion on the vibrational frequency of water OH modes was studied by Geissler *et al.*[12] They found that the electric field of an ion affects the stretching mode of water OH when the H atom is directly bound to the ion. Our data may also be a manifestation of this phenomenon, with the mode affected in our studies being $OH\cdots X^-$. The shift of the ion-water mode to the higher frequency with increasing concentration might also indicate an increase in strength of the H-bond between water and anion. Such an effect might arise from structural changes in the anion hydration shell as a result of cation solvation.

For the $MgCl_2$, $AlCl_3$ and $LiCl_3$ a second harmonic oscillator was needed to fit the isotropic temporal response. The representative data are shown in Figure 3.8.

This new oscillation appears as a mode at 524 cm^{-1}, 353 cm^{-1} and 250 cm^{-1} in the frequency domain for $AlCl_3$, $MgCl_2$ and LiCl, respectively. The appearance of this mode is due to the $M^{n+}\cdots OH_2$ polarized mode associated with symmetric stretching of

an ion-water H-bond. The polarized mode of $Al^{3+}\cdots OH_2$ was observed before in frequency domain Raman measurements.[36] The high frequency mode observed for the

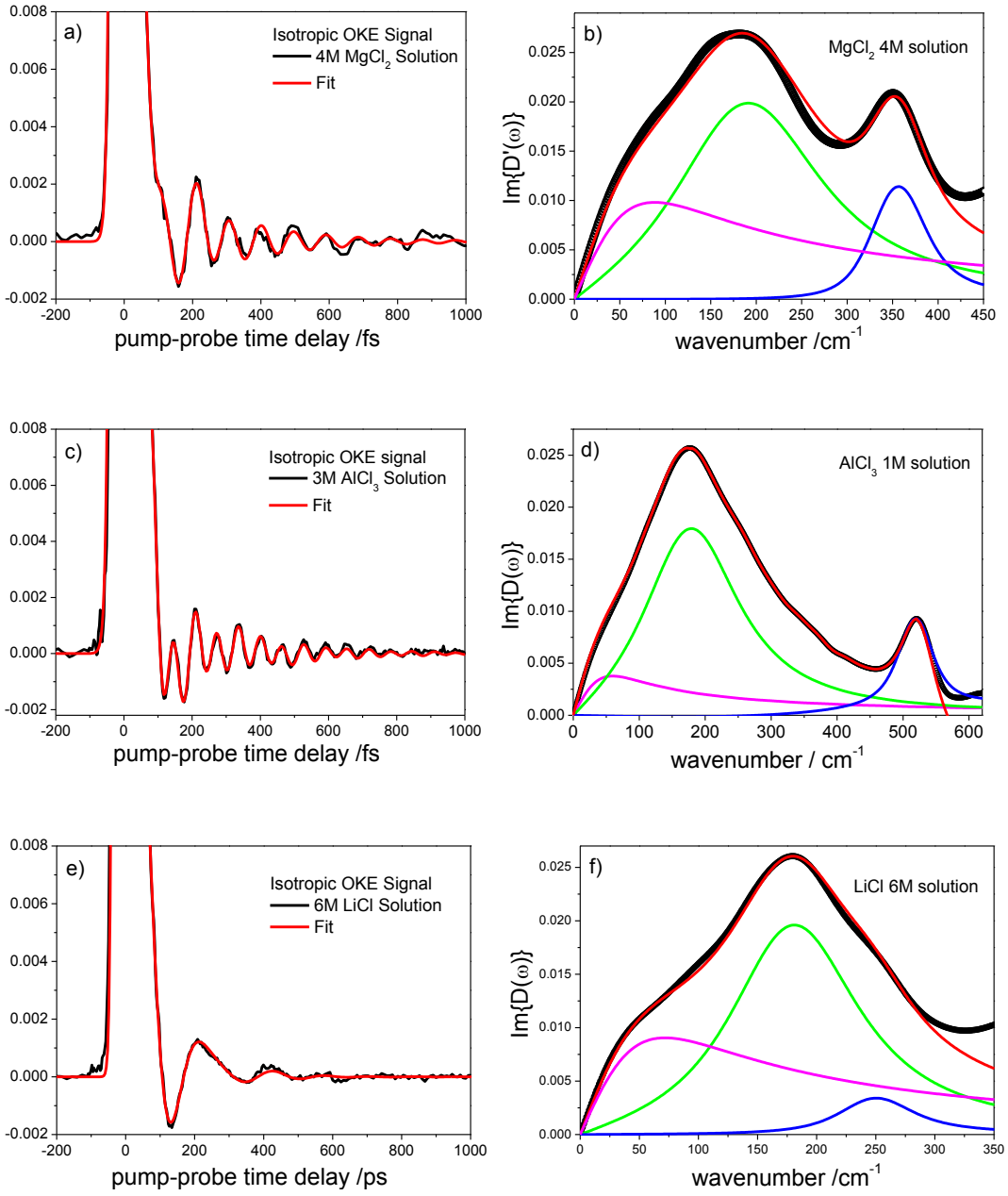

Figure 3.8. Time domain isotropic data to $AlCl_3$, $MgCl_2$ and LiCl its representation in frequency domain. Magenta, green and blue lines are the fitting functions.

$MgCl_2$ solutions is also in agreement with previously published experimental and molecular dynamics data.[36] Bouř *et. al*[37] using CPMD calculations found that the magnesium cation binds water strongly, forming a stable octahedral six-water

hydration shell which supports low frequency polarized Raman mode. Their calculations also showed[37] that for the hydrated calcium cation a mode at 262 cm^{-1} should appear, although its amplitude should be approximately five times smaller than the one of magnesium. Also, hydrated sodium and potassium cations were calculated to produce polarized low frequency modes in the region of 170 cm^{-1} but with roughly 100 times less amplitude compared to a magnesium mode. These modes were not observed as they expect to overlap with anion-water modes.

3.4 Conclusions

The anisotropic and isotropic response of a series of aqueous alkali halide salt solutions at wide range of concentrations were studied by means of OKE spectroscopy. A low frequency anion-water mode was observed in the isotropic Raman spectral density. This mode was assigned to symmetric stretching of an ion-water H-bond. It was observed that this mode shifts to higher frequency with increasing salt concentration and it was suggested that this shift is associated either with an electric field exerted on the vibration by a nearby cation or by a concentration dependent solvation structure. From analysis of the anisotropic response it was concluded that larger anions perturb the tetrahedral structure of water to a larger extent than the small Cl^-.

3.5 References

1. C. Hartnig and M. T. M. Koper, *J. Am. Chem. Soc.*, 2003, **125**, 9840-9845.
2. J. Ranke, A. Othman, P. Fan and A. Muller, *Int J Mol Sci*, 2009, **10**, 1271-1289.
3. K. Ando and J. T. Hynes, *Adv Chem Phys*, 1999, **110**, 381-430.
4. P. Ball, *Chem. Rev.*, 2008, **108**, 74-108.
5. H. D. B. Jenkins and Y. Marcus, *Chem. Rev.*, 1995, **95**, 2695-2724.
6. *Handbook of Chemistry and Physics*, CRC Press, 2004.
7. D. H. Powell, G. W. Neilson and J. E. Enderby, *J Phys-Condens Mat*, 1993, **5**, 5723-5730.

8. G. W. Neilson, P. E. Mason, S. Ramos and D. Sullivan, *Philos T R Soc A*, 2001, **359**, 1575-1591.
9. D. A. Turton, J. Hunger, G. Hefter, R. Buchner and K. Wynne, *Journal of Chemical Physics*, 2008, **128**, 161102.
10. S. R. Meech, I. A. Heisler and K. Mazur, *J. Phys. Chem. B*, 2011, **115**, 1863-1873.
11. W. H. Robertson and M. A. Johnson, *Annu. Rev. Phys. Chem.*, 2003, **54**, 173-213.
12. P. L. Geissler, J. D. Smith and R. J. Saykally, *J. Am. Chem. Soc.*, 2007, **129**, 13847-13856.
13. K. J. Tielrooij, J. Hunger, R. Buchner, M. Bonn and H. J. Bakker, *J. Am. Chem. Soc.*, 2010, **132**, 15671-15678.
14. S. Raugei and M. L. Klein, *J. Chem. Phys.*, 2002, **116**, 196-202.
15. H. Ohtaki and T. Radnai, *Chem. Rev.*, 1993, **93**, 1157-1204.
16. Y. Marcus, *Chem. Rev.*, 2009, **109**, 1346-1370.
17. R. M. Lawrence and R. F. Kruh, *Journal of Chemical Physics*, 1967, **47**, 4758-&.
18. G. Markovich, R. Giniger, M. Levin and O. Cheshnovsky, *Journal of Chemical Physics*, 1991, **95**, 9416-9419.
19. M. A. Ricci, R. Mancinelli, A. Botti, F. Bruni and A. K. Soper, *J. Phys. Chem. B*, 2007, **111**, 13570-13577.
20. R. Mancinelli, A. Botti, F. Bruni, M. A. Ricci and A. K. Soper, *Physical Chemistry Chemical Physics*, 2007, **9**, 2959-2967.
21. A. W. Omta, M. F. Kropman, S. Woutersen and H. J. Bakker, *Science*, 2003, **301**, 347-349.
22. A. Chandra, *Phys. Rev. Lett.*, 2000, **85**, 768-771.
23. H. J. Bakker, *Chem. Rev.*, 2008, **108**, 1456-1473.
24. R. W. Gurney, *Ionic Processes in Solutions*, McGraw-Hill, New York, 1953.
25. M. D. Fayer and S. Park, *P. Natl. Acad. Sci. USA*, 2007, **104**, 16731-16738.
26. G. E. Walrafen, *J. Chem. Phys.*, 1962, **36**, 1035-&.
27. T. Ujike, Y. Tominaga and K. Mizoguchi, *J. Chem. Phys.*, 1999, **110**, 1558-1568.
28. Y. Wang and Y. Tominaga, *J Chem Phys*, 1994, **101**, 3453-3458.
29. S. R. Meech and I. A. Heisler, *Science*, 2010, **327**, 857-860.
30. G. E. Walrafen, M. S. Hokmabadi and Y. C. Chu, in *Hydeogen-Bonded Liquids*, eds. J. C. Dore and J. Teixeira, Kluwer Academic, 1991, pp. 261-283.
31. M. Starzak and M. Mathlouthi, *Food Chem.*, 2003, **82**, 3-22.
32. T. Iijima, *J. Mol. Struct.*, 1996, **376**, 525-529.
33. J. M. Heuft and E. J. Meijer, *J. Chem. Phys.*, 2003, **119**, 11788-11791.
34. J. M. Heuft and E. J. Meijer, *J. Chem. Phys.*, 2005, **123**.
35. G. Herzberg, *Molecular spectra and molecular structure II. Infrared and Raman spectra of polyatomic molecules*, D. Van Nostrand Company, Inc., Princeton, New Jersey, New York, 1962.
36. D. J. Tobias, K. M. Callahan, N. N. Casillas-Ituarte, M. Roeselova and H. C. Allen, *J. Phys. Chem. A*, 2010, **114**, 5141-5148.
37. J. Kapitan, M. Dracinsky, J. Kaminsky, L. Benda and P. Bour, *J. Phys. Chem. B*, 2010, **114**, 3574-3582.

Chapter 4

Water dynamics in aqueous solutions of amphiphilic and hydrophilic solutes

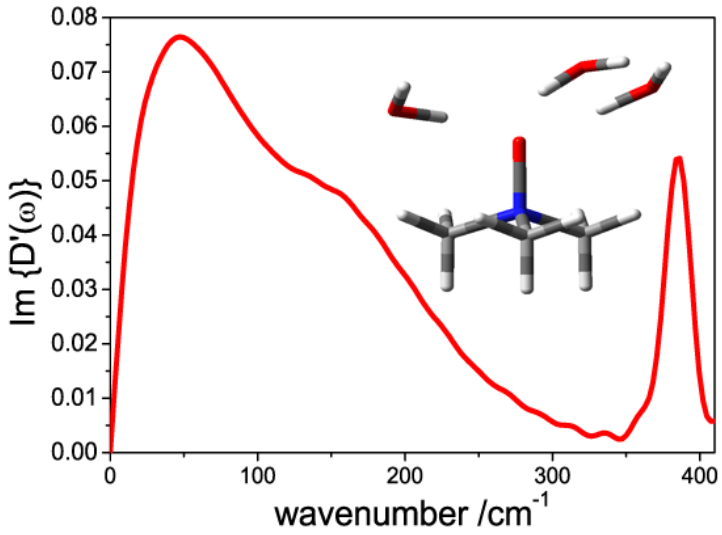

In this chapter the anisotropic OKE response of simple aqueous solutions is described. The observed picosecond relaxation dynamics are discussed in terms of hydrophilic and hydrophobic interactions at the interface between solute and water, *i.e.* in the solvation shell. At first, the dynamics of two largely hydrophilic solutes: urea ($CO(NH_2)_2$, UA) and formamide (CH_3NO, FA) will be compared with two amphiphilic solutes with large hydrophobic surface areas: tetramethylutrea ($(CH_3)_2NCON(CH_3)_2$,TMU) and trimethylamine N-oxide ($(CH_3)_3N(O)$, TMAO). Finally the temperature dependence of the OKE response of tert-butanol ($(CH_3)_3COH$, TBA) and TMAO will be compared and contrasted.

4.1. Introduction

Interfacial water is of great importance in biology. It is well known that such water has different properties to those of bulk water. Interfacial water is important in controlling the structure of biological assemblies, *i.e.* protein folding, function and reactivity in biological media. As a consequence it has been the subject of intensive studies in recent years.[1-12] Particular attention has been paid to water dynamics in the vicinity of hydrophilic and hydrophobic sites.[1-3, 9, 10, 13-15] In general biological water exhibits slower dynamics than bulk water. Despite these extensive studies no uniform picture of the magnitude or mechanism of the slow down of hydration water dynamics has emerged, *i.e.* it is not clear how many solvation shells are affected by the solute,[16] or what is the water structure in the vicinity of hydrophobic sites.[9, 13, 15]

In order to provide a new perspective on this problem we studied a range of prototypical hydrophilic and hydrophobic solute molecules: TMAO, TMU, UA, FA and TBA, (Figure 4.1). TMAO consists of three hydrophobic methyl groups and a hydrophilic group consisting of a very polar N^+O^- group. Its oxygen having three

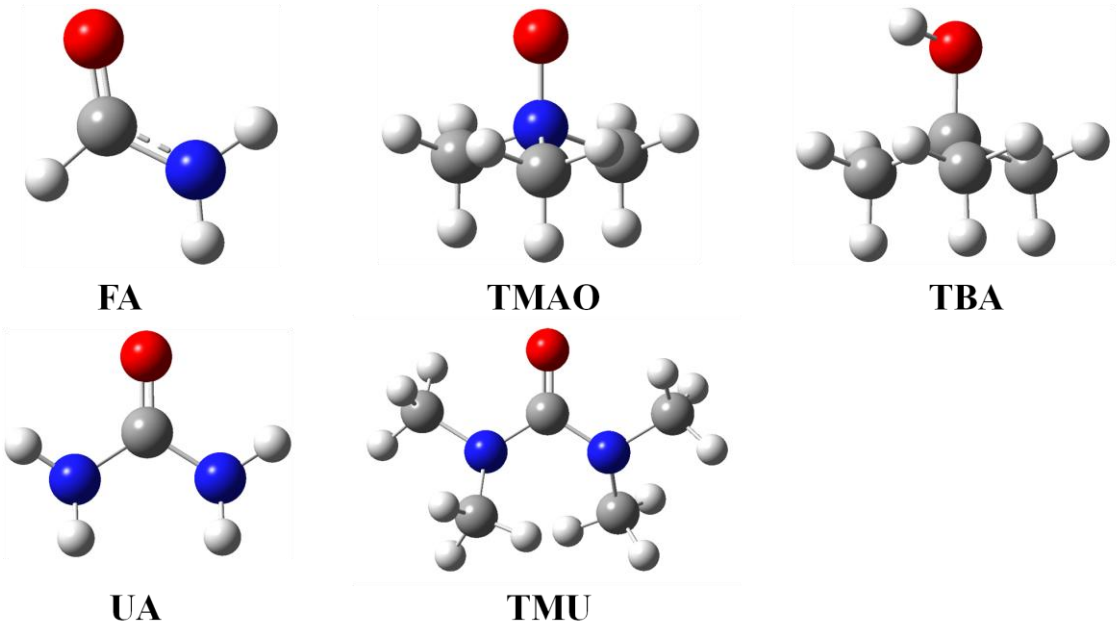

Figure 4.1 Optimized structures of FA, TMAO, TBA, FA and TMU obtained from DFT calculations.

lone pairs can accept more than two hydrogen bonds.[17] TBA has a hydrophobic part identical to that of TMAO, but its hydrophilic group consists of one hydroxyl group. TMU consists of four methyl groups and a hydrophilic carbonyl group. Oxygen from this group can form on average two hydrogen bonds with surrounding water molecules.[18] Computer simulations showed that the strength of the interaction between the TMU nitrogen atom and water is not sufficient to stabilize hydrogen bonded complex, thus it was concluded that nitrogen atoms in TMU cannot form hydrogen bonds in aqueous solutions.[18] Thus, the hydrophilic group of TMAO and TMU can only act as hydrogen bond acceptors. TBA can however act also as a hydrogen bond donor. To compare with these mainly hydrophobic molecules, UA and FA were chosen as representatives of mainly hydrophilic molecules. UA and FA have two and one amine group, respectively, connected by a carbonyl. Thus, both UA and

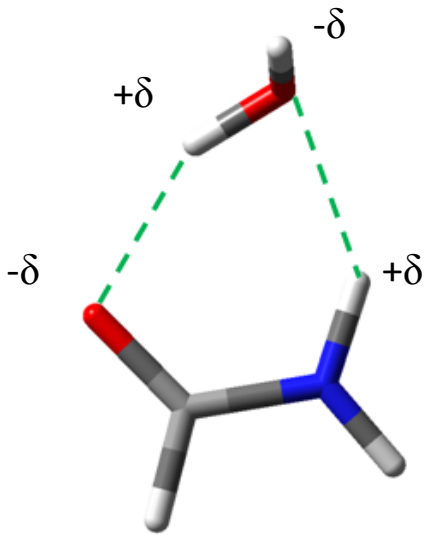

Figure 4.2 Representation of H-bonding ability of FA. δ is a partial charge, and +δ denotes donor and –δ is acceptor.

FA (Figure 4.2), act as a hydrogen bond acceptor and donor, with urea and formamide able to form six and four hydrogen bonds in an aqueous solution, respectively.[19, 20]

The values of the B coefficient in viscosity studies,[21] indicate the structure making or breaking ability of a given solute (section 3.1). However within this classification there is some ambiguity, especially concerning the microscopic behaviour of the solutions investigated. The values of B-coefficients obtained for UA, FA, TBA and TMU are 0.035, 0.019, 0.373 and 0.384, respectively.[22] This indicates that these solutes act as structure makers. On the contrary TMU was classified as a structure breaker on the basis of molecular dynamics simulations.[23] Neutron scattering data[24] on the other hand supports the assignment to a structure making capability for TMU. TMAO, on the basis of molecular dynamics simulations, was classified as a structure maker.[23] Urea, similarly to TMU, does not have a clear assignment. Using Raman and ultrasonic attenuation measurements[25, 26] it was concluded that UA is a structure breaker. On the other hand dielectric measurements[27] suggested that UA is not a

strong structure breaker and molecular dynamics simulations suggested that UA is in fact a structure maker.[28, 29] NMR studies of UA solutions performed by two different groups have previously reported UA as either a structure breaker,[30] or suggested it has little or no effect on water structure.[31] Positron annihilation and sound velocity studies classified FA as a structure breaker.[32] Therefore, on the basis of these findings it is impossible to infer structure making/braking ability of the solute from B-coefficient value.

The microscopic solvation structure of UA has been most intensively studied by spectroscopic techniques including IR, neutron and Raman scattering[2, 19, 33] and molecular dynamics simulations.[17, 23] No consistent picture of water properties in the presence of UA has emerged.[29, 34, 35] Idrissi *et al.*[34] on the basis of molecular dynamics simulations found enhanced water structure and that there is a distortion of the tetrahedral water structure upon addition of UA (both radial and orientational). They found that the increase of the fluctuation in the radial distance and the loss of mutual orientation of the nearest water forming the tetrahedron cause weakening of the tetrahedral arrangement of water molecules. However, molecular dynamics simulations by Kuffel *et al.*[17] showed quite opposite behaviour. In their simulations, the geometry of the water-water hydrogen bond network around UA was the same as that in bulk water. NMR studies of UA solutions found that the orientational relaxation of water molecules was largely unaffected by UA.[36] The possibility of self-association of UA molecules with increasing concentration in aqueous solution has also been considered. Infrared studies suggested the possibility of formation of UA dimers, which slightly alter the structure of water,[2] while Monte Carlo simulations suggested that UA dimers are present at ~1 M concentration, and that above ~5.5 M a UA network is formed.[7] However, at concentrations below 1 M UA does not affect

the water structure.[7] In contrast to these reports a neutron scattering study found no evidence for the existence of UA dimers.[19] Clearly there is still room for further experimental study of aqueous UA solution.

4.2 Hydrophilic and Hydrophobic Interactions

In 1945 Frank and Evans[37] reported that the entropy of vaporization of non-polar solutes in water diverged from that established for nonaqueous solutions. They suggested that water molecules form frozen patches or icebergs around non-polar solutes, which are dependent on the solute size. In such a clathrate-like structure water molecules in the first hydration shell of a nonpolar solute do not create H-bonds with the solute, instead they form a hydrogen bonded cage around the solute. This model however was challenged as no evidence of ice-like water structures was found in neutron scattering measurements[38] and simulations.[39] It has been suggested that the loss of entropy can also be explained without invoking frozen water.[40] However the iceberg model has recently had some support by means of the molecular dynamics simulations of Wei *et al.*[23] They reported that on average individual bonds between water molecules become stronger in the presence of TMU and TMAO molecules. Further they showed that the presence of TMAO led to increased ordering of the water molecules, making them "ice-like"; however no such ordering was observed in aqueous solution of TMU.[23] Recently a dynamical, rather than structural picture of the iceberg model was proposed by Bakker *et al.*[9, 10] on the basis of ultrafast time resolved mid-infrared spectroscopy. They found much slower orientational dynamics of water in the presence of hydrophobic groups than was observed for bulk water. From this they concluded that each methyl group of TMU and TMAO immobilizes on average four water OH groups. However their dynamical picture is in contrast to conclusions

of dielectric relaxation[41] and NMR spectroscopy.[42, 43] These studies together with molecular dynamics simulations[15, 44, 45] did not produce evidence for a dynamic iceberg model. In particular a large number of molecular dynamics simulations were reported by the group of Laage.[13, 15, 46, 47] They used molecular dynamics simulations and an analytic extended jump model of water orientational dynamics (see section 2.4.3) to study TMAO,TBA and TMU, and found only a moderate slow down of solvent orientational dynamics at low solute concentration in the vicinity of hydrophobic groups (less than a factor of two compared to bulk water). This slow down of water reorientation was explained on the basis of slower H-bond exchange and an excluded volume effect (*i.e.* the approach of a new H-bond acceptor is limited by the presence of the hydrophobic group). No evidence however was found for water immobilization in these calculations.

Hydrophilic interactions received the same amount of interest as hydrophobic ones. In this case again no consensus has been reached regarding the extent of these interactions on water dynamics.[15, 48] Hydrophilic groups interact strongly with water through H-bonds and Coulombic interactions. However Pshenichnikov *et al.*[48] using 2D IR spectroscopy found that the effect of the hydrophilic groups exerted on water dynamics is negligible in comparison with hydrophobic groups. In contrast Laage *et al.*[15] found that hydrophobic groups do not affect the water dynamics as much as hydrophilic sites. Using molecular dynamics simulations they calculated that water dynamics around hydrophilic sites are 2.5 times slower than around hydrophobic ones.

4.3 Two State Model for Diluted Solutions

The advantage of OKE is that both structural (spectral density) and picosecond dynamics are recovered. The complex origin of the picosecond dynamics was discussed in chapter 2. A problem is that the OHD-OKE technique probes the collective polarizability of the entire system and does not allow the separate measurement of the hydration water and free water. Therefore it is instead assumed that the average time, $<\tau>$, measured is a sum of the free water relaxation, τ_{WF}, and hydration water relaxation, τ_{WH}, weighted by their molar fraction, X_i:[49]

$$<\tau>= X_{WF}\tau_{WF} + X_{WH}\tau_{WH} \tag{4.1}$$

After substituting $X_{WF}+X_{WH}$ =1, the above equation can be rewritten for diluted solutions:

$$<\tau>= n_{SW}n_m(\tau_{WH} - \tau_{WF}) + \tau_{WF} \tag{4.2}$$

where n_{SW} is the molar ratio (moles of solute divided by moles of water) and n_m is the number of water molecules in the hydration shell. The n_m was chosen to include the number of water molecules in the first hydration shell, unless otherwise stated. The above equation is only valid for diluted solutions. If we perform a linear fit to the data (relaxation time vs. molar ratio), the slopes obtained are $n_m(\tau_{WH} - \tau_{WF})$. To calculate n_m, firstly, the molecular volumes of the solute and water molecules were obtained from DFT calculations. Knowing the volume of each molecule, the number of water molecules in the first hydration shell was calculated from simple geometric properties.

It was taken as a number of adjacent spheres representing water on the surface of a sphere representing a solute molecule, Figure 4.3.The volume of a solute molecule

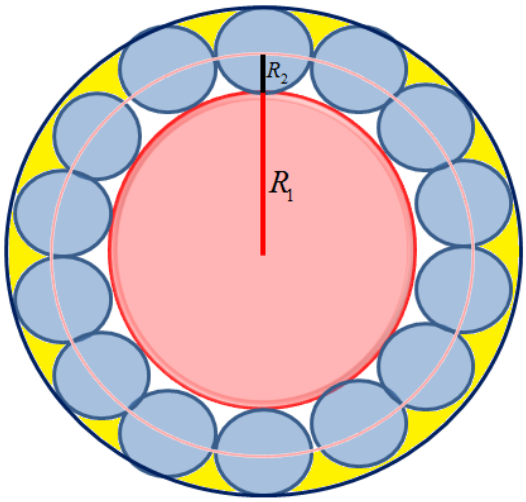

Figure 4.3 Cross-section of a solute (red) surrounding by solvent molecules (blue).

with half the volume of the water layer around the solute was calculated:

$$V_3 = 4(R_1 + R_2)^3 \pi / 3 \tag{4.3}$$

where R_1 and R_2 are radii of solute and water, respectively. Half of the water layer was taken in order to minimize free volume of spaces between spheres (yellow in Figure 4.3). Then the number of water molecules was calculated as follows:

$$n_m = \frac{(V_3 - V_1)}{V_2} \cdot 2 \cdot 0.87 \tag{4.4}$$

where V_1 and V_2 are the volume of solute and water respectively. The highest density that can be achieved by the arranging of spheres is given by the Kepler conjecture[50] and is equal to 0.74048. This indicates that the volume occupied by void is 26 % of the total volume. However, in the calculation of the volume occupied by water molecules only the white spaces between spheres were included. Therefore, the volume occupied by void should be half of the 26 % given by Kepler's conjecture. Therefore water molecules occupied 87 % of the V_3 –V_1 volume, thus multiplication by 0.87 in the above equation. Multiplication by a factor two includes the second half

of the water layer. Calculated numbers of water molecules in the first hydration shell using this simple geometric model agreed very well with data found in literature,[14] *i.e.* n_m for UA and TMU calculated with the described method are 21(UA) and 32 (TMU) while 20 and 32 were obtained through molecular dynamics simulations.[14]

4.4 Concentration Studies of Aqueous Solutions

Here the time and frequency domain data of four aqueous solutions of UA, FA, TMAO and TMU at room temperature will be analysed and discussed.

4.4.1 Picosecond Time Domain Analysis

OKE traces for four of the solutions studied are plotted as a function of concentration in Figure 4.4. Data were normalized to the electronic response at t = 0 ps. Hydrophilic FA and UA solutions exhibit qualitatively similar dynamics, with the relaxation time increasing with solute concentration. TMU follows a similar pattern, but the increase associated with the slowest components is much more marked. The slowest relaxation time in TMU solutions was not observed for neat TMU but for a concentration of 4 M, Figure 4.4f. This is likely to be associated with the viscosity of the solution which has its maximum around 4 M, see below. In contrast the relaxation time of TMAO solutions increases with increasing concentration but less dramatically and without a major increase in amplitude. At the high concentration new underdamped (oscillatory) features appear in the subpicosecond response for UA, FA, TMAO and TMU. These features can be seen at around 500 fs for FA and UA solutions and between 200 fs and 1.7 ps for TMU and TMAO solutions. These oscillations are assigned to Raman active solute modes and will be explained in detail below.

The picosecond OKE relaxation dynamics of UA, FA and TMAO solutions were fit with a biexponential function given (Eq. 2.34). The fitting parameters are listed in Table 4.1. Two exponentials were not sufficient to reproduce the picosecond response of TMU and a third exponential was added. The rise time was fixed at 10 fs. As the

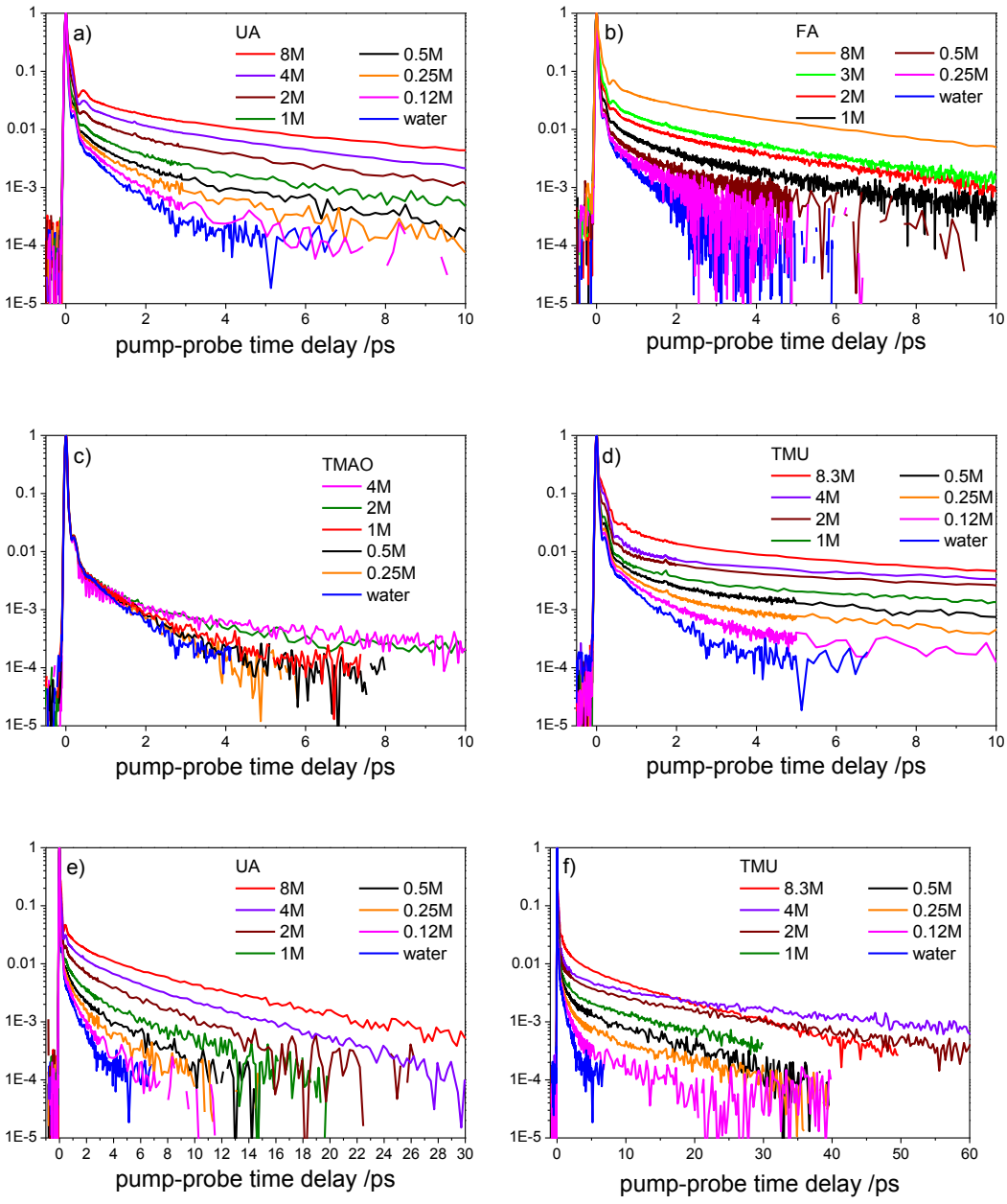

Figure 4.4 Time resolved OKE signals of aqueous UA,FA,TMAO, and TMU plotted against concentration a),b),c) and d) at the short time scale. e) and f) long time scales observed for urea and TMU. Pure water is shown in blue.

subpicosecond OKE data reflects the non-diffusive and interaction induced contributions it is convenient to analyse them in the frequency domain. Therefore data before 1 ps were not included in the fit. Data obtained from the biexponential fit were used to calculate a weighted mean relaxation time, $<\tau>$, Eq. 2.35. Calculated values

Concentration /mol	$\frac{a_1}{a_1+a_2+a_3}$	**τ_1 /ps**	$\frac{a_2}{a_1+a_2+a_3}$	**τ_2 /ps**	$\frac{a_3}{a_1+a_2+a_3}$	**τ_3 /ps**
water	0.81	0.46	0.19	1.55		
Urea						
0.06	0.86	0.50	0.14	1.98		
0.12	0.82	0.51	0.18	2.03		
0.25	0.84	0.54	0.16	2.89		
0.5	0.80	0.81	0.20	4.10		
1	0.75	0.94	0.25	5.05		
2	0.66	1.17	0.34	5.50		
4	0.62	1.33	0.38	6.36		
8	0.62	1.71	0.38	8.81		
Formamide						
0.06	0.84	0.50	0.16	2.03		
0.12	0.84	0.54	0.16	2.08		
0.25	0.83	0.60	0.17	2.60		
0.5	0.79	0.70	0.21	3.90		
1	0.77	0.95	0.23	5.00		
2	0.71	1.28	0.29	5.58		
3	0.70	1.40	0.30	5.70		
6	0.60	1.38	0.40	5.81		
8	0.57	1.40	0.43	5.87		
25	0.58	1.48	0.42	14.11		
TMAO						
0.25	0.85	0.71	0.15	1.95		
0.5	0.84	0.80	0.16	2.31		
1	0.81	0.90	0.19	3.03		
2	0.75	1.10	0.25	5.44		
4	0.83	1.44	0.17	8.20		
TMU						
0.06	0.82	0.49	0.14	1.70	0.04	3.16
0.12	0.81	0.59	0.11	1.74	0.08	7.21
0.25	0.69	0.62	0.19	1.99	0.12	12.25
0.5	0.61	0.85	0.17	2.30	0.22	12.65
1	0.59	1.19	0.11	3.10	0.30	15.55
2	0.46	1.38	0.27	5.56	0.27	29.27
4	0.45	1.30	0.32	6.64	0.23	46.90
6	0.50	1.70	0.28	7.20	0.22	47.90
8.3	0.70	1.06	0.13	7.66	0.17	15.74

Table 4.1 Fitting parameters to biexponential function given by Eq. 2.34.

are plotted as a function of molar ratio, n_{SW} (moles of solute to moles of water) in Figure 4.5. The weighted mean relaxation time obtained for TMU was calculated using the fastest two components only. The third, long component required to fit the response is discussed separately. Two different concentration regions are evident from Figure 4.5a. One below n_{SW} =0.05 where the relaxation time increases significantly with concentration and above this concentration, where the slow down is much less pronounced. These two regions are discussed separately.

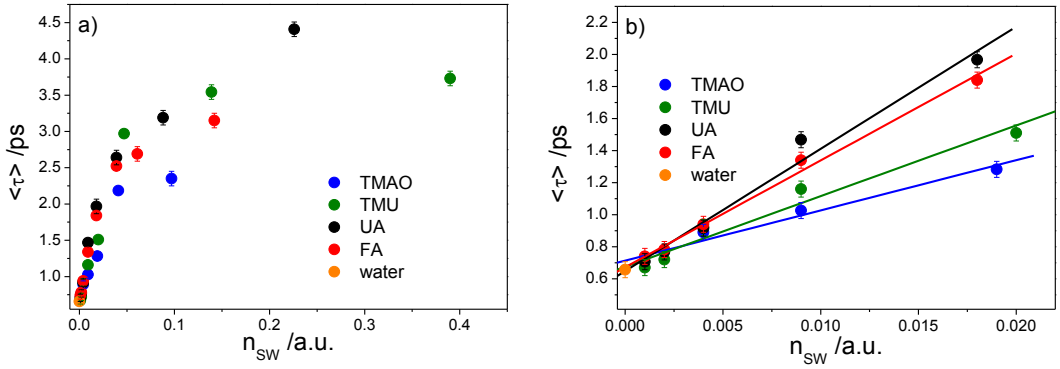

Figure 4.5 a) Weighted mean lifetime for UA, FA, TMAO and TMU solutions plotted as a function of molar ratio, b) linear fit to the data for the solutions of molar ratio below 0.02.

4.4.1.1 Low Concentration Region

At low concentration, below $n_{SW} \approx 0.02$, the weighted mean lifetime increases linearly with increasing solute concentration and extrapolates back to the pure water value (Figure 4.5b). Therefore we assume that at this low concentration the observed relaxation time is dominated by the dynamics of the water H-bonded network. Qualitatively it is apparent that in the low concentration range hydrophilic UA and FA give rise to a larger increase in $<\tau>$ than the hydrophobic solutes TMAO and TMU.

We investigated the extent to which the solute might contribute to the weighted mean relaxation time at these low concentrations since its contribution cannot be separated from the sample response. Firstly, it was assumed that the relaxation time associated with the solute corresponds to the longest relaxation time observed at the highest concentration and that this is the solute orientational relaxation. From this assumed solute relaxation time and knowing the relaxation time of pure water and the respective mole fractions, a value for $<\tau>$ was calculated under the assumption that it is simply a weighted sum of the bulk water and the solute relaxation times (the latter were corrected for the viscosity of the solution, Eq. 4.6):

$$<\tau_x>= X_w\tau_w + X_s\tau_s \tag{4.5}$$

$$\tau_s = \tau_\infty / \left(\frac{\eta_\infty}{\eta_x}\right) \tag{4.6}$$

where X_w and X_s are the molar fractions of bulk water and solute, respectively. τ_w and τ_s are the relaxation times of water and the reorientational time of the solute, respectively and τ_∞ is the relaxation time observed for the highest concentration, η_∞ is the viscosity at the highest concentration, and η_x is the viscosity at the concentration studied. The origin of the Eq. 4.6 lies in the DSE theory, section 2.4.1. Values obtained from the Eq. 4.5 are plotted in Figure 4.6. The solute relaxation times under these conditions are substantially shorter than those obtained experimentally, therefore suggesting that an additional contribution must have been observed in the measurement. We assume this contribution is the slow relaxation of hydration shell water. This assessment points to the minor solute contribution at low concentrations, which is consistent with the results of MD simulations for FA in water, which found the water response begins to dominate at $X_S < 0.05$.[51]

To model quantitatively the effect of solute on the water dynamics in its vicinity it is necessary to consider to what extent water molecules are affected by a single solute molecule. As a first approximation, the number of water molecules in the first

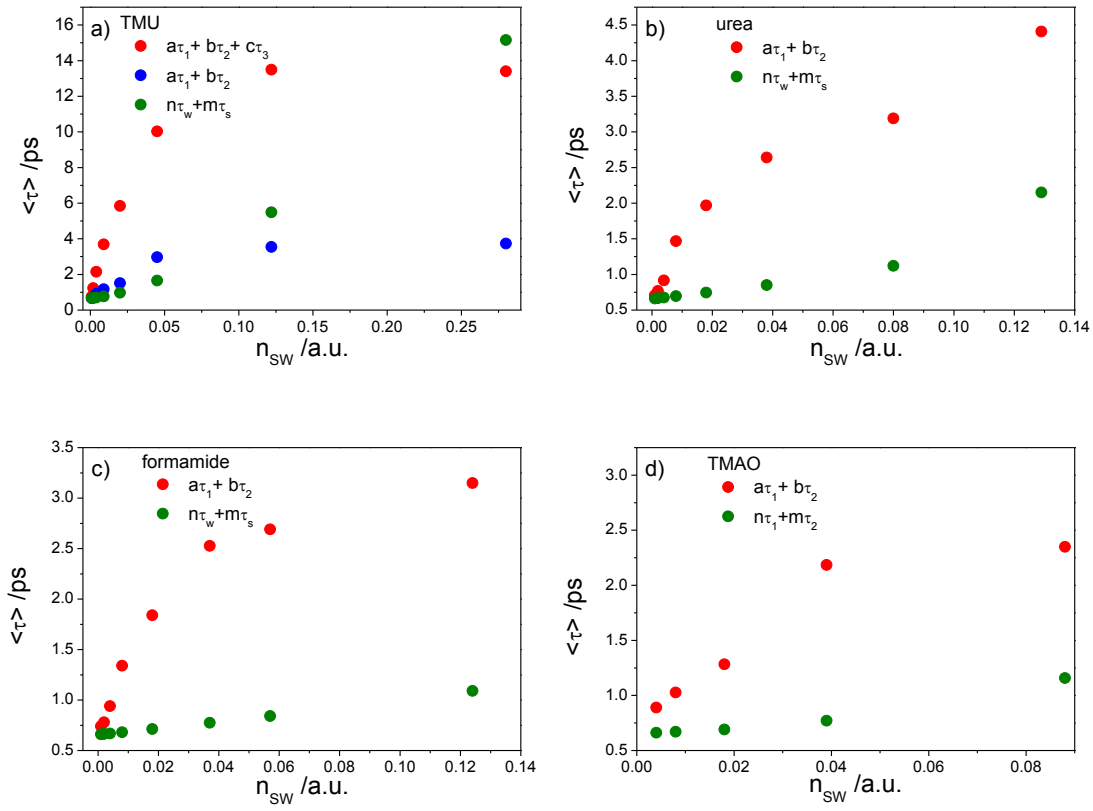

Figure 4.6 Comparison of the weighted mean lifetime (red dots) with time calculated from Equation 4.5 (green dots) for four molecules studied. The blue dots in the TMU data a) denote the weighted mean relaxation time calculated from Eq.2.35 for the two fastest exponentials. Error 5 %

solvation shell of each solute, n_m was calculated using the procedure described in section 4.4. The molar volumes obtained from the DFT calculations (Gaussian03, B3LYP hybrid functional and the 6-31G (d,p) basis set) were 45.62 cm^3/mol, 30.54 cm^3/mol, 108.08 cm^3/mol and 82.61 cm^3/mol for UA, FA, TMU and TMAO, respectively. The molecular volumes were calculated from those molar volumes by

dividing molar volumes by Avogadro's number. Values obtained are 75.76 $Å^3$ (UA), 50.72 $Å^3$ (FA), 179.47 $Å^3$ (TMU) and 137.18 $Å^3$ (TMAO). The volume of a water molecule was calculated to be 22 $Å^3$. From Eq. 3.5 the number of water molecules in the first solvation shell (n_m) was 21, 17, 32, 28 for UA, FA, TMU, TMAO, respectively. These values are in good agreement with previously published data,[14] where hydration numbers were obtained through molecular dynamics simulations.

The slope of linear fits to Eq. 4.2 yields $n_m(\tau_{WS} - \tau_{WF})$. Using the calculated n_m the relaxation times, τ_{WS}, were calculated to be: 1.7 ps for TMAO, 1.9 ps for TMU, 4.2 ps for UA, 4.4 ps for FA (all ±0.2). Thus, water relaxation in the first hydration shell is 2-3 times slower than in bulk water ($\tau_{WF} = 0.67 \pm 0.1$) for the hydrophobic TMAO and TMU solutes and 6-7 times slower for hydrophilic UA and FA. The retardation factor is somewhat dependent on the assumptions made in the analysis. For example it was assumed that only the first solvation shell of solute molecules is affected.

If the solute influences the water dynamics beyond the first hydration shell (n_m equal to the sum of water molecules in the first and second hydration shell) the ratio is smaller and the relaxation time are 1.3 ps (TMAO), 1.4 ps (TMU), 2.4 ps (UA) and 2.6 ps (FA) (all ±0.2). Such long range effects have been suggested in some molecular dynamics studies of proteins[16] and aqueous carbohydrate solutions.[52]

Figure 4.5 confirms that the degree of slow down depends on the nature of the solute; the slowest water dynamics were observed for hydrophilic solutes, UA and FA. This is in agreement with molecular dynamics simulation by Laage *et al.*[15] and neutron scattering experiment by Russo *et al.*[6] The modest effects of hydrophobic solutes on water dynamics are also consistent with NMR measurements[14] and a very recent study of dielectric relaxation in dilute aqueous TMU.[53] This is significant as NMR and

dielectric relaxation probe rather different dynamics (rotational) to those reported by OHD-OKE (translational), as discussed in chapter 2.

4.4.1.2 High Concentration Region

At n_{SW} > 0.02 (i.e. >1 M solute concentration), the weighted mean relaxation time increases less slowly with increasing solute concentration, and no longer extrapolates to the pure water result. At this concentration it is likely that the solute orientational relaxation time contributes to the observed OHD-OKE signal. In addition solute – solute interactions are likely to become significant.

At these high concentrations almost all water molecules are in the first hydration shell of a solute (Figure 4.7). Therefore the relation given by Eq. 4.2 is no longer valid as it is only applicable for dilute solutions. As a consequence of almost all water molecules being involved in hydration shells or being shared between solute hydration shells, their ability to form the tetrahedral structures characteristic of bulk water may be limited. This effect is analysed in detail in the frequency domain representation, section 4.4.2. Above 0.5 M, significant changes in amplitude of the slow component are observed, however these changes are not accompanied by a large increase in relaxation time; *i.e.*, the change in τ_2 between 1 and 8 M for FA is only a factor of 0.87, which is reflected in the concentration dependent $<\tau>$, where relatively small increases are observed for concentrations above 1 M, Figure 4.5. This suggests a growing contribution from slow structural relaxation in these more concentrated solutions.

Slow orientational dynamics were reported by Rezus *et al.*[10] in their mid-infrared ultrafast pump-probe studies of vibrational and orientational relaxation of HDO

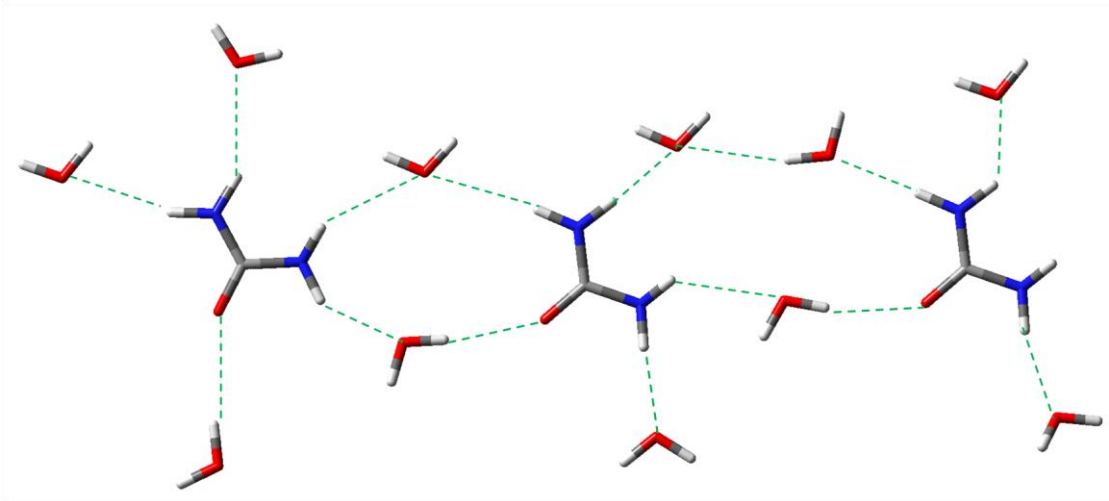

Figure 4.7 Hydration water being shared between two UA solutes. Green dashed lines denote hydrogen bonds.

molecules (water molecule with one proton and one deuterium) in relatively concentrated (>0.4 M) aqueous solutions of TMU. Reorientation times more than four times slower than bulk water were observed, which was assigned to approximately 15 OH groups being immobilized by the TMU methyl groups. This slowing down effect of a hydrophobic solute on the aqueous solvent is clearly larger than that seen in the OHD-OKE experiments (Figure 4.5), although different dynamics are probed by the two methods and the solute may contribute to OHD-OKE, especially for TMU. Molecular dynamics simulations by Laage e*t al.*[15] showed that water molecules reorient about 1.5 and 4 times slower than bulk water in the vicinity of hydrophobic and hydrophilic groups, respectively. They suggested that the retardation of water dynamics originates from a combination of two effects. Firstly, the oxygen in TMAO forms stronger H-bonds with water molecules than are formed between water molecules. This process is concentration independent. Secondly, the slowing down of water dynamics is due to the solute-induced transition state excluded volume fraction effect. The presence of the hydrophobic moieties prevents the approach of water

molecules, thus retarding the jump rate between water molecules around a hydrophilic group. This process is concentration dependent. These are qualitatively consistent with the OHD-OKE data reported above (although again OHD-OKE measures structural (translational) relaxation in the water network rather than orientational relaxation). Interestingly Laage and co-workers suggested that the effect of concentration on reorientation might be larger than calculated because of the concentration dependent viscosity of the solutions.[13]

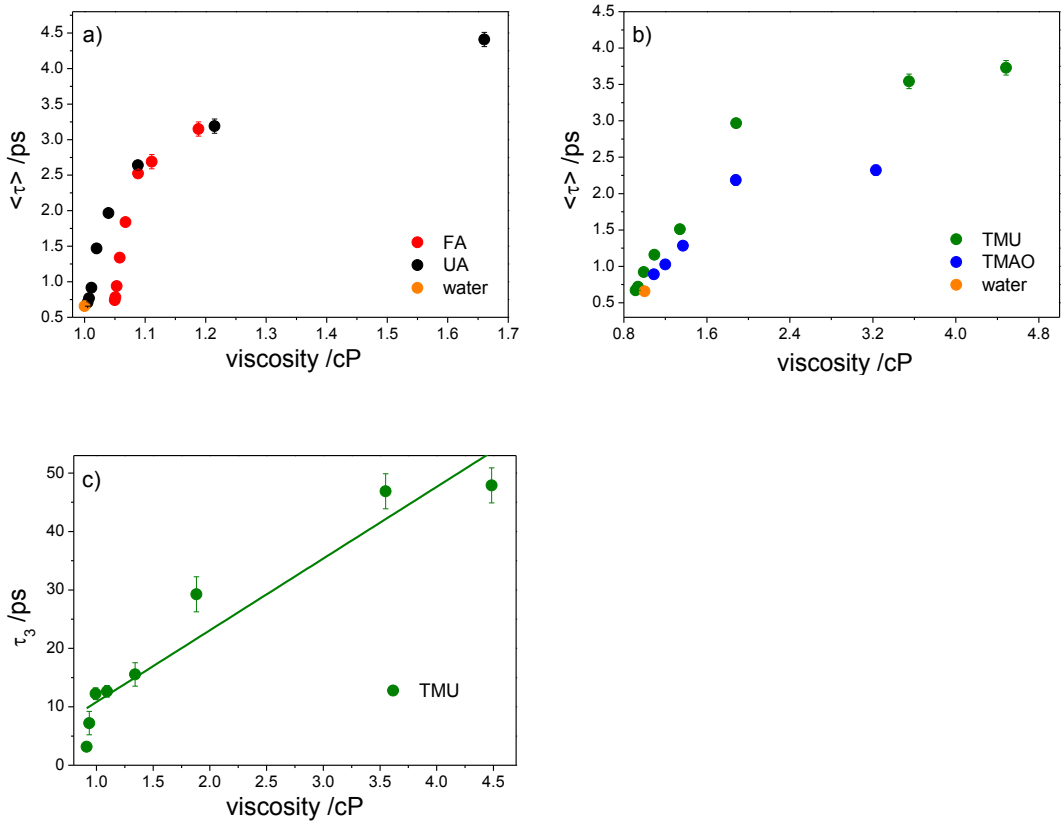

Figure 4.8 Dependence of the weighted mean relaxation time, <τ>, on viscosity for a) UA and FA, b) TMAO and TMU. The slowest relaxation time recovered for TMU is plotted as a function of viscosity.

In Figure 4.8 the relationship between the measured relaxation time <τ> and solution viscosity is plotted. The changes in viscosity for FA and UA are very small, at most 65% over the full concentration range, while the increase in <τ> is large (a factor of 7

for UA), Figure 4.8a. The increases in $<\tau>$ observed for TMU and TMAO are of a similar order to those for FA and UA, but the viscosity change is much larger (increasing by up to a factor of 5) over the same concentration range, Figure 4.8b.From these data it is clear that viscosity has at most a minor effect on the relaxation time observed in OHD-OKE.

The time domain data for TMU solutions were the only ones for which three exponential functions were required to fit the picosecond dynamics. The relaxation time, τ_3, obtained from the third exponential is plotted in Figure 4.8c and was fitted with linear function. The results is fairly consistent with the Debye-Stokes-Einstein (DSE) relation (Eq. 2.30). This suggests the assignment of τ_3 to orientational relaxation of TMU. However the saturation in the relaxation time observed for the two highest viscosities might reflect clustering of TMU molecules. The viscosity of TMAO is similar to that of TMU. However the signal for TMAO at high concentration was several times smaller and it was not possible to resolve a third exponential. This implies that the TMAO solute contributes at most a minor component to the picosecond relaxation dynamics, which thus reflect dynamics in the solvating water molecules, consistent with the preceding analysis. Even though TMAO has a large dipole moment it is also symmetric molecule, therefore its reorientational contribution are negligible.

4.4.2 Frequency Domain Analysis

The concentration dependent Im $D'(\omega)$ of UA, TMU, FA and TMAO solutions are shown in Figure 4.9. All data were normalized in the time domain to the electronic response prior to the Fourier transform. The Im $D'(\omega)$ measured for solute concentrations between 0 and 0.5 M are very similar to one another. At these low

concentrations they retain the bimodal shape characteristic of liquid water, chapter 2. Thus we conclude that the structure of liquid water is maintained at these low solute concentrations, even though the collective picosecond time scale relaxation dynamics are slowed appreciably by the presence of the solute, as described in section 4.4.1. For the low concentrated samples, the intensity of Im *D'(ω)* increases slightly with increasing concentration suggesting change in the H-bonded network.

Above 0.5 M there is a considerable divergence in the shape of the spectral densities for the different solutes. For TMAO the Im *D'*(*ω*) are remarkably independent of solute concentration apart from the appearance of a mode at ~380 cm^{-1} assigned to an

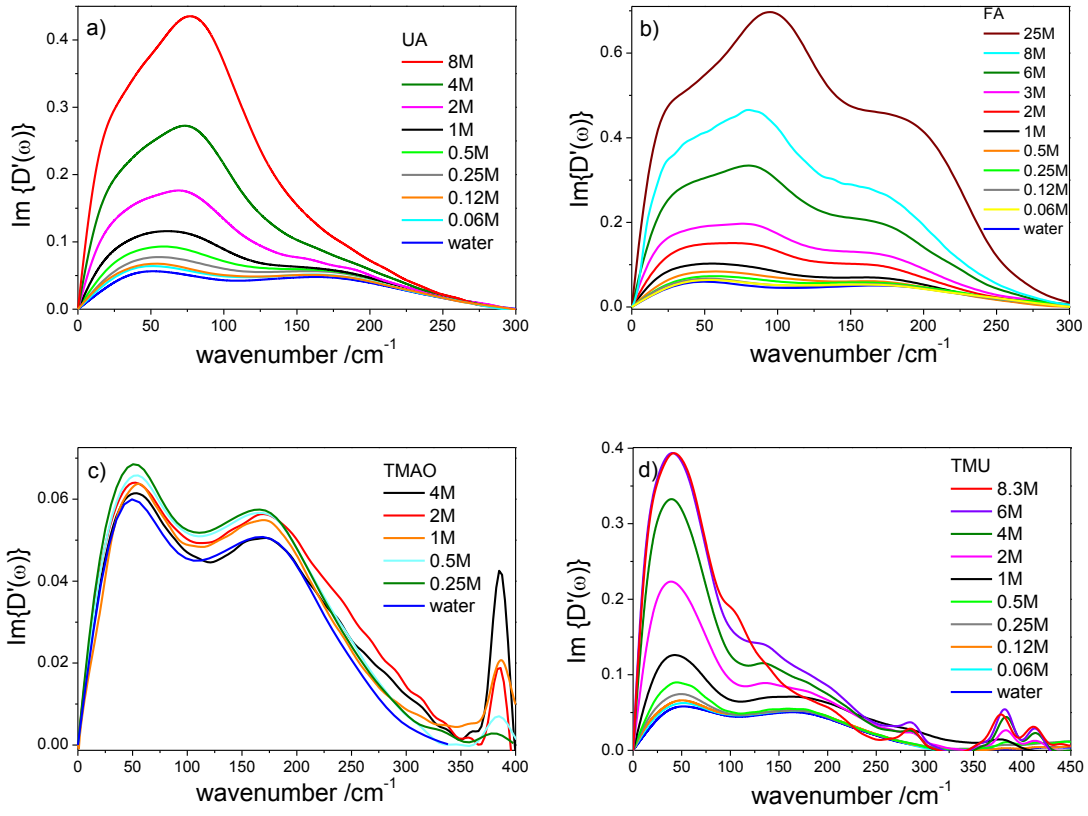

Figure 4.9 Raman spectral densities for aqueous solutions of UA, FA, TMAO and TMU as a function of concentration. 25M and 8.3M are the concentrations of neat FA and TMU respectively. The Im D'(ω) of pure water is plotted in blue.

intramolecular Raman active vibration (Figure 4.9c). This mode increases in amplitude linearly with increasing solute concentration, as expected for an intramolecular mode. For UA and FA the increased amplitude in Im $D'(\omega)$ with increasing concentration above 0.5 M is accompanied by the growth of a band around 100 cm^{-1} which is absent in pure water. For TMU above 0.5 M the amplitude also increases sharply and is dominated by strong growth in the band at low frequency, which is also evident in neat liquid TMU.

To quantitatively analyse all spectral densities, they were fitted to functions given by Eq. 2.37-2.39. Numerical values obtained from this fitting procedure, which gave good quality fits (Figure 4.10) for these four solutes, are listed in Table 4.2. At the low concentration region, below 0.5M, only two functions (BL and ASG) were needed to recover spectral densities of UA and FA. The same two functions were used to fit the pure water Im $D'(\omega)$. A third function (G) was added to fit the data above 0.5 M. The water spectrum was not subtracted from the solution spectra prior to fitting as solute-water modes can contribute to the observed spectra.

The Im $D'(\omega)$ of TMU is much more complex and two additional to water G functions were required to fit the low frequency part of the spectrum (Figure 4.10b). The Raman spectrum of TMU was also investigated through DFT. A number of low frequency modes were found. The two additional modes in the TMU spectral density < 300 cm^{-1} (52 and 107 cm^{-1} for pure TMU), are most likely to be associated with modes at 77 cm^{-1} and 101 cm^{-1} obtained from DFT calculations, Figure 4.9d. However the lowest frequency band observed (52 cm^{-1}) might also be assigned to TMU librations. Such low frequency solute librations were previously observed in a number of studies.[54-56] The three higher frequency bands in the TMU spectral density

(Figure 4.9d) at 285, 378 and 412 cm^{-1} can be assigned to intramolecular modes obtained with DFT at 301 cm^{-1}, 368 cm^{-1} and 404 cm^{-1} (Figure 4.11a), respectively. Thus, we tentatively assign the additional component in the Im $D'(\omega)$ of TMU to molecular modes of the solute. The DFT spectra of the TMU upon salvation showed a shift of the TMU modes to the higher frequency.

The DFT calculations for TMAO did not show a broad distribution of low frequency modes (Figure 4.11a), consistent with experimental results (Figure 4.9c), where only

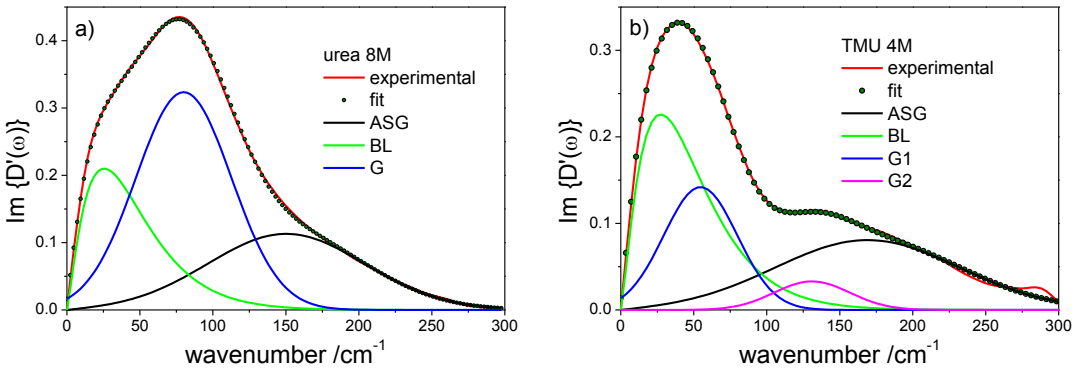

Figure 4.10 Fit to spectral densities of a) 8M UA and b) 4M TMU. BL, G and ASG denote Bucaro-Litovitz, Gaussian and antisymmetrized Gaussian, respectively.

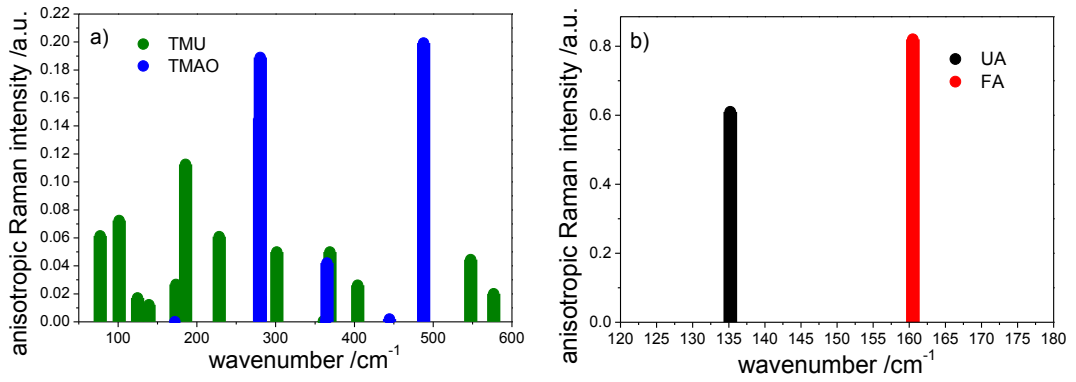

Figure 4.11 Frequencies obtained from the DFT calculations for single molecule of a) TMAO, TMU and b) UA and FA using DFT calculations.

Concent. /mol	A_{BL}	α	ω_{BL} /cm^{-1}	A_G	ω_G /cm^{-1}	$\Delta\omega_G$ /cm^{-1}	A_{ASG}	ω_{ASG} /cm^{-1}	$\Delta\omega_{ASG}$ /cm^{-1}
FA									
0.06	0.05	1.54	30.54	-	-	-	0.04	174.3	132.6
0.12	0.06	1.43	31.59	-	-	-	0.04	175.0	127.9
0.25	0.06	1.41	33.96	-	-	-	0.04	175.0	132.6
0.5	0.07	1.32	35.54	0.01	76.1	92.3	0.04	175.8	111.9
1	0.07	1.36	25.00	0.04	77.0	81.5	0.06	169.6	117.0
2	0.12	1.32	27.20	0.05	81.5	65.6	0.08	163.0	121.2
3	0.14	1.29	23.32	0.10	82.0	70.0	0.11	164.0	117.9
6	0.24	1.20	27.72	0.16	84.62	66.8	0.18	164.8	116.1
8	0.33	1.29	25.34	0.25	86.43	65.9	0.25	164.8	110.8
25	0.42	1.21	25.53	0.53	96.03	76.6	0.43	183.8	99.7
UA									
0.06	0.06	1.74	26.45	-	-	-	0.04	171.6	123.6
0.12	0.06	1.50	32.35	-	-	-	0.04	175.0	110.0
0.25	0.07	1.52	33.00	-	-	-	0.04	179.4	118.1
0.5	0.06	1.27	36.10	0.02	63.77	78.3	0.04	173.2	126.9
1	0.08	1.18	31.44	0.04	74.64	66.5	0.05	167.9	129.0
2	0.10	1.35	20.98	0.10	75.15	72.2	0.06	159.1	131.1
4	0.14	1.21	23.10	0.18	77.19	74.6	0.08	157.5	125.6
8	0.21	1.28	19.87	0.32	80.00	77.1	0.11	150.0	126.7
TMAO									
0.25	0.06	1.80	25.0	-	-	-	0.05	174.9	141.7
0.5	0.05	1.80	25.0	-	-	-	0.05	174.6	148.7
1	0.05	1.96	23.8	-	-	-	0.04	174.3	143.9
2	0.05	1.90	23.0	-	-	-	0.05	177.0	160.0
4	0.06	1.55	30.0	-	-	-	0.04	176.0	120.0
TMU									
0.06	0.05	1.5	30.0	-	-	-	0.04	177.0	129.6
0.12	0.06	2.0	23.2	-	-	-	0.04	175.0	130.0
0.25	0.07	2.0	21.5	-	-	-	0.05	171.9	130.0
0.5	0.09	1.6	23.4	-	-	-	0.05	172.5	139.9
1	0.09	1.5	19.5	-	-	-	0.05	173.3	180.1
2	0.19	1.3	23.7	-	-	-	0.07	172.0	140.0
4	0.22	1.3	20.5	-	-	-	0.08	169.0	148.8
6	0.30	1.0	0.11	-	-	-	0.08	172.0	140.0
8.3	0.30	1.0	28.5	-	-	-	0.05	172.3	145.3

TMU						
concentration/mol	A_{G2}	ω_{G2} /cm^{-1}	$\Delta\omega_{G2}$ /cm^{-1}	A_{G3}	ω_{G3} /cm^{-1}	$\Delta\omega_{G3}$ /cm^{-1}
1	0.04	56.3	54.2	0.01	133.3	78.1
2	0.03	47.6	58.0	0.01	136.0	29.4
4	0.14	54.4	60.0	0.03	132.0	60.0
6	0.11	52.9	57.6	0.02	130.2	48.1
8.3	0.11	51.4	50.7	0.05	106.7	70.1

Table 4.2 Fit parameters of Fourier Transform Kerr Spectra of formamide, urea, TMAO and TMU.BL denotes Bucaro-Litovitz, G Gaussian and ASG antisymmetrized Gaussian. Two extra components required to fit TMU are shown in separate table.

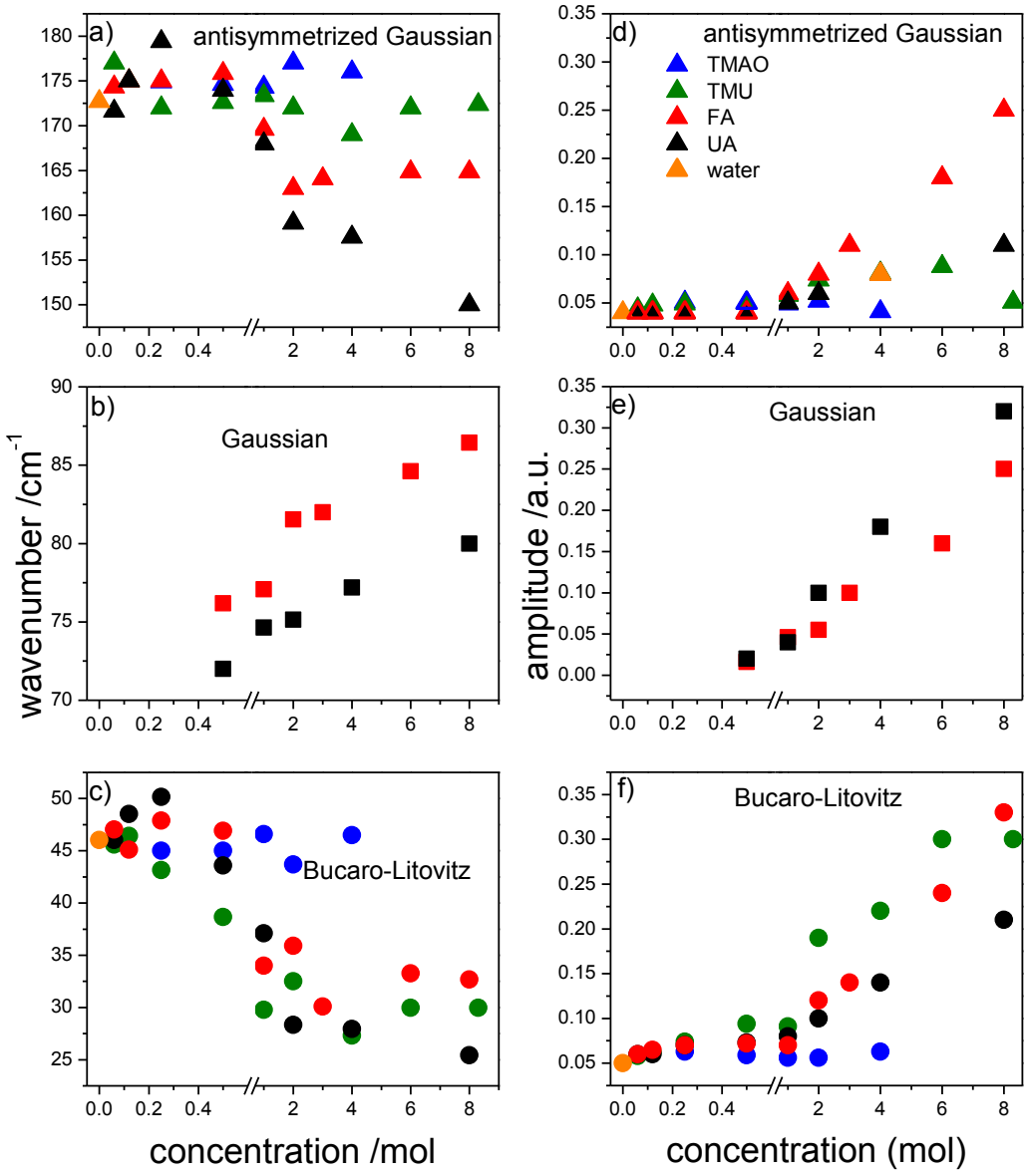

Figure 4.12 Frequency and amplitudes of fitted spectral components for all four solutes studied. Gaussian is the intermediate component observed for UA and FA, which is not required to fit the data below 0.5 M. Error ± 2%.

one intramolecular mode at 370 cm^{-1} is observed. Single intramolecular modes were calculated for UA and FA, see below for details.

It is clear from Figure 4.12 that for TMAO the amplitudes and frequencies of both BL and ASG functions over the whole concentration range are constant and, within

experimental error, the same as for pure water. This result indicates that the water structure, indicated by the characteristic bimodal Im $D'(\omega)$, is remarkably well preserved in the TMAO solutions, even at 4 M concentration. The retention of water structure near a hydrophobic solute is consistent with some molecular dynamics simulations[17] where it was found that the water hydrogen-bond network is little affected by the presence of a hydrophobic solute. The same conclusion was reached through the analysis of neutron scattering[38] data for methane-water solutions. The retention of this structure even at 4 M is however surprising as it is expected that at this concentration there are approximately 9 water molecules per TMAO molecule, all being a part of the first hydration shell of TMAO. This may suggest microscopic clustering of the TMAO solute to leave larger volumes of contiguous bulk like water. Alternatively, the water monolayer between solute molecules may still support a stretching O···O H-bonded mode, even though it must become much more localized than in bulk water.[57] In contrast to the THz Raman spectral density the mid IR absorption spectra of increasingly concentrated TMAO solutions were reported to reveal a red shift of the OH stretching mode.[58] Two explanations were suggested. First that there is a strengthening of water-water H-bonds in the vicinity of the hydrophobic TMAO methyl group[58] and second that the red shift is caused by an increasing fraction of strong H-bonds with the hydrophilic oxygen in TMAO.[15] In either case the present data suggest that the underlying tetrahedral water structure is not highly perturbed by the water – TMAO interactions.

The Im $D'(\omega)$ for FA and UA are composed of three modes, the BL, ASG and at high concentrations (>0.5 M), an intermediate frequency G mode. The low frequency Raman spectra of aqueous solutions of FA and UA have been discussed elsewhere.[8, 59-61] However the concentrations studied were typically at the higher end compared to

those considered here. At concentrations below 0.5 M, the Im $D'(\omega)$ of UA and FA are characterized only by the two modes characteristic of pure water at ~45 cm^{-1} and 175 cm^{-1} (Figure 4.9). The frequencies of both the BL and ASG modes are constant below 1 M but shift slightly to the red above this concentration, the biggest shift being observed for UA, Figure 4.12. The red shift is accompanied in both cases by increasing ASG amplitude, which is much more marked for FA than UA. The decrease in frequency of the ASG is assigned to the disruption or distortion of the tetrahedral structure in liquid water. This in turn indicates a perturbation to water-water hydrogen bonds by the solute. It is significant that at these high concentrations (>1 M) almost all water molecules will be found in the hydration shell of a solute, so it is apparently only under conditions of such high solute concentration that the water-water H-bond structure is significantly disrupted. The increase in amplitude of the ASG is more difficult to assign but may suggest a larger Raman cross section for water-UA/FA modes than for water-water modes, although for the highest FA concentrations a molecular component may become significant (see below).

As the concentration increases further the contribution of the solute orientational (librational) dynamics to the observed signal is expected to become more significant. Molecular dynamics simulations coupled to the calculation of polarizability anisotropy relaxation[51] suggest that above a mole fraction of 0.05 FA in water (*i.e.* a 2.5 M solution) the FA libration, (modified by its interaction with water) begins to make a significant contribution to the OKE signal. This contribution then increases further with additional FA. In line with this assignment the decrease in frequency of the ASG mode for FA continues only until a concentration of 6 M (Fig 4.12) above which it begins to increase, as the solute librational mode starts to dominate over the

water response, eventually reaching ~184 cm^{-1} for pure FA (25 M, data not shown); this mode in pure FA has previously been assigned to molecular libration.[60, 61]

The origin of the G mode in UA and FA has been considered further. The G mode required to fit the Im $D'(\omega)$ data FA and UA grows in importance at concentrations above 0.5 M. In order to confirm that this mode is associated with an oscillation, which appears at ~450 fs in the time domain, the inverse Fourier transform (IFT) was

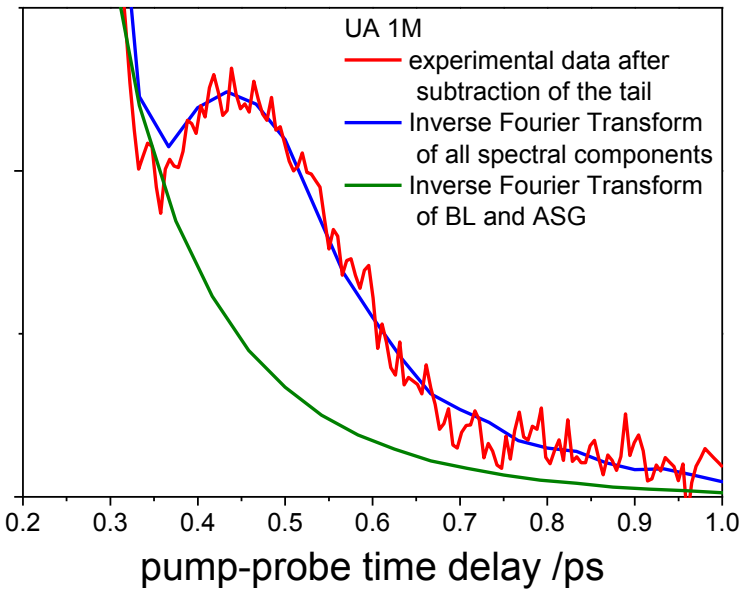

Figure 4.13 Inverse Fourier Transform of data recorded for Urea 1M. The IFT was performed after the diffusive tail was subtracted. From these data it can be seen that the peak around 450 fs in the time domain correlates with the Gaussian component in the frequency domain, which grows-in with increasing solute concentration.

performed. The IFT of all spectral components (ASG+BL+G) recovered the oscillation at 450 fs, Figure 4.13. However, when only BL + ASG were taken for IFT no such oscillation was recovered.

The amplitude of this mode increases linearly with concentration (Figure 4.12), which also suggests that it is associated with the solute. The frequency of the mode also increases with increasing concentration, suggesting the formation of stronger hydrogen bonded structures in the solution when fewer water molecules are available for solvation. Idrissi also resolved the low frequency Raman spectra for UA in water into three components.[59] In that work, a red shift of the ASG was recovered, as seenhere, but the low frequency component was reported to show an increase in frequency with increasing concentration while a constant frequency was found for the intermediate Gaussian mode. These small differences may arise because of the different fitting functions used (In this work: BL, G and ASG were used while Idrissi: used three G functions). Alternatively the spectra measured in the frequency domain below 50 cm^{-1} may not be as well resolved as in the OKE measurement (due to the thermal occupation factor).[59] DFT calculations were performed for UA with specific waters included, Figure 4.14. A new low frequency Raman active out-of-plane bending mode appears at 73 cm^{-1} for the complex. This suggests an assignment of G to a water-UA mode, consistent with the linear concentration dependence. However, a similar mode appeared for DFT calculations on UA dimers, yielding a 99 cm^{-1} mode with larger amplitude than the water-UA mode, suggesting an alternative assignment of G to a UA dimer mode. The formation of UA dimers were suggested by molecular dynamics simulations and infrared studies.[2, 7] Additional calculations on a UA dimer structure linked by two intervening water molecules also showed a band in the correct location for G (87 cm^{-1}). DFT calculations on the FA water complex also predict a mode near 100 cm^{-1} (Figure 4.15), but with a very small amplitude. In contrast, calculations on the FA dimer predict an intense mode of the correct frequency, favouring a dimer assignment for G in FA solutions. The key feature in all these

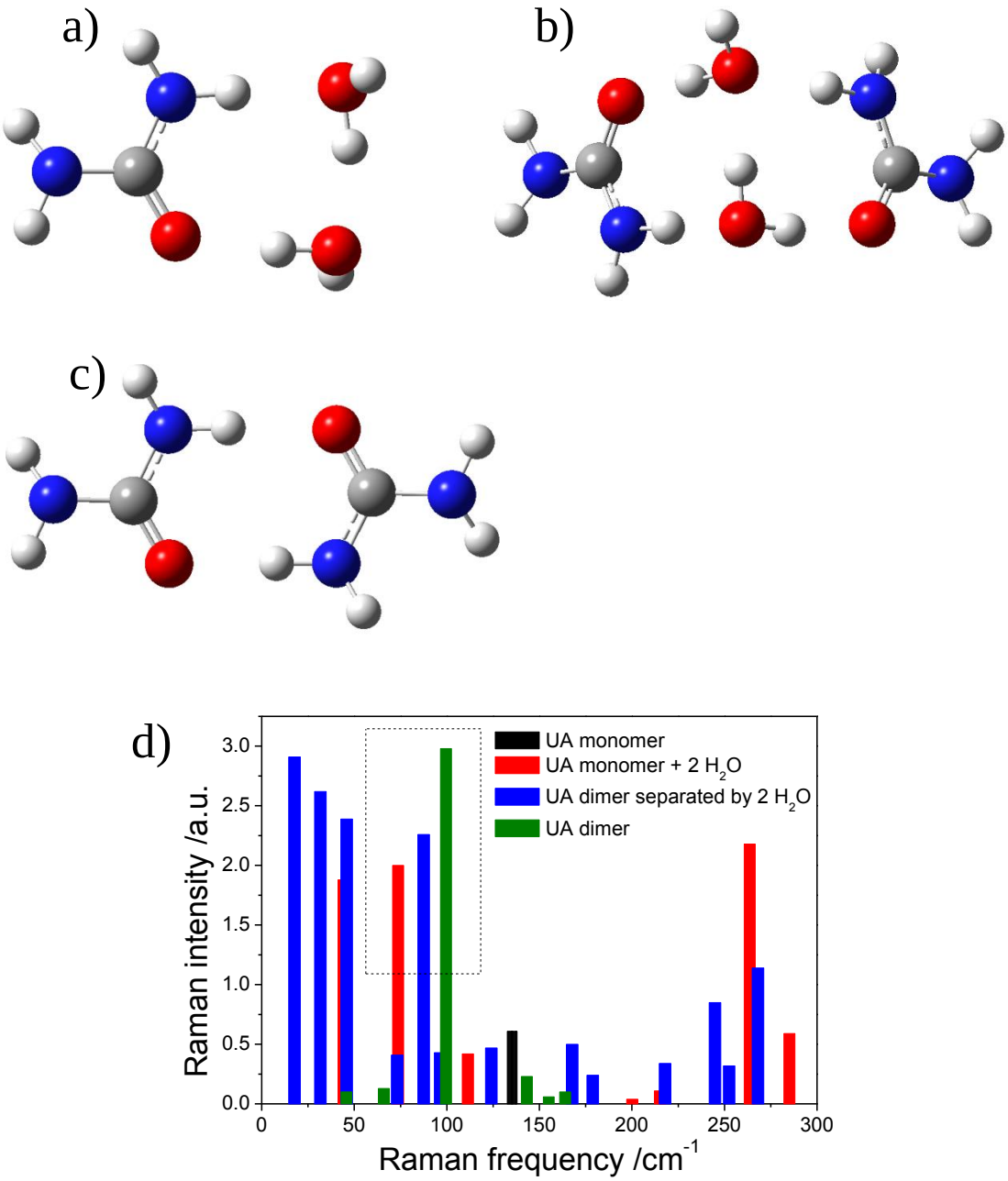

Figure 4.14 Optimized structure of a) urea monomer with two water molecules b) urea dimer separated by two water molecules, c) urea dimer .d) Raman frequencies obtained from DFT calculations. The G mode is marked with the frame.

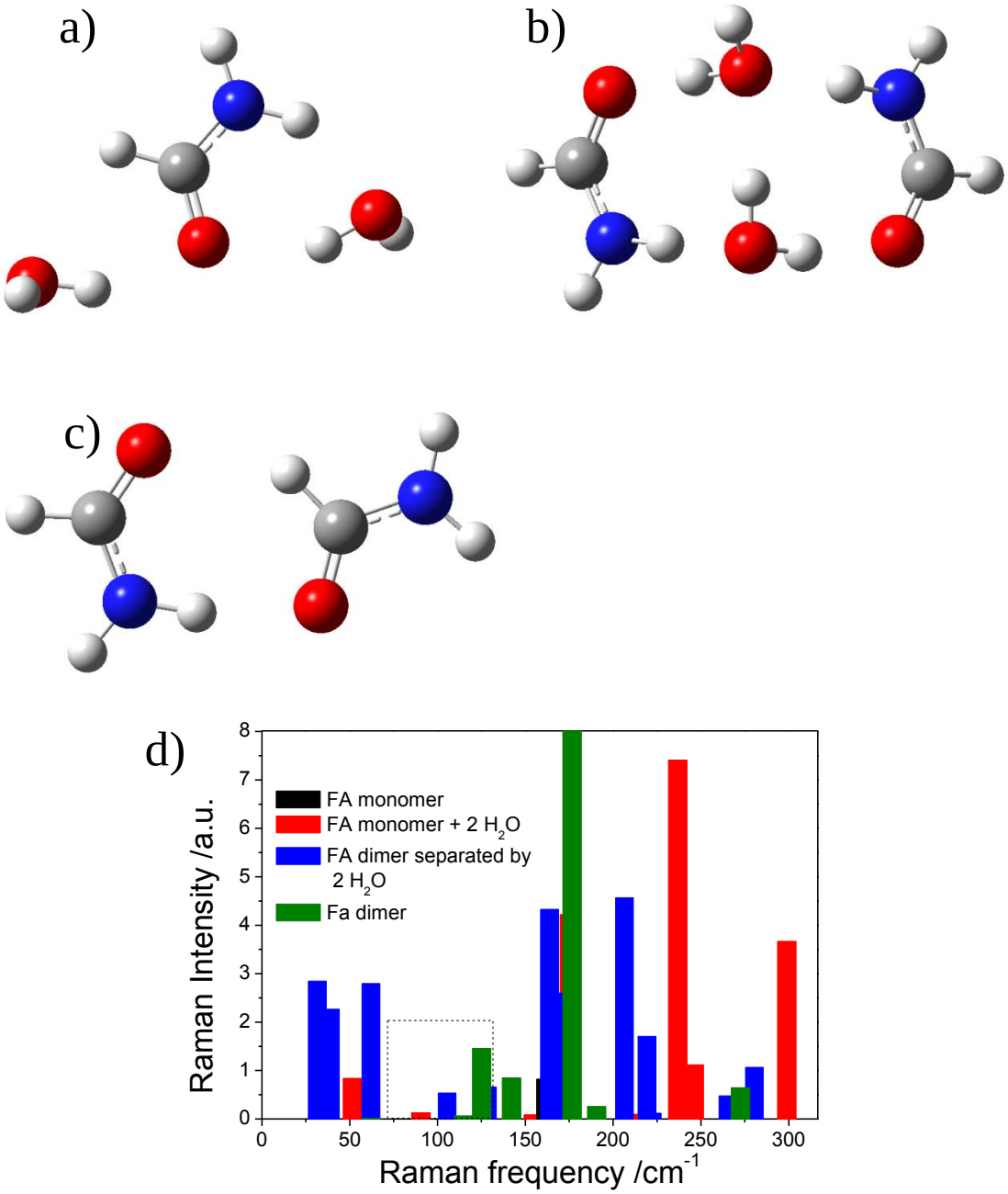

Figure 4.15 Optimized structures of a) formamide monomer with two water molecules, b) formamide dimer separated by two water molecules, c) formamide dimer. d) . Raman frequencies obtained from DFT calculations. The G mode is marked with the frame.

calculations is that this mode only arises in the presence of hydrogen bonding to the solute (either solvent-solute or solute-solute) and is not found in the isolated molecule.

Nielsen *et al.*[62] studied spectra of N-methylformamide and dimethylformamide and found a 90 cm^{-1} mode in the former but not the latter. He concluded that this mode is only present in amides capable of forming hydrogen bonds. Castner *et al.*[60] studied the same solutes using OHD-OKE and reached the same conclusion. On the basis of the DFT calculations and these previously mentioned studies we assign the G mode observed for FA and UA solutions to out-of-plane bending of an H-bonded solute complex, which may include both solute-solute and solute-water complexes, or a more extended solute-solvent network.

In the spectral densities of TMU (Figure 4.12), the BL band shifts to the lower frequency with increasing concentration and increases in amplitude. However, the ~175 cm^{-1} ASG mode, taken to be characteristic of the tetrahedral water structure, remains unchanged over the whole range of concentrations (Figure 4.12). The absence of a shift in this ASG mode suggests that the H-bonded water structure in the TMU-water solutions is similar to that of bulk water, as was observed for TMAO-water solutions. Thus, although the TMU assignment is less certain because of the complexity of the spectrum, the data are consistent with a weak perturbation to the water structure by this hydrophobic solute.

4.4.3 Conclusions

The ultrafast OHD-OKE experiment has been used to probe the dynamics of a series of aqueous solutions. Two hydrophobic and two hydrophilic solutes were investigated over concentration ranges from <0.1 M to saturated solutions or neat liquid. The OHD-OKE reports simultaneously the THz Raman spectral density of the solution and the collective picosecond relaxation dynamics of its H-bonded network. Two distinct concentration regimes were identified. At low concentration (<0.5 M) the

THz spectrum is similar to that of pure water showing that the water structure is largely retained. However, the nonexponential picosecond relaxation dynamics are slowed significantly by all solutes. The hydrophilic solutes are shown to be about twice as effective at slowing the dynamics as the hydrophobic solutes, when judged by a two state model (section 4.3).

As the concentration increases above 1 M the slowest component in the picosecond dynamics begins to dominate, consistent with an appreciable slow-down in the relaxation mechanism when the majority of water molecules are involved in a solute's solvation shell. In hydrophilic solutes this slow down correlates with disruption of the water structure in the THz Raman spectral density, specifically a red shift of the ca 175 cm^{-1} component observed in the pure water spectrum and assigned to H-bond stretching in a tetrahedral geometry. This suggests that the slowest dynamics at high solute concentration are associated with a disrupted water structure. The surprisingly weak perturbation to the spectral density by the hydrophobic TMAO is consistent with the hydrophobic solute having a minimal effect on the water structure. That this weak perturbation is maintained up to 4 M is suggestive of solute clustering in this solution. As the solute concentration increases the Raman spectral densities for FA, UA and TMU come to be dominated by the solute contribution. This is particularly marked for TMU, where low frequency molecular modes contribute at all frequencies. For the hydrophilic solutes UA and FA the changes in the water spectral density are accompanied by the growth of a new mode associated with an H-bonded solute structure, which may include H-bonded dimers.

4.5 Comparison of TMAO and TBA Aqueous Solutions.

The unaltered spectral densities < 300 cm^{-1} for different TMAO concentrations compared to bulk water (Figure 4.9c) was an unexpected result. To gain further insight into the H-bonded network in aqueous solutions of amphiphiles, the temperature dependence of 4 M TMAO will be now discussed. For comparison, a study of the related amphiphilic molecule, TBA (Figure 4.1) was chosen. TBA is geometrically very similar to TMAO having the same hydrophobic moiety but a different hydrophilic group. Despite the similarities in their structures, experimental and theoretical studies showed that the behaviour of both solutes in aqueous solutions is different. For example each molecule has a markedly different effect on protein conformation, with TBA tending to destabilize and TMAO to stabilize the protein structure.[63-66] It was suggested that they do so by indirect contact with the protein.[67] Therefore their effect on the protein must originate in the different effect these molecules exert on the structure and dynamics of the solvent. A number of experimental and theoretical studies reported that TBA tends to aggregate in aqueous solution while TMAO does not.[68-74] The reason why TBA is thought to aggregate while TMAO does not is related to the differences in their dipole moments, hydrophilic-hydrophobic content and hydrogen bonding propensity, *i.e.* TMAO forms stronger H-bonds with water than does TBA.[68, 71] Spatial distribution functions of the water oxygen atom surrounding both solutes obtained by molecular dynamics simulations[69] showed that there are more water molecules in the vicinity of hydrophobic groups of TMAO than TBA. It was suggested that the nitrogen atom in TMAO partially neutralized the hydrophobic effects of the methyl groups, thus disfavouring aggregation. Yet different molecular dynamics simulations[68] reported that the molecules differ significantly only in their electrostatic properties. Calculations showed that the average TMAO-water hydrogen bond energy is 80%

larger (more negative) than that of TBA-water. It was suggested that this is not due to different site charges, instead it arises from repulsion of hydroxyl group hydrogen of TBA and water. Molecular dynamics simulation,[68] NMR,[71] near infrared,[73] infrared and dielectric[75] studies also showed that the TMAO hydration shell is much more compact than that of TBA. This is caused by TMAO having a larger dipole moment than TBA ($\mu_{TMAO} \approx 3\mu_{TBA}$).

The dynamical properties of aqueous TBA solutions have been studied by means of molecular dynamics simulations,[13, 15] 2DIR[70] and neutron-scattering spectroscopy.[76] In neutron scattering[76] it was found that the effect of increasing solute concentration on the water dynamics is equivalent to an effect observed by lowering the temperature of pure water. Laage *et al.*[13, 15] using molecular dynamics simulation found that water dynamics in the vicinity of hydrophobic moieties are slowed down by a factor of 1.5 and 1.4 compared to pure water for TMAO and TBA, respectively. It was also reported that water around hydrophilic sites is slowed down by a factor of 4 for TMAO while the effect of hydrophilic groups of TBA was negligible. This result is contrary to the 2DIR studies[70] which showed that the observed slow down of water molecules is due to the hydrophobic and not the hydrophilic groups.

In order to better understand the effect these molecules have on water structure, first the concentration dependence of TBA at room temperature will be discussed and compared with that of TMAO, then their respective temperature dependence will be considered.

4.5.1 Concentration Dependent Dynamics of TBA-Water Solutions

The concentration dependence of the OKE response of the TBA-water solutions in the time domain is shown in Figure 4.16. The OKE traces reveal that the oscillation at

200 fs which is characteristic of pure water (Figure 4.16) is preserved in the TBA solutions. With increasing solute concentration, a new high frequency oscillatory

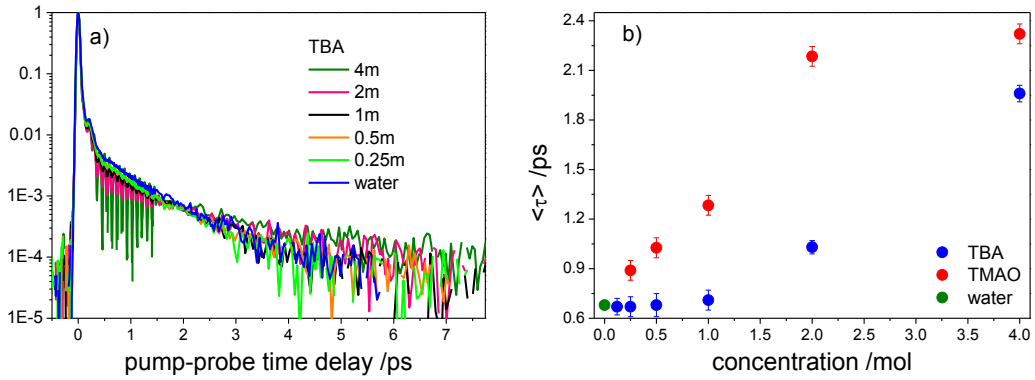

Figure 4.16 a) concentration dependence of Kerr transients for TBA, b) <τ> for TBA, TMAO and water plotted against concentration.

feature is observed. The amplitude of this new oscillation increases with increasing concentration, and corresponds to a Raman active solute intramolecular mode (see below). The same behaviour was observed for aqueous solutions of TMAO (Figure 4.4c).

The averaged relaxation time for both TBA and TMAO solutions extracted from a biexponential fit to the data for t > 1 ps, are plotted in Figure 4.16b. In the concentration range 0.12 - 1 M the <τ> values for TBA are indistinguishable from those of pure water, which indicates that at these concentrations the TBA molecule has a negligible effect on the water dynamics. This is in contrast to TMAO water solutions where already at concentrations as low as 0.25 M the water dynamics are significantly slowed down. This indicates that the strongly hydrophilic group of TMAO (N^+O^-) has a greater impact on the translational II water dynamics than does the O-H group of TBA. This is in agreement with molecular dynamics simulations[69] where it was reported that translational dynamics of water molecules in the solute's first hydration shell are more restrained by TMAO than TBA. In addition, the polarity

of the TBA O-H group is the same as that of the O-H groups of water.[70] This is consistent with the lack of an increase in relaxation time at low concentration of TBA solutions, because the water molecules do not distinguish whether they are H-bonded to another water molecule or to a TBA molecule. At a concentration of 2 M there is an increase in the $<\tau>$ measured for the TBA solution. Molecular dynamics simulations[68, 72, 77] and neutron scattering[78] studies showed that at approximately this concentration (2-3 M) clusters of 3-4 TBA molecules are formed. Therefore it is plausible that the observed sudden increase in relaxation time indicates the formation of TBA aggregates. TBA aggregates might cause water molecules to be trapped between TBA clusters, preventing the approach of a new water partner. This constraint is expected to result in the retardation of water orientational dynamics (*i.e.* an excluded volume effect),[13] which in turn may also influence the II dynamics which is observed in OKE measurements. It is also possible that the TBA dynamics accounts for the observed slower dynamics at the concentration > 2M.

To estimate the contribution of TBA molecules to the observed relaxation time, we applied the analysis described in section 4.4.1.1. We assumed that the averaged relaxation time is the sum of the relaxation times of bulk water and pure TBA weighted by their molar fraction, corrected for viscosity (Eq. 4.5). The relaxation times obtained are plotted in Figure 4.17. Pure TBA exists as a solid at room temperature, therefore its viscosity was extrapolated from the viscosity data given in ref.79 and 80. It's relaxation time was estimated from the relation: $\frac{\eta_{20C}}{\eta_{30C}} = \frac{<\tau>_{20C}}{<\tau>_{30C}}$, where η is the viscosity and τ is the averaged relaxation time at 20 ºC or 30 ºC.

The relaxation times obtained have the same values as the observed relaxation times in the concentrations up to 1 M. This confirms that at low concentration no slow water

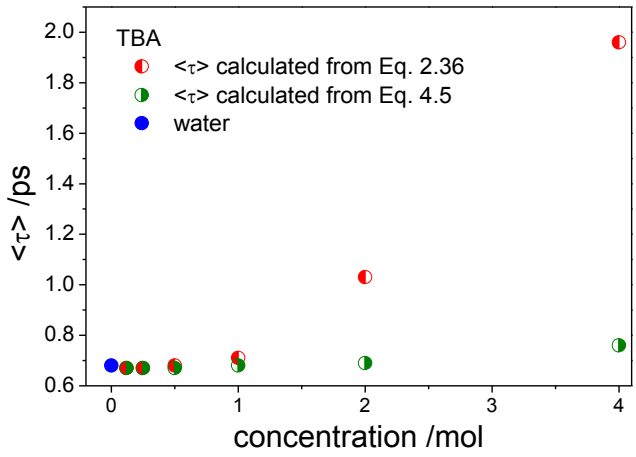

Figure 4.17 Comparison of the averaged relaxation time (red symbol) with the calculated from Eq. 4.5 (green symbol). The average relaxation time is shown as a reference (blue symbol).

population exists in the solution. Above this concentration the observed relaxation times increase significantly. This suggests that additional contributions must be occurring. We ascribe this contribution to the slow water relaxation of water in the water pools between TBA clusters.

To gain an insight into the H-bonded structure of the solutions studied, the time domain data were converted by Fourier transform (section 2.4) to the frequency domain representation. The Raman spectra of TBA solutions were previously reported by Tominaga *et al.*[81] and Sassi *et al.*[82] However, both studies were made at relatively high concentrations, >2.3 M (Tominaga) and >9.5 M (Sassi). Tominaga *et al.*[81] showed that the spectra of TBA-water solutions could be decomposed into linear combinations of the water and neat TBA spectrum in the frequency range 80 - 400 cm^{-1}. Sassi *et al.*[82] reported that the spectral evolution of the librational band (~ 50 cm^{-1}) observed by varying the concentration from pure TBA down to 9.5 M is similar to the effect produced by lowering the temperature of neat TBA. The low frequency reduced Raman spectra obtained via OHD-OKE measurements are shown in Figure

4.18a. The RSD of pure TBA is shown in green. The molecular mode at 345 cm^{-1} was previously assigned to an intramolecular C-C-C bending mode of TBA.[81] Apart from this intramolecular mode, the RSDs of aqueous solutions of TBA in the concentration range of 0.12 – 4 M resemble the spectrum of bulk water (shown in blue). The RSDs were fitted with BL and ASG functions at the concentrations up to 4 M. The intramolecular band at 345 cm^{-1} observed in the Raman spectrum was not included in the fit. The wavenumbers obtained from the fit are shown in Figure 4.18b.

The integrated area relative weights, shown in Figure 4.18c,d were calculated using the equation:

$$I_i = \frac{I_i}{I_{TOT}} \tag{4.7}$$

where i is either BL or ASG and I_{TOT} is the total integrated area of the RSD.

The spectra of both TBA and TMAO solutions exhibit a bimodal structure at the concentrations $\leq 4M$. The frequencies of both the BL and ASG bands obtained for TMAO are approximately constant with addition of TMAO and give values similar to those of water, Figure 4.18b. The same behaviour is observed for TBA up to a concentration of 2 M. However, above this concentration both bands shift gradually to the red. The shift of the BL band is associated with the growing contribution of the librational mode of TBA, which is present between 0 – 100 cm^{-1} in pure TBA (Figure 4.18a). To test this assumption, the RSD of 4 M TBA and pure TBA were normalized to the 345 cm^{-1} mode of the 4 M solution. The water spectrum was then added to the normalized spectrum of pure TBA. The resulting spectrum exhibits the same frequency of the BL band as was observed for the aqueous solution of 4 M TBA.

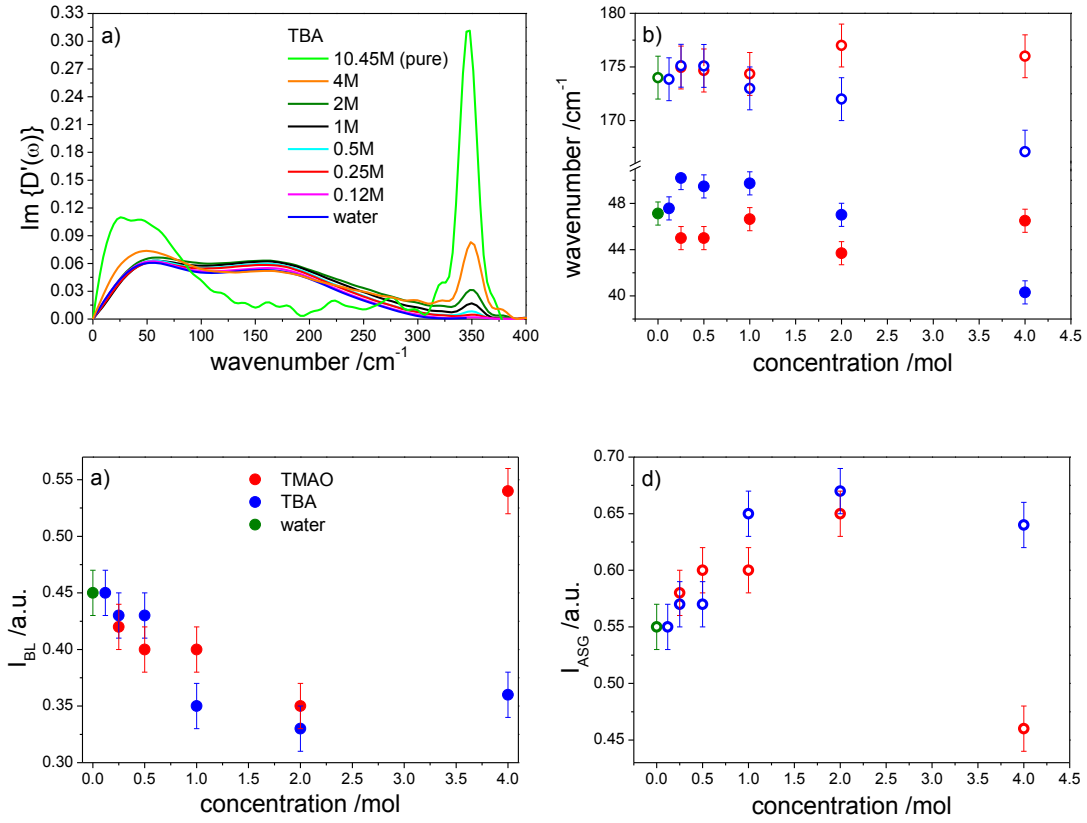

Figure 4.18 a)The RSD of TBA solutions over the entire range of concentration studied. Pure water is shown in blue. b) wavenumber obtained from analysis where a closed symbol denotes BL component and an open symbol is ASG. The red, blue and green are TMAO, TBA and water, respectively. Relative weight of integrated area of c) BL and d) ASG calculated from Eq. 4.7

Thus, the RSDs in the low frequency part (BL) are additive and the shift of the BL to lower frequency with increasing solute concentration is due to the growing contribution of the librational band of the TBA molecule. The ASG band was found no to be additive.

The spectral region between 100 cm^{-1} and 300 cm^{-1} arises from the H-bond interactions of solvent molecules. Therefore, the shift of the ASG band to lower frequency indicates a structural change of the solvent at these high concentrations. This is in agreement with previously published data[83, 84] where it was shown that there is a transition from a tetrahedral water structure to the zigzag structure typical of

alcohols at ~4 M. No shift in wavenumber for TMAO solutions indicates, as previously noticed, no change in water structure over the entire range of concentrations studied. However, from the weighted integrated area it is clear that with addition of the solute the ASG area of TMAO increases. This might indicate that the addition of solute enhances the water structure. The I_{BL} and I_{ASG} for both TMAO and TBA exhibit the same trend (Figure 4.18c,d) except for the 4 M sample. At 4 M the BL mode is the dominant mode for TBA, whereas for TMAO the biggest contribution to the spectrum is from the ASG mode.

4.5.2 Temperature Dependent Dynamics of Aqueous Solutions of TBA and TMAO.

The temperature dependence of TBA solutions at various concentrations has been the subject of a number of studies.[78, 83, 85-87] The majority of these were concerned with a structural picture rather than a dynamical one. As far as we are aware there are no data on the temperature dependence of TMAO solutions. Here, the dynamics of 4 M TBA and 4 M TMAO solutions as a function of temperature will be discussed. The concentration of 4 M was chosen because at this concentration TBA is believed to form clusters in the solution.[68, 72, 77, 78] Therefore temperature dependent studies will provide information on the clustering stability of TBA.

4.5.2.1 Picosecond Response.

Temperature dependence of the picosecond response of bulk water was studied with OHD-OKE spectroscopy by Winkler *et al.*[88] They fitted the picosecond relaxation decay with a double exponential. The time recovered for the slowest component was attributed to the diffusive single molecule rotational motion and the fastest time was linked to restricted translational modes in the H-bonded network. Both components

exhibit faster relaxation with increasing temperature. The oscillations at 50 fs and 175 fs become overdamped (oscillatory behaviour less pronounced) with increasing concentration, which is also observed in Figure 4.19c. However, it must be pointed out that average times obtained in our studies correspond to the fastest time recovered by Winkler *et al.*[88] The slowest time was not observed in our studies due to a worse signal to noise ratio.

The temperature dependence of the aqueous solutions studied is shown in Figure 4.19, where they are compared with the pure water data. The comparison of OKE responses for three samples studied at 80 ºC is shown in Figure 4.19d. It is immediately evident

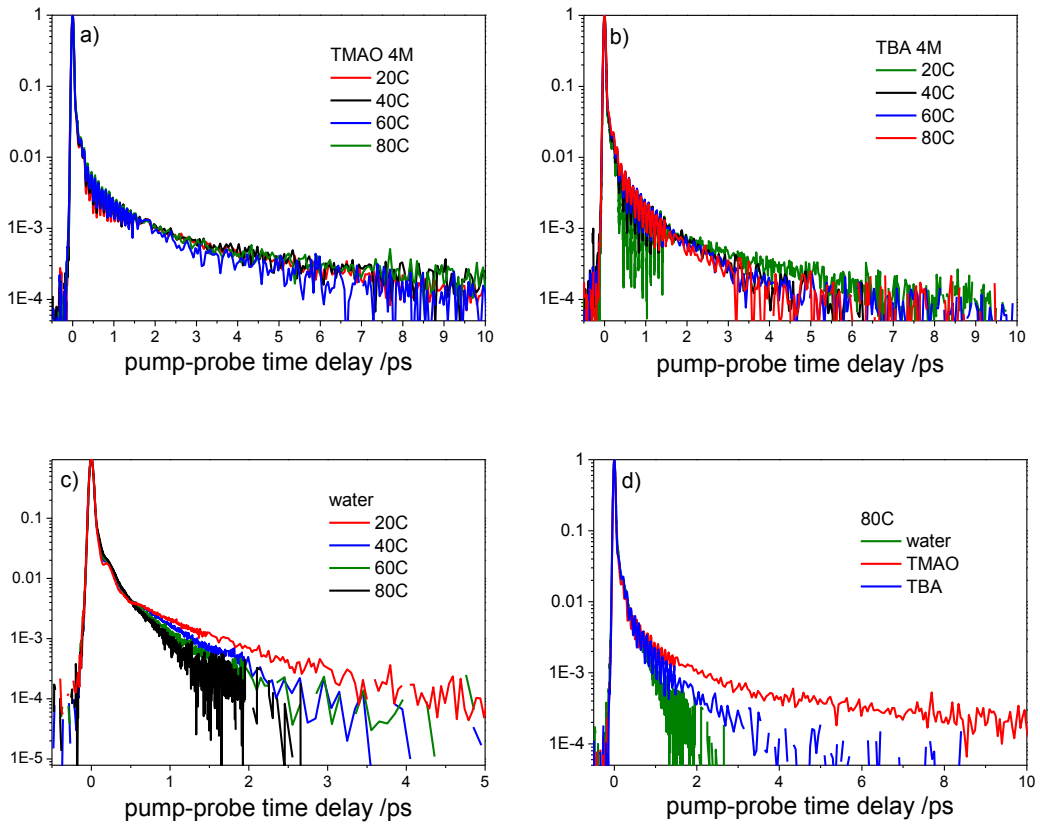

Figure 4.19 Temperature dependent OKE traces of 4M aqueous solutions of a) TMAO and b) TBA. Temperature dependence of pure water is shown in c) and comparison of water, TBA and TMAO at 80 ºC in d).

that with increasing temperature the relaxation time of pure water decreases, whereas for the solutions the temperature dependent dynamics are less marked and are solute dependent. For example, the picosecond relaxation of TMAO is temperature independent.

The picosecond response was fitted with a biexponential function (Eq. 2.34) and the average relaxation time calculated, $<\tau>$ (Eq. 2.35). The fitting parameters are listed in Table 4.3. The fitting parameters for individual relaxation times, τ_1 and τ_2 indicate that the long relaxation time (τ_2) is most temperature dependent. The $<\tau>$ plotted as a

function of η/T (DSE relation, chapter 2) are shown in Figure 4.20a. The $<\tau>$ obtained for TMAO solutions are essentially independent of viscosity and temperature. In TBA solutions a rather large drop in relaxation time, from 1.96 ps to 1.43 ps is observed, between 20 ºC and 30 ºC and then a further slight decrease was found between 40 ºC and 80 ºC. This behaviour is also reflected in the viscosity where only a small increase in temperature (10 ºC) results in a significant change in the viscosity from 4.2 cP to 2.6 cP. This might suggest that this small increase in temperature is sufficient to perturb the structural conformation of the sample, most likely by breaking TBA aggregates. The viscosity as a function of temperature for 4 M TBA, TMAO and pure water are plotted in Figure 4.20b. The relaxation times corrected by viscosity are shown in Figure 4.20c. For all solutions studied, $<\tau>/\eta$ increases with increasing temperature. However, this increase for pure water and TBA solutions is smaller than that recovered for TMAO. The relaxation time corrected by viscosity recovered for TBA at the highest temperature studied has a similar value to pure water. This indicates that even at the highest temperature, water dynamics in TBA solutions are similar to those present in pure water.

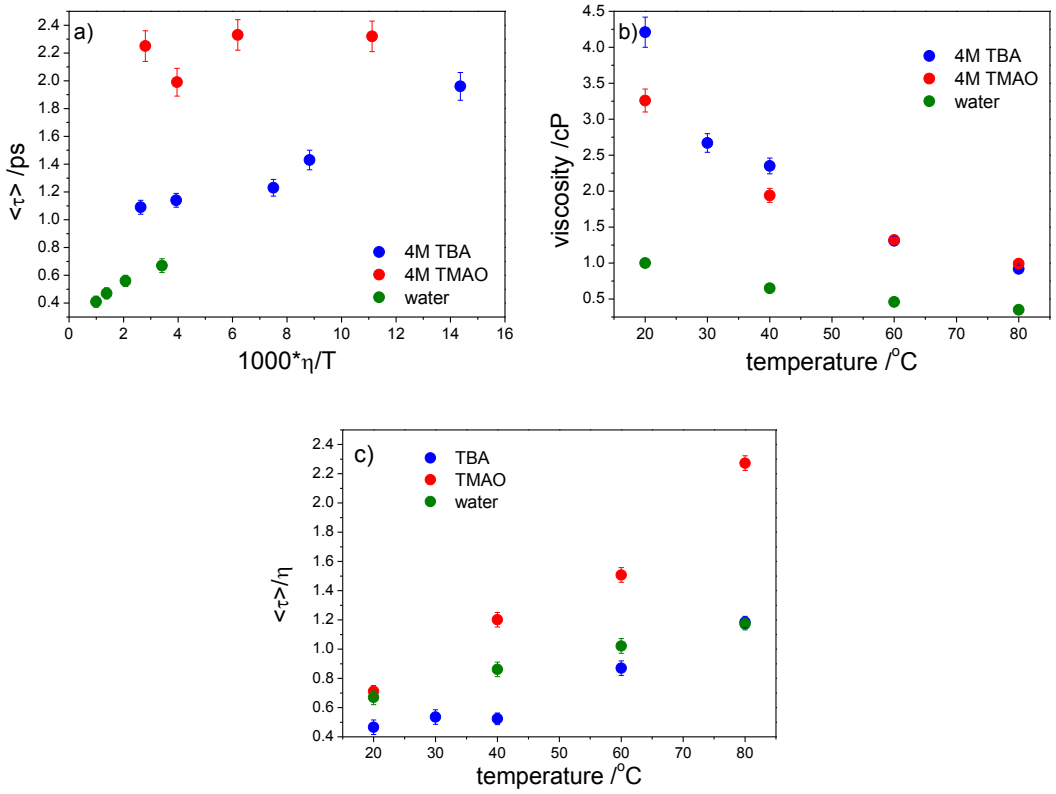

Figure 4.20 a) Averaged relaxation times plotted plotted as a function of *η/T.b) viscosity as a function of temperature and c) <τ>/η plotted as a function of temperature*

Neutron scattering,[89] UV absorption spectroscopy[83] and molecular dynamics simulations[78, 86, 89] showed that the temperature dependence of TBA solutions exhibit different behaviour at different concentrations. Neutron scattering studies[89] and molecular dynamics simulations[86, 89] showed that at a concentration of 1 M the TBA molecules remain in aqueous solution as free molecules or as linear dimers, connected by hydrophobic groups. An increase in temperature does not change the arrangement of TBA molecules in this solution. Similarly, at 2.6 M the size of the clusters formed by 3-4 TBA molecules was independent of temperature up to 120 ºC, but above 120 ºC clusters became unstable and disintegrated. However at an intermediate concentration between the two above (1.9 M) the observed behaviour of TBA clusters was different again.[86, 89] It was found, that at this concentration, TBA clusters increase

in size with increasing temperature with the maximum size being observed at 80 ºC. Above this temperature TBA clusters start to break up. An increase in cluster size with temperature at low concentration was also observed by means of steady state UV absorption spectroscopy,[83] but no maximum in the cluster size was observed in this study. At high solute concentrations (≥ 4 M) a transition from heterogeneous solution to a relatively more homogeneous one was observed. Thus, in these highly concentrated solutions an increase in temperature assists disaggregation.

The temperature dependence of $<\tau>$ observed for 4 M TBA is greater than for 4 M TMAO. At the concentration studied here there are approximately 9 water molecules per one molecule of TMAO, thus water molecules in the hydration shell of TMAO must be shared with another TMAO molecule if the solution is isotropic at the microscopic level. Removal of water molecules from this shell by varying physical parameters like temperature is more difficult for TMAO than for TBA.[90] This is because the hydration shell of TMAO is much more compact and stable than the

temperature /C	a_1	τ_1 /ps	a_2	τ_2 /ps	$<\tau>$/ps
water					
20C	0.80	0.46	0.20	1.51	0.67
40C	0.81	0.47	0.19	0.98	0.56
60C	0.81	0.39	0.19	0.83	0.47
80C	0.89	0.39	0.11	0.61	0.41
TMAO					
20C	0.83	1.44	0.17	8.20	2.32
40C	0.85	1.25	0.15	8.40	2.33
60C	0.88	1.12	0.12	8.40	1.99
80C	0.83	1.10	0.17	8.60	2.25
TBA					
20C	0.83	1.09	0.17	6.52	1.96
30C	0.82	1.04	0.18	3.19	1.43
40C	0.80	1.22	0.20	1.22	1.23
60C	0.76	1.13	0.24	1.20	1.14
80C	0.68	1.02	0.32	1.10	1.09

Table 4.3 Fitting parameters to Eq. 2.34.

hydration shell of TBA.[71] This is in agreement with the relaxation times observed here. By changing temperature, the structure of TMAO-water solutions apparently remains unaltered. TMAO molecules prevent water molecules from relaxing on the faster time scale observed in bulk water. The greater effect of TMAO molecules on the water dynamics is consistent with molecular dynamics simulations,[69] where it was reported that translational dynamics near TMAO are more restrained than around TBA. The decrease in relaxation times observed for TBA solutions follows a pattern similar to bulk water, that is the relaxation dynamics accelerate with increasing temperature. Bakker *et al.*[87] studied the temperature dependence of ~1 M TBA solutions with mid-infrared ultrafast spectroscopy. They found that with an increase in temperature the reorientation time of water molecules within the hydration shell accelerates. They found that at 25 ºC the hydration water was five times slower than the bulk, but at 65 ºC this value decreased to only two. They assigned the slow low temperature orientational dynamics to a slowing down of the structural dynamics of the H-bonded network in the vicinity of hydrophobic groups. In the average relaxation times recovered from OKE measurement it is clear that the water dynamics become faster with increasing temperature, but to a smaller extent than was observed in mid-infrared spectroscopy. There are two reasons for this discrepancy: (1) OKE probes translational dynamics of water rather than orientational; (2) at the much higher concentrations of TBA solutions studied here, aggregation/disaggregation of TBA molecules must be taken into consideration.

4.5.2.2 THz Raman Spectral Density Analysis

To gain an insight into the H-bond structure in these solutions the Fourier Transform of the time domain data were performed to recover the RSD as described in section 2.4.2. The temperature dependent RSD for 4 M TMAO, TBA and water are shown in

Figure 4.21. Comparison of the normalized spectra at 80 ºC for TBA, TMAO and water are shown in Figure 4.21d. It is immediately evident that the intensity of the ~45 cm^{-1} band increases with increasing temperature in all cases. The evolution of the ~175 cm^{-1} band is more complex and solute dependent.

Figure 4.21c shows that water RSDs are temperature dependent as the strength and length of the hydrogen bond is sensitive to temperature changes.[91] A number of studies showed that when temperature is increased the H-bond becomes weaker[91-94] and a breakdown of the tetrahedral structure of water is observed.[93] In particular, Walrafen *et al.*[94] studied the temperature dependence of the water Raman spectra.

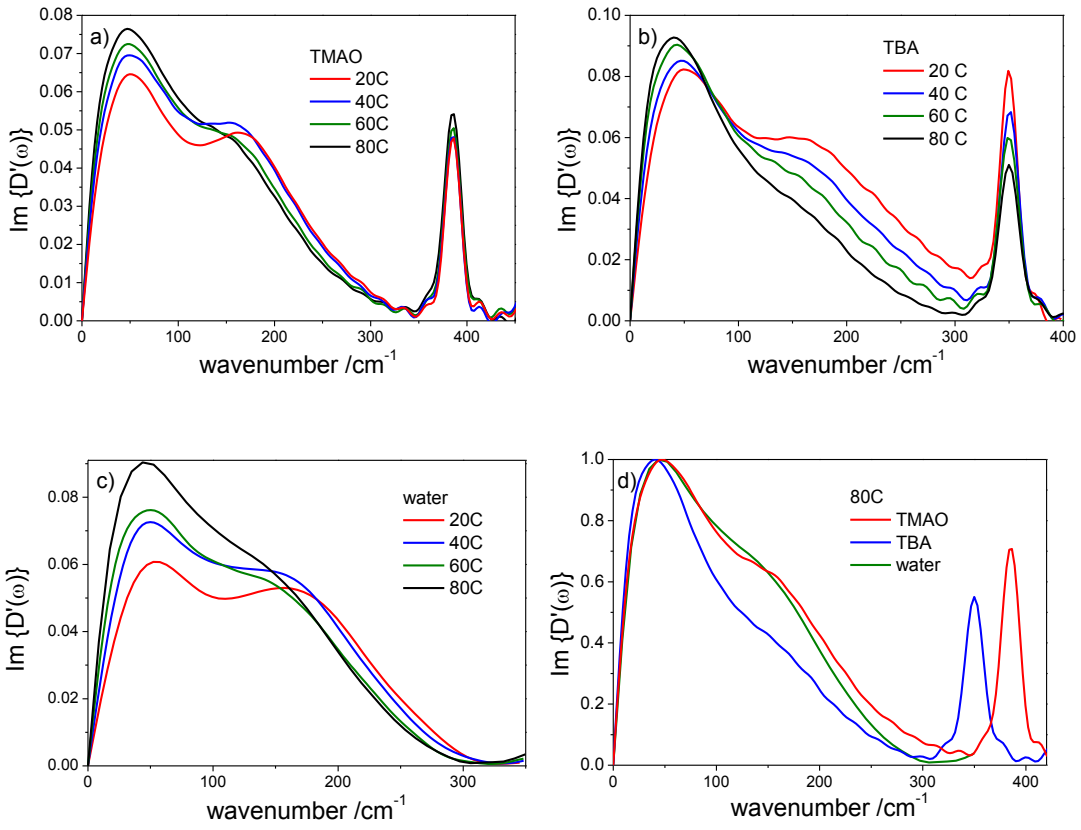

Figure 4.21 The evolution of RSD spectra with temperature for 4M solution of a) TMAO and b) TBA. Pure water is plotted in c) and d) comparison of normalized RSD at 80C.

They showed that when the temperature is increased, both the ~45 cm^{-1} and 175 cm^{-1} bands shift to lower frequencies. The same behaviour was observed in our study (Figure 4.21c and 4.22a,b). The decrease in frequency of the higher frequency mode was correlated to a decrease in the stretching force constant of the H···O bond of the O-H···O unit. Such a decrease in the force constant is consistent with an increase in the length of the O···H bond.[91] It was suggested that the shift of the ~45 cm^{-1} band indicated a decrease in the bending force constant. However, it was also suggested that in order for the bending force constant to be smaller, an increase in the O-H···O angle towards a more planar structure is expected. Larger angles lower the O···O repulsion by moving the oxygen atoms further apart.[95] However, it was concluded that an almost linear H-bond could be stronger and not weaker than the H-bond at room temperature. Thus the interpretations for ~45 cm^{-1} and 175 cm^{-1} contradict each other. It was suggested that to have weaker bending and stretching force constants, the decrease in the partial covalency of the O···H mode is required because both modes are active by virtue of this partial covalency.[94]

The spectral densities were fitted up to 300 cm^{-1} with BL and ASG functions. Parameters obtained from the fit are listed in Table 4.4, and the frequencies recovered are plotted in Figure 4.22. Both BL and ASG modes of pure water, TBA and TMAO solutions shift to lower frequencies with increasing temperature. The shift of the ASG band indicates the weakening of the water-water H-bond as observed for pure water. However, the relative weight of the integrated areas of both modes show distinctly different trends for TBA and TMAO. The T dependent I_{BL} and I_{ASG} for TMAO are similar to the values obtained for bulk water, Figure 4.22c,d. They show a growing contribution of the ASG mode at the expense of the BL mode. The normalized spectra at 80 ºC for TBA, TMAO and water show the strong resemblance of the TMAO and

temperature /C	A_{BL}	α	ω_{BL} /cm^{-1}	A_{ASG}	ω_{ASG} /cm^{-1}	$\Delta\omega_{ASG}$ /cm^{-1}
water						
20C	0.05	1.55	31.3	0.04	175.1	132.8
40C	0.06	1.48	29.9	0.04	164.0	135.7
60C	0.06	1.28	30.4	0.04	151.7	144.5
80C	0.08	1.25	31.2	0.04	146.9	143.8
TMAO						
20C	0.06	1.55	30.0	0.04	176.0	120.0
40C	0.06	1.42	30.0	0.04	168.0	151.2
60C	0.06	1.26	30.4	0.03	155.9	164.5
80C	0.06	1.22	30.7	0.03	149.9	169.6
TBA						
20C	0.06	1.55	26.0	0.05	167.1	198.1
40C	0.07	1.17	35.8	0.04	165.2	176.0
60C	0.07	1.22	29.5	0.03	149.5	175.9
80C	0.08	1.13	30.5	0.02	144.5	157.4

Table 4.4 Parameters obtained by fitting RSD with Bucaro-Litovitz (BL) and antisymmetrized Gaussian (ASG) functions.

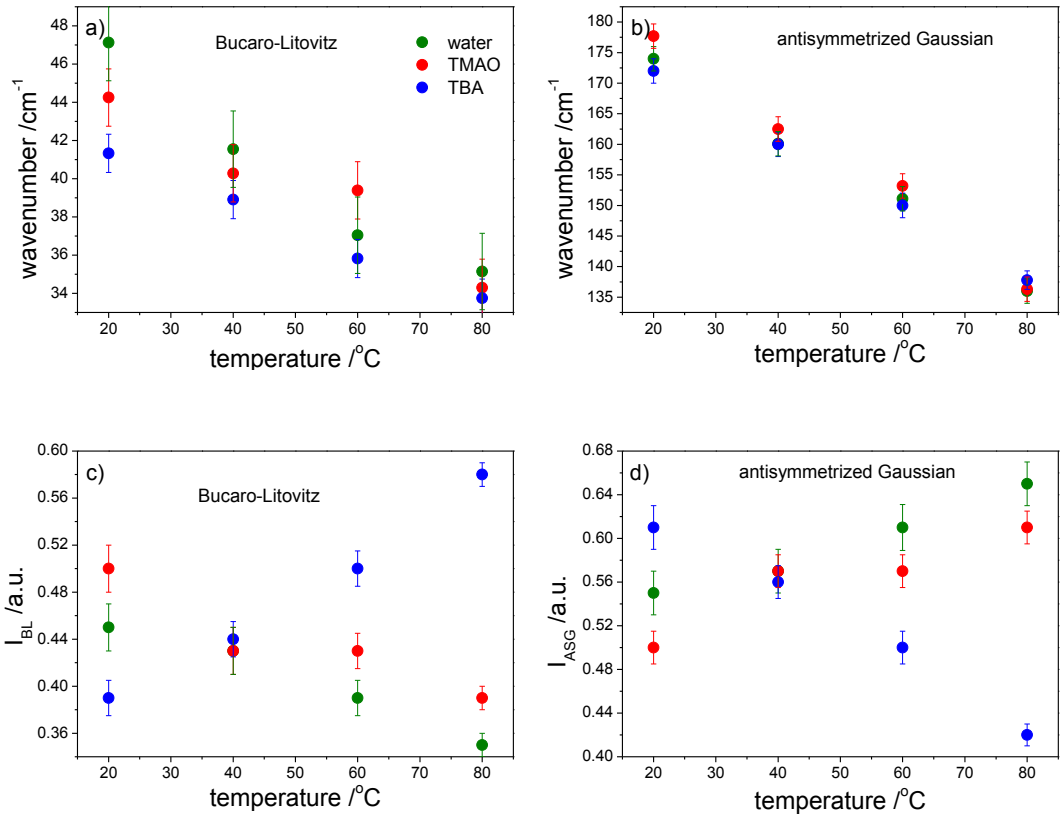

Figure 4.22 Wavenumbers obtained from the fit to a) BL and b) ASG. Weighted integrated area of c) BL and d) ASG. See Eq. 4.7 for details.

water spectra even at 80 ºC. Relative integrated areas calculated for TBA solutions show the opposite trend to that observed for water and TMAO. In TBA solutions the I_{ASG} band decreases with increasing temperature. This discrepancy between water and TBA solutions indicates that there is a change in the distribution of H-bonds in the water with increasing temperature. Thus the behaviour of TBA is clearly different to both bulk water and the TMAO solution. When temperature is increased, the TBA clusters may break up as was suggested by UV absorption spectroscopy.[83] As a result more water must be accommodated in the solvation shells of TBA, Figure 4.23. This is reflected in the I_{ASG} behaviour. I_{ASG} decreases with increasing temperature indicting gradual loss of the tetrahedral water structure. The increase in temperature cannot be associated with an increase in cluster size at this concentration (4 M) as already concluded.[83] An increase in TBA cluster size would be associated with an increase in water pools size, which in turn would lead to an enhancement of water structure with increasing temperature. This is not observed in OKE measurements.

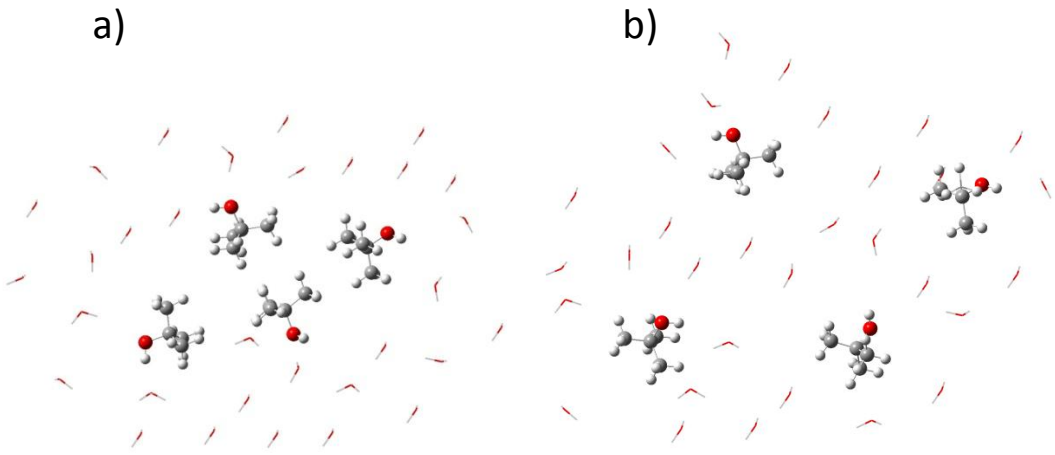

Figure 4.23 Conceptual diagram of a) TBA cluster with hydration water and b) free TBA molecules with their hydration water.

The intramolecular vibrational band observed for TMAO (380 cm^{-1}) and TBA (350 cm^{-1}) also exhibit quite different behaviour with increasing temperature. The amplitude of this band is approximately temperature independent for TMAO solutions. However for TBA this intramolecular band decreases in amplitude with increasing temperature, Figure 4.21b. The decrease in the intensity of this intramolecular band is most likely associated with disaggregation.

4.5.3 Conclusions

The concentration studies of aqueous solutions of TBA and TMAO showed that TMAO has a larger effect on picosecond water dynamics. At concentrations as low as 0.25 M TMAO, a significant slow down of water dynamics was observed, while the relaxation dynamics in TBA solutions resembles that of pure water up to a concentration 2 M. This is in agreement with molecular dynamics simulations[69] where it was shown that translational dynamics of water are more restrained in TMAO than TBA solutions. The result also confirms that the hydrophobic sites have a negligible effect on water dynamics. The temperature dependence of the OKE traces for 4 M aqueous solutions were also studied. It was found that an increase in the temperature is accompanied by a faster relaxation time in TBA solution and also in pure water. The largest difference in relaxation times was observed between 20 ºC and 30 ºC, this is probably due to the breaking up of TBA aggregates as is reflected in viscosity. The relaxation time of TMAO was found to be independent of temperature.

The temperature dependent RSD spectra of TMAO resemble those of bulk water below 300 cm^{-1}. This indicates that the TMAO-water structure is temperature independent, at least in the range studied. For structurally similar TBA, however, it was found that the RSD is a strong function of temperature, probably a result of the gradual disaggregation. The RSD of TBA show that with increasing temperature, the

area of ~175 cm^{-1} associated with a water H-bond stretching mode decreases. This is due to rearrangement of water molecules in the solutions, as they must be accommodated in the hydration shells of TBA.

4.6 Additional Analysis

The presented analysis was performed assuming that only water contributed to the slow picosecond dynamics observed, especially in the low concentration region. To assess the effect of solute on the observed OKE signal, further analysis was performed.

Firstly, the integrated area of the recorded (not normalized) pure FA signal was divided by the integrated area of the pure water signal in order to estimate the strength of the FA signal compared to water, Figure 4.24. FA was chosen because pure FA exists as a liquid at room temperature. The calculated value was 13.

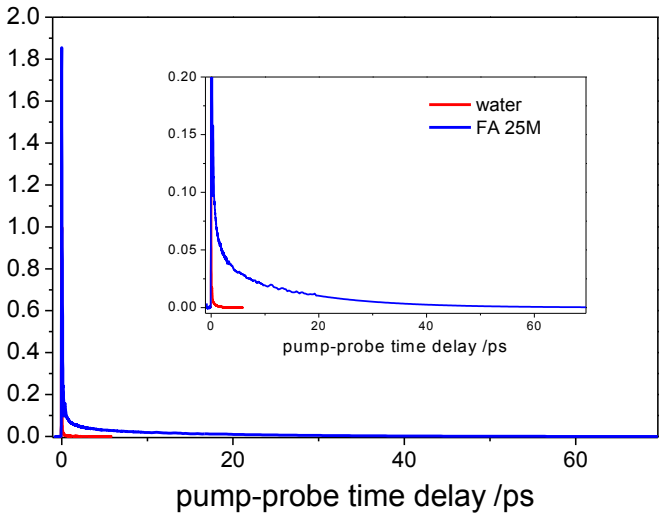

Figure 4.24. Comparison of OKE traces and water.

Then the relaxation time, assuming that only pure water and FA contribute to the observed signal, was calculated from Eq.4.5, but now with the contribution of FA increased by a factor of 13.

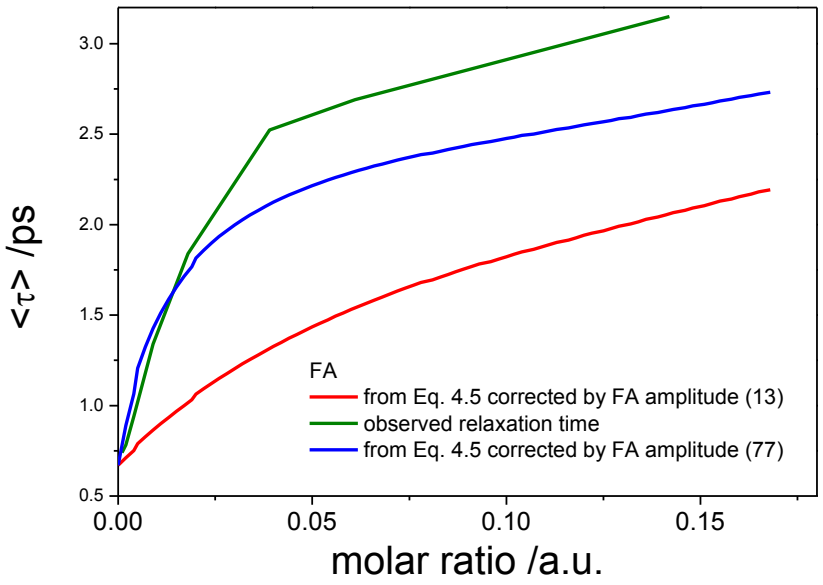

Figure 4.25. Observed and calculated (Eq. 4.5) relaxation times for FA. The amplitude of FA was multiplied by a factor of 13 and 77, see above.

It is clear from figure 4.25 that the observed time is not simply the sum of the relaxation times of pure water and FA weighted by a molar fraction and corrected by the FA amplitude factor of 13. However if the FA contribution was multiplied by a factor of 77, this qualitatively reproduced the low concentration relaxation times. Therefore it might be possible that even at very low concentration (0.06 M) the FA contribution is significantly larger that we assumed in our previous analysis (section 4.4.1.1).

To investigate it further, OKE time domain traces were analysed assuming their additivity. Thus, the OKE signal of water was corrected by molar fraction and added

to the FA signal corrected by molar fraction. This was done for three different concentrations. The obtained OKE trace for FA 0.5M is shown in Figure 4.26a. The obtained OKE traces were fitted with biexponential functions and then the average relaxation time was calculated using Eq. 2.34, correcting the τ_2 by viscosity (Eq. 4.6). Again, the obtained relaxation times are faster than the ones recovered from experiment, suggesting existence of a slow water population.

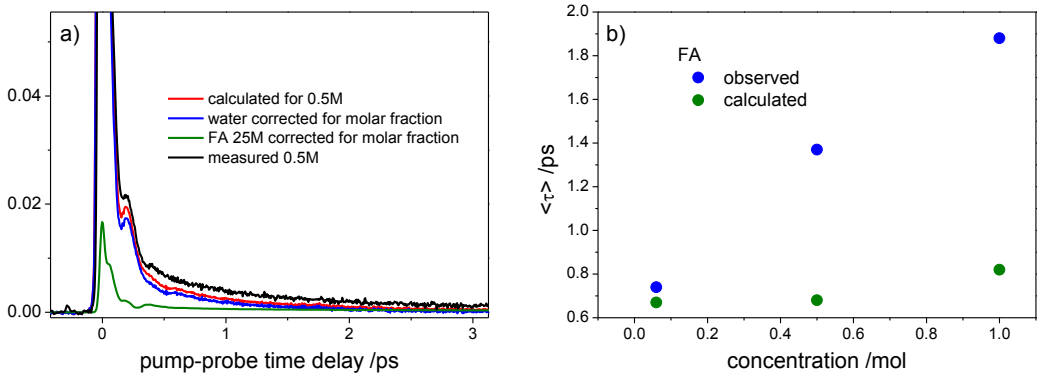

Figure 4.26. Reconstructed OKE traces for FA 0.5 M assuming that water and FA signals are additive.

4.7 References

1. A. A. Bakulin, C. Liang, T. L. Jansen, D. A. Wiersma, H. J. Bakker and M. S. Pshenichnikov, *Acc. Chem. Res.*, 2009, **42**, 1229-1238.
2. J. Grdadolnik and Y. Marechal, *J. Mol. Struct.*, 2002, **615**, 177-189.
3. B. Halle, *Philosophical Transactions of the Royal Society of London Series B-Biological Sciences*, 2004, **359**, 1207-1223.
4. M. E. Johnson, C. Malardier-Jugroot, R. K. Murarka and T. Head-Gordon, *J. Phys. Chem. B*, 2009, **113**, 4082-4092.
5. P. Ball, *Chem. Rev.*, 2008, **108**, 74-108.
6. D. Russo, G. Hura and T. Head-Gordon, *Biophys. J.*, 2004, **86**, 1852-1862.
7. J. Hernandezcobos, I. Ortegablake, M. Bonillamarin and M. Morenobello, *J. Chem. Phys.*, 1993, **99**, 9122-9134.
8. A. Idrissi, P. Bartolini, M. Ricci and R. Righini, *J. Chem. Phys.*, 2001, **114**, 6774-6780.
9. Y. L. A. Rezus and H. J. Bakker, *Phys. Rev. Lett.*, 2007, **99**, 148301.
10. Y. L. A. Rezus and H. J. Bakker, *J Phys Chem*, 2008, **112**, 2355-2361.
11. V. Helms, *Chemphyschem*, 2007, **8**, 23-33.

12. G. A. Papoian, J. Ulander, M. P. Eastwood, Z. Luthey-Schulten and P. G. Wolynes, *P. Natl. Acad. Sci. USA*, 2004, **101**, 3352-3357.
13. D. Laage, G. Stirnemann and J. T. Hynes, *J Phys Chem* 2009, **113**, 2428-2435.
14. J. Qvist and B. Halle, *J. Am. Chem. Soc.*, 2008, **130**, 10345-10353.
15. G. Stirnemann, J. T. Hynes and D. Laage, *J. Phys. Chem. B*, 2010, **114**, 3052-3059.
16. S. Ebbinghaus, S. J. Kim, M. Heyden, X. Yu, U. Heugen, M. Gruebele, D. M. Leitner and M. Havenith, *P. Natl. Acad. Sci. USA*, 2007, **104**, 20749-20752.
17. A. Kuffel and J. Zielkiewicz, *J. Chem. Phys.*, 2010, **133**.
18. P. Belletato, L. C. G. Freitas, E. P. G. Areas and P. S. Santos, *PCCP*, 1999, **1**, 4769-4776.
19. A. K. Soper, E. W. Castner and A. Luzar, *Biophys. Chem.*, 2003, **105**, 649-666.
20. A. Pullman, H. Berthod, C. Giessnerprettre, J. F. Hinton and D. Harpool, *J. Am. Chem. Soc.*, 1978, **100**, 3991-3994.
21. H. Zhao, *Biophys. Chem.*, 2006, **122**, 157-183.
22. Herskovi.Tt and T. M. Kelly, *J. Phys. Chem.*, 1973, **77**, 381-388.
23. H. Y. Wei, Y. B. Fan and Y. Q. Gao, *J. Phys. Chem. B*, 2010, **114**, 557-568.
24. N. K. Szekely, L. Almasy and G. Jancso, *J. Mol. Liq.*, 2007, **136**, 184-189.
25. G. E. Walrafen, *J. Chem. Phys.*, 1966, **44**, 3726-&.
26. G. G. Hammes and P. R. Schimmel, *J. Am. Chem. Soc.*, 1967, **89**, 442-&.
27. Y. Hayashi, Y. Katsumoto, S. Omori, N. Kishii and A. Yasuda, *J. Phys. Chem. B*, 2007, **111**, 1076-1080.
28. R. Chitra and P. E. Smith, *J. Phys. Chem. B*, 2000, **104**, 5854-5864.
29. M. C. Stumpe and H. Grubmuller, *J. Phys. Chem. B*, 2007, **111**, 6220-6228.
30. A. Sacco and M. Holz, *Journal of the Chemical Society-Faraday Transactions*, 1997, **93**, 1101-1104.
31. Subraman.S, Balasubr.D and Ahluwali.Jc, *J. Phys. Chem.*, 1969, **73**, 266-&.
32. K. Jerie, A. Baranowski, J. Glinski and K. Orzechowski, *J. Phys. IV*, 1993, **3**, 135-137.
33. X. Hoccart and G. Turrell, *J. Chem. Phys.*, 1993, **99**, 8498-8503.
34. A. Idrissi, M. Gerard, P. Damay, M. Kiselev, Y. Puhovsky, E. Cinar, P. Lagant and G. Vergoten, *J. Phys. Chem. B*, 2010, **114**, 4731-4738.
35. A. Tovchigrechko, M. Rodnikova and J. Barthel, *J. Mol. Liq.*, 1999, **79**, 187-201.
36. A. Shimizu, K. Fumino, K. Yukiyasu and Y. Taniguchi, *J. Mol. Liq.*, 2000, **85**, 269-278.
37. H. S. Frank and M. W. Evans, *J. Chem. Phys.*, 1945, **13**, 507-532.
38. P. Buchanan, N. Aldiwan, A. K. Soper, J. L. Creek and C. A. Koh, *Chem. Phys. Lett.*, 2005, **415**, 89-93.
39. W. Blokzijl and J. B. F. N. Engberts, *Angew. Chem. Int. Edit.*, 1993, **32**, 1545-1579.
40. G. Hummer, S. Garde, A. E. Garcia, A. Pohorille and L. R. Pratt, *P. Natl. Acad. Sci. USA*, 1996, **93**, 8951-8955.
41. K. Hallenga, J. R. Grigera and H. J. C. Berendsen, *J. Phys. Chem.*, 1980, **84**, 2381-2390.
42. R. Haselmeier, M. Holz, W. Marbach and H. Weingartner, *J. Phys. Chem.*, 1995, **99**, 2243-2246.
43. Y. Ishihara, S. Okouchi and H. Uedaira, *Journal of the Chemical Society-Faraday Transactions*, 1997, **93**, 3337-3342.

44. P. L. Silvestrelli, *J. Phys. Chem. B*, 2009, **113**, 10728-10731.
45. P. J. Rossky and M. Karplus, *J. Am. Chem. Soc.*, 1979, **101**, 1913-1937.
46. D. Laage, G. Stirnemann and J. T. Hynes, *Sci China Phys Mech Astron*, 2010, **53**, 1068-1072.
47. F. Sterpone, G. Stirnemann, J. T. Hynes and D. Laage, *J. Phys. Chem. B*, 2010, **114**, 2083-2089.
48. M. S. Pshenichnikov, A. A. Bakulin, H. J. Bakker and C. Petersen, *J. Phys. Chem. A*, 2011, **115**, 1821-1829.
49. M. Paolantoni, P. Sassi, A. Morresi and S. Santini, *J. Chem. Phys.*, 2007, **127**.
50. G. G. Szpiro, *Kepler's Conjecture*, John Wiley & Sons, 2003.
51. M. D. Elola and B. M. Ladanyi, *J. Chem. Phys.*, 2007, **126**.
52. S. L. Lee, P. G. Debenedetti and J. R. Errington, *J. Chem. Phys.*, 2005, **122**.
53. K. J. Tielrooij, J. Hunger, R. Buchner, M. Bonn and H. J. Bakker, *J. Am. Chem. Soc.*, 2010, **132**, 15671-15678.
54. N. T. Hunt, A. R. Turner, H. Tanaka and K. Wynne, *J. Phys. Chem. B*, 2007, **111**, 9634-9643.
55. N. A. Smith and S. R. Meech, *Int. Rev. Phys. Chem.*, 2002, **21**, 75-100.
56. H. Shirota, T. Fujisawa, H. Fukazawa and K. Nishikawa, *Bull. Chem. Soc. Jpn.*, 2009, **82**, 1347-1366.
57. I. Ohmine and S. Saito, *Acc. Chem. Res.*, 1999, **32**, 741-749.
58. K. A. Sharp, B. Madan, E. Manas and J. M. Vanderkooi, *J. Chem. Phys.*, 2001, **114**, 1791-1796.
59. A. Idrissi, *Spectrochimica Acta Part a-Molecular and Biomolecular Spectroscopy*, 2005, **61**, 1-17.
60. Y. J. Chang and E. W. Castner, *J. Chem. Phys.*, 1993, **99**, 113-125.
61. Y. J. Chang and E. W. Castner, *J. Phys. Chem.*, 1994, **98**, 9712-9722.
62. S. E. M. Colaianni and O. F. Nielsen, *J. Mol. Struct.*, 1995, **347**, 267-283.
63. P. H. Yancey, M. E. Clark, S. C. Hand, R. D. Bowlus and G. N. Somero, *Science*, 1982, **217**, 1214-1222.
64. Q. Zou, B. J. Bennion, V. Daggett and K. P. Murphy, *J. Am. Chem. Soc.*, 2002, **124**, 1192-1202.
65. M. V. Athawale, J. S. Dordick and S. Garde, *Biophys. J.*, 2005, **89**, 858-866.
66. L. Cordone, V. Izzo, G. Sgroi and S. L. Fornili, *Biopolymers*, 1979, **18**, 1965-1974.
67. G. Onori and A. Santucci, *J. Mol. Liq.*, 1996, **69**, 161-181.
68. G. N. Patey and S. Paul, *J. Phys. Chem. B*, 2006, **110**, 10514-10518.
69. S. L. Fornili, A. Fornili, M. Civera and M. Sironi, *PCCP*, 2003, **5**, 4905-4910.
70. C. Petersen, A. A. Bakulin, V. G. Pavelyev, M. S. Pshenichnikov and H. J. Bakker, *J. Chem. Phys.*, 2010, **133**, 164514.
71. R. Sinibaldi, C. Casieri, S. Melchionna, G. Onori, A. L. Segre, S. Viel, L. Mannina and F. De Luca, *J. Phys. Chem. B*, 2006, **110**, 8885-8892.
72. A. Laaksonen, P. G. Kusalik, A. P. Lyubartsev and D. L. Bergman, *J. Phys. Chem. B*, 2000, **104**, 9533-9539.
73. A. Di Michele, M. Freda, G. Onori and A. Santucci, *J. Phys. Chem. A*, 2004, **108**, 6145-6150.
74. A. Di Michele, M. Freda, G. Onori, M. Paolantoni, A. Santucci and P. Sassi, *J. Phys. Chem. B*, 2006, **110**, 21077-21085.
75. M. Freda, G. Onori and A. Santucci, *J. Mol. Struct.*, 2001, **565-566**, 153-157.
76. V. Calandrini, A. Deriu, G. Onori, R. E. Lechner and J. Pieper, *J. Chem. Phys.*, 2004, **120**, 4759-4767.

77. J. L. Finney, D. T. Bowron and A. K. Soper, *J. Phys. Chem. B*, 1998, **102**, 3551-3563.
78. D. T. Bowron, A. K. Soper and J. L. Finney, *J. Chem. Phys.*, 2001, **114**, 6203-6219.
79. D. S. Viswanath, *Viscosity of liquids:theory, estimation, experiment, and data*, Springer, 2006.
80. *Handbook of Chemistry and Physics*, CRC Press, 2004.
81. Y. Tominaga, T. Fukasawa and Y. Amo, *J. Chem. Phys.*, 2003, **118**, 6387-6393.
82. P. Sassi, M. Paolantoni, S. Perticaroli, F. Palombo and A. Morresi, *J. Raman Spectrosc.*, 2009, **40**, 1279-1283.
83. R. Biswas and H. A. R. Gazi, *J. Phys. Chem. A*, 2011, **115**, 2447-2455.
84. H. Tanaka, K. Nakanishi and H. Touhara, *J. Chem. Phys.*, 1984, **81**, 4065-4073.
85. T. M. Bender and R. Pecora, *J. Phys. Chem.*, 1986, **90**, 1700-1706.
86. D. T. Bowron and J. L. Finney, *J. Phys. Chem. B*, 2007, **111**, 9838-9852.
87. C. Petersen, K. J. Tielrooij and H. J. Bakker, *J. Chem. Phys.*, 2009, **130**, 214511.
88. K. Winkler, J. Lindner, H. Bursing and P. Vohringer, *J. Chem. Phys.*, 2000, **113**, 4674-4682.
89. J. L. Finney, D. T. Bowron, R. M. Daniel, P. Timmins and M. A. Roberts, *Biophys. Chem.*, 2003, **105**, 391-409.
90. R. Noto, V. Martorana, A. Emanuele and S. L. Fornili, *J Chem Soc Faraday T*, 1995, **91**, 3803-3808.
91. R. C. Dougherty, *J. Chem. Phys.*, 1998, **109**, 7372-7378.
92. H. J. Kim and B. D. Bursulaya, *J. Chem. Phys.*, 1999, **110**, 9656-9665.
93. J. Marti, J. A. Padro and E. Guardia, *J. Chem. Phys.*, 1996, **105**, 639-649.
94. G. E. Walrafen, M. R. Fisher, M. S. Hokmabadi and W. H. Yang, *J. Chem. Phys.*, 1986, **85**, 6970-6982.
95. M. S. Hokmabadi and G. E. Walrafen, *J. Chem. Phys.*, 1983, **78**, 5273-5274.

Chapter 5

Water Dynamics in Aqueous Solutions of Peptides

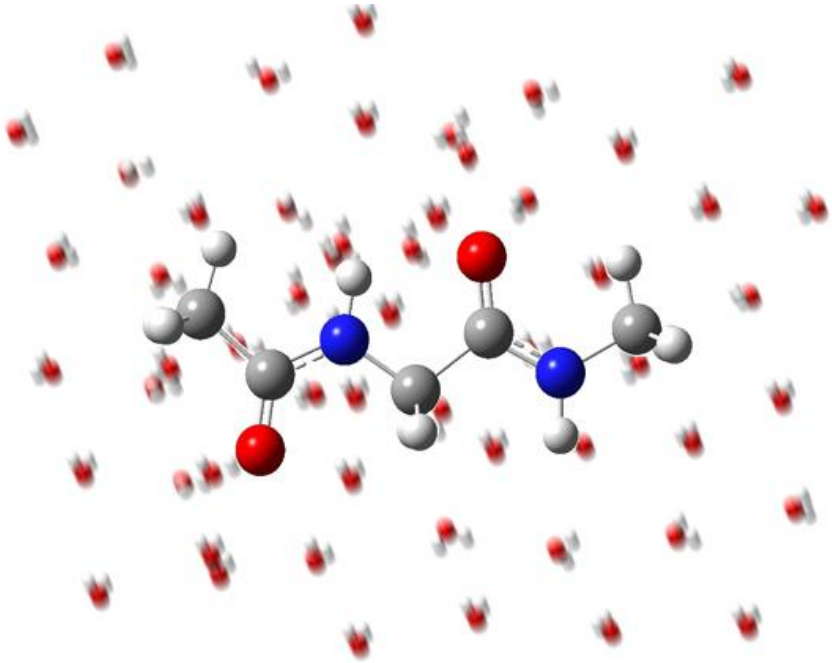

5.1 Introduction

To provide details about water dynamics around biological molecules three model peptides were studied in aqueous solutions: *N*-acetyl-glycine-methylamide ($C_5H_{10}N_2O_2$, NAGMA), N-acetyl-leucine-methylamide ($C_9H_{18}N_2O_2$, NALMA) and N-acetyl-alanine-methylamide ($C_6H_{12}N_2O_2$, NAAMA), Figure 5.1. These will provide an intermediate case between molecular solutions and proteins (chapter 6). The pair of di-peptides NAGMA and NALMA have been especially widely studied, as they are of similar sizes but NAGMA is hydrophilic whereas NALMA is amphiphilic, because it has a leucine residue as a hydrophobic site group. Experimental methods applied to these samples have included neutron scattering,[1-4] NMR relaxation,[5, 6] dielectric relaxation[7] and terahertz absorption spectroscopy.[8] These experimental studies have been recently complemented by detailed molecular dynamics simulations.[9, 10]

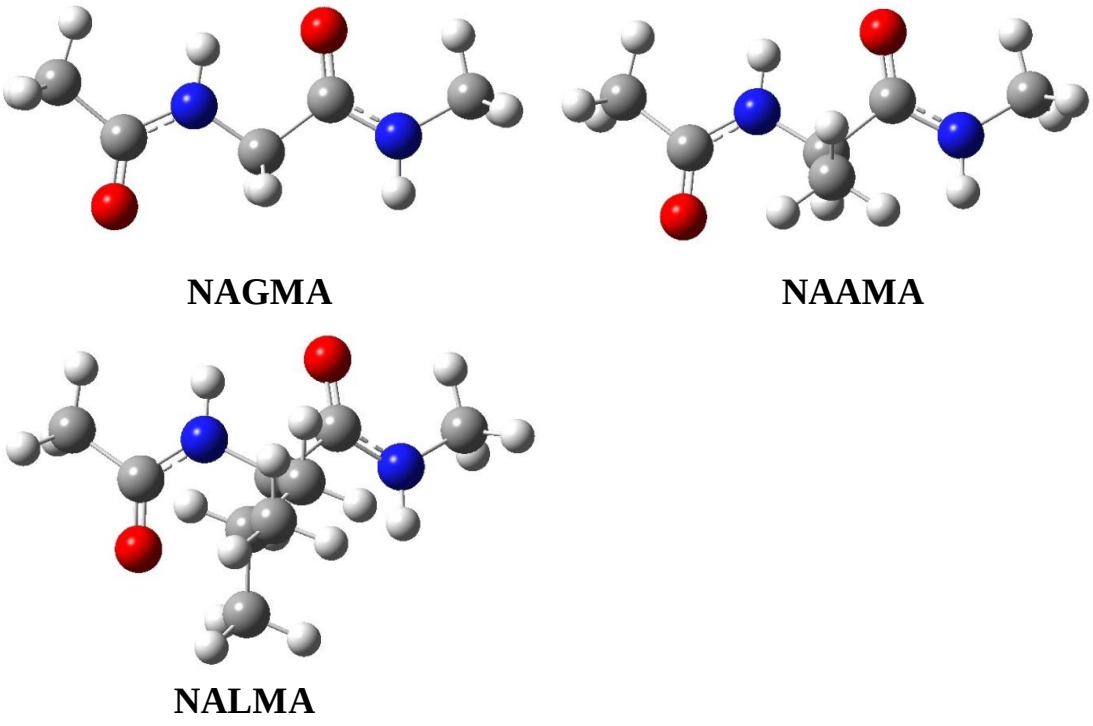

Figure 5.1 Optimized structures of NAGMA, NAAMA and NALMA.

In these diverse experiments, most studies report a population of water molecules in solutions of NAGMA and NALMA at around 295 K which relaxes on a timescale roughly twice as long as is found in pure water.[11] There is however a significant area of disagreement concerning the existence of a more slowly relaxing population. No such population is observed in NMR experiments.[6] In contrast, in neutron scattering[1] the existence of 'slow' water was reported with a relaxation time > 13 ps, corresponding to a retardation factor of ~10. Similarly, dielectric relaxation experiments recover relaxation dynamics on the time scale of tens of picoseconds, and a component as long as hundreds of picoseconds has been reported.[7] Quasi-elastic neutron scattering measurements[4] found the retardation factor smaller than 3.5 and depolarized light scattering measurements[12] estimated retardation factors between 7 and 9. These experiments were performed over a broad range of concentrations, depending on the sensitivity of the experiment. The concentrations used in NMR studies were kept below 0.2 M,[6] depolarized light scattering was investigated in the range 0.05 M - 0.6 M[12] and neutron scattering[1, 4] and dielectric relaxation[7] used samples between 0.5 M and 3 M. To provide a new perspective on these important systems we report here the dynamics of aqueous solutions of the three di-peptides NAGMA, NALMA and NAAMA as a function of concentration between 0.1 M and 3 M.

5.2 Picosecond Time Domain Analysis

The OKE data for aqueous solutions of peptides are shown in Figure 5.2 over the full range of concentration on the 0 – 4 ps timescale. The traces are normalized to the intense narrow Gaussian feature centred at t = 0 ps. For the first 200 fs the relaxation

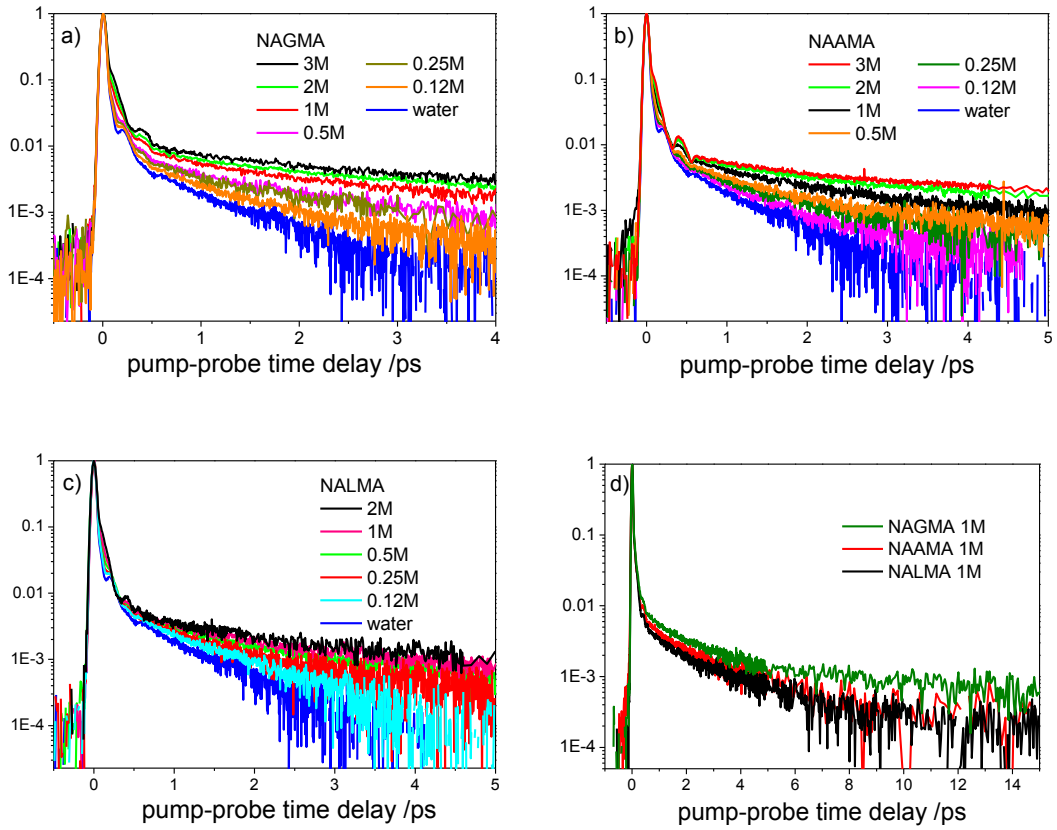

Figure 5.2 Short time window transient OHD-OKE data for a) NAGMA, b) NAAMA and c) NALMA. Pure water is plotted in blue for comparison. d) long time OKE response for 1M solutions of NAGMA, NAAMA and NALMA.

is characterised by a rapid decay which is oscillatory for both pure water and solutions of low (< 0.4 M) peptide concentration. At higher concentrations this oscillatory response is overdamped, *i.e.* the relaxation time is faster than the inverse of the oscillation frequency, so no oscillation is resolved. However at these high concentrations (above 0.4 M) a new oscillatory feature appears with a strong feature at ca 500 fs. Beyond 1 ps the relaxation is characterised by a monotonic but non-single exponential relaxation. As the concentration increases this picosecond relaxation time becomes longer, an effect that is particularly evident at concentrations above 1 M, where the slowest part of the relaxation has components of up to 20 ps.

The oscillatory features are best discussed in the frequency domain analysis (section 5.3). The picosecond dynamics will be discussed first.

The data for the three peptides were fitted from 600 fs up to the time at which the signal could not be distinguished from background. Both the bi-exponential and stretched exponential forms provided adequate fits to the data, but in all cases the stretched exponential (Eq. 2.32) yielded a better fit, as indicated by the reduced chi-square value. The fitting parameters recovered at selected concentrations are listed in

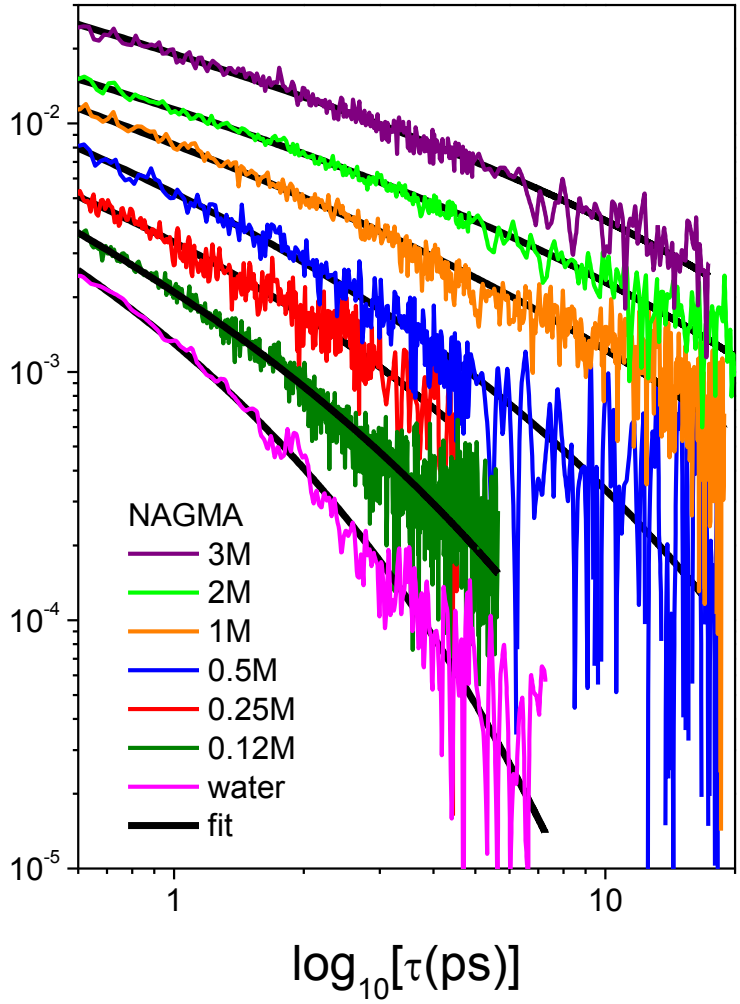

Figure 5.3 Diffusive reorientation component for NAGMA. The black lines are the stretched exponential fit.

Concentration /mol	NAGMA		NAAMA		NALMA	
	β	τ /ps	β	τ /ps	β	τ /ps
0.0	0.56	0.35	0.56	0.35	0.56	0.35
0.12	0.49	0.59	0.46	0.43	0.63	0.54
0.2	0.50	0.65	-	-	0.55	0.53
0.25	0.56	1.51	0.50	1.15	0.53	0.89
0.4	0.52	1.88	-	-	0.52	0.96
0.5	0.51	1.92	0.50	1.80	0.51	1.75
1	0.50	8.35	0.50	3.19	0.52	2.88
2	0.55	14.55	0.59	13.38	0.52	7.33
3	0.56	16.80	0.63	14.60	-	-

Table 5.1 Fit parameters of the time domain data obtained for NAGMA, NAAMA and NALMA. The 0 concentration denotes pure water. The starting point for all fits was 0.6 ps.

Table 5.1 and the quality of the fit is shown in Figure 5.3. No trend in β with concentration was observed, and for all peptides the β value was approximately constant with a mean value of 0.54. For subsequent analysis we report the mean relaxation time, defined in Eq. 2.33.

In Figure 5.4 the relaxation times for all three peptides are plotted as a function of molar ratio and (for NAGMA and NALMA) the dependence on solution viscosity is shown, where the viscosity is itself a function of concentration. These data show that for all three peptide solutions the structural reorganisation of the hydrogen bonded network reflected (section 2.4.3) in the OKE signal is slower than in pure water and two distinct concentration regions are found.

5.2.1 Low Concentration Region

Even without a quantitative analysis it is apparent in Figure 5.4c that the slowdown in structural reorganisation with increasing peptide concentration is a more significant effect for the hydrophilic NAGMA than for the amphiphilic NALMA, which persistently has the faster relaxation time. This is consistent with hydrophilic

interactions leading to slower structural dynamics in aqueous peptide solutions than hydrophobic interactions.[2, 3]

Significantly, in contrast to the observed relaxation time, NALMA causes a small but consistently greater increase in solution viscosity than NAGMA at the same concentration (Figure 5.4b). Although the contribution to the viscosity of peptide solutions are complex this result does confirm that the structural relaxation probed by OHD-OKE is not simply reflecting bulk viscosity in a way that might be predicted for orientational relaxation, through the Debye-Stokes-Einstein relation (Eq. 2.30). However estimation of rotational time for the NAGMA from Eq. 2.30 gave value of 66 ps. The NAGMA volume used for the calculation was obtained from DFT

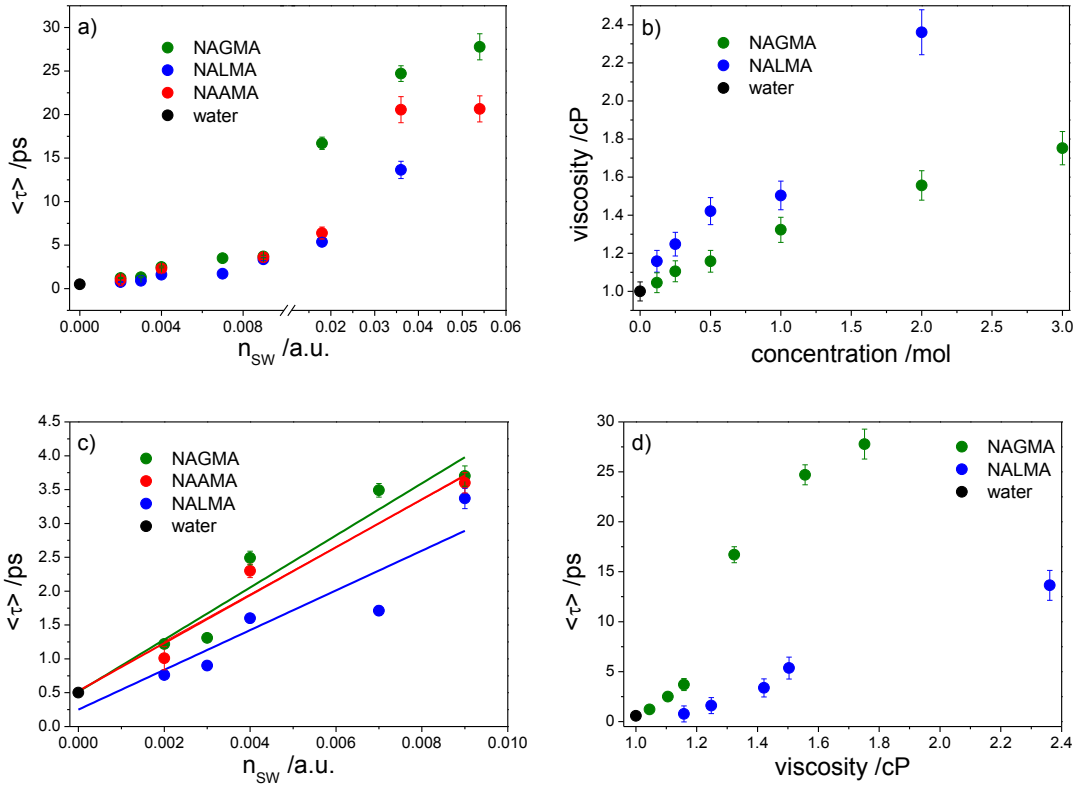

Figure 5.4 a) Dependence of <τ> on concentration for all three peptides.(b) solution viscosity as a function of concentration (c) fit to the two population analysis at low concentration and (d) the change in <τ> with viscosity.

calculations (158 $Å^3$). The calculated orientational time is as twice as long as the one observed for the highest NAGMA concentration. Therefore it is rather unlikely that at high concentration region, > 1M, pure peptide contributions are observed.

It is difficult to account for the dependence of solution viscosity on peptide concentration with any certainty, but the different behaviour of NALMA and NAGMA may simply reflect the greater volume fraction occupied by the former at any given concentration (*e.g.* 0.23 and 0.17 for NALMA and NAGMA, respectively at 2M concentration). Such behaviour would be consistent with the simple Einstein relation linking viscosity to a volume fraction of (non–interacting) spheres in solution (although it seems unlikely that the underlying assumptions of the Einstein relation will be met at the microscopic level by these aqueous peptide solutions).

To analyse quantitatively the effect of peptides on the picosecond structural dynamics in liquid water at low concentration (< 0.5 M) we adopt a two state model and apply it to the picosecond time scale OKE data as previously described in section 4.3. The linear fit to the low concentration data is shown in Figure 5.4c. The linear relation holds up to at least 0.007 molar ratio (0.4 M) and, significantly, the data extrapolate back to the relaxation time of bulk water. The number of water molecules in the first hydration shell was calculated using the procedure described in section 4.3. The values were 43, 38 and 32 (±2) for NALMA, NAAMA and NAGMA, respectively. In MD simulations NALMA and NAGMA were calculated to have 43 and 33 water molecules, respectively, in the first solvation shell, in good agreement with our calculations.[6] Knowing the hydration number and the slope (Figure 5.4c) the relaxation time of the water molecules in the first hydration shell was calculated to be 12.4 ± 0.5 ps for NAGMA, 9.7 ± 0.7 ps for NAAMA and 7.2 ± 0.5 ps for NALMA, thus giving retardation factors of 21, 17 and 12 for NAGMA, NAAMA and NALMA,

respectively. Again the result is consistent with a greater slowing down of the structural relaxation in water due to the hydrophilic solutes rather than the amphiphilic solute NALMA. This result is in turn qualitatively consistent with recent molecular dynamics studies of H-bonding lifetimes for amphiphilic solutes and for amino acids.[13, 14]

The relaxation times recovered from the analysis are significantly longer than those reported in NMR relaxation experiments. Since NMR and OHD-OKE probe quite different dynamics, a correspondence is not necessarily expected. However, two factors should be noted which might contribute to the recovery of an artificially long relaxation time from the two-state analysis of OKE signal. First, the long relaxation times are indicative of a strong effect of the peptide on the water relaxation dynamics even at low concentration. It is possible that at the very lowest concentrations the solute influences the observed structural reorganisation in water beyond the first solvation shell. In that case the relaxation time is overestimated (or, equivalently, n_S underestimated) in the two state analysis. Such long range effects of proteins and peptides on the structure and dynamics of solvation water have been reported on the basis of THz transmission spectra.[15] There is also evidence for peptide solvation layers extending beyond the first solvation shell in incoherent quasi-elastic neutron scattering.[1] If the second hydration shell was included in the two state analysis we estimate the relaxation time of water molecules around the peptide to be approximately 3.4 ps, 2.9 ps and 2.3 ps for NAGMA, NAAMA and NALMA, respectively. These yield retardation factors of approximately 6 (NAGMA), 5 (NAAMA) and 4 (NALMA). The recent study of NALMA aqueous solutions by depolarized light scattering[12] estimated retardation factor between 7 and 9 assuming that the number of water molecules affected by NALMA is 50-62 (temperature

dependent), therefore extending beyond the first hydration shell. If we reanalyze the present data using the same number of water molecules in the calculations (61) at a given temperature we obtain a retardation factor of ~9, which is in good agreement with the light scattering data. A second factor which may influence the estimated retardation factor is if the depolarised Raman cross section for the solvating water population is larger than for free water. This will tend to weight $<\tau>$ towards longer times, even if the solute effect on the dynamics is restricted to the first solvation shell. Additional experiments are required to separate these two possibilities.

5.2.2 Estimation of the Number of Water Molecules Exhibiting Slow Relaxation

We made an attempt to estimate the number of water molecules exhibiting slow relaxation by analysing the picosecond relaxation in more detail. The picosecond response of water was first fitted with a biexponential function given by Eq. 2.34. The values obtained for bulk water are listed in Table 4.1. To fit the picosecond response of the aqueous peptide solutions, the two exponentials obtained from the fit to pure

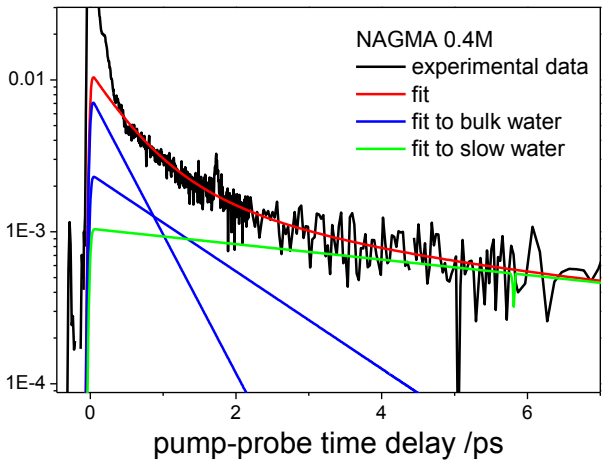

Figure 5.5 Fit with three exponentials to picoseconds response of NAGMA 0.4M. The blue exponentials are obtained from the bulk like water and green exponential is associated with slow water relaxation.

water were kept fixed and a third exponential which we associated with slow water was added, Figure 5.5. The number of water molecules responsible for the slow relaxation observed were calculated from the relationship:

$$n_m = \frac{I_m}{(I_B + I_m)X_P} \tag{5.1}$$

where I_m and I_B are the integrated areas of the exponentials associated with slow water and bulk water, respectively. X_P is a molar fraction of peptide/water solution. The results are plotted in Figure 5.6. It was calculated that with increasing concentration n_m decreases. However it has to be pointed out that at the lowest concentration studied a slight change in the fitting parameters results in a significant decrease or increase of n_m. Thus the error range at these low concentrations is large, so the precise number of water molecules affected by the solute is difficult to estimate from our measurements. However it is clear from Figure 5.6 that the most hydrophilic NAGMA affects the largest number of molecules and most hydrophobic NALMA the smallest number. This is again consistent with the hydrophilic solutes having the biggest effect on water dynamics in their vicinity.

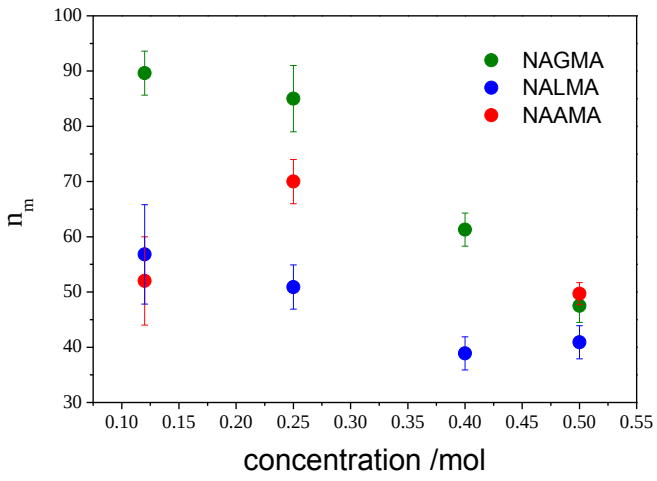

Figure 5.6 Number of water molecules exhibiting slow relaxation in the peptide aqueous solutions, calculated from Eq. 5.1.

5.2.3 High Concentration Region

Above 0.5 M the effect of increasing concentration is more marked, and the relaxation slows dramatically, such that for 3 M NAGMA the measured relaxation is up to 40 times slower than in bulk water. However, at these very high concentrations relaxation processes associated with the peptide may also contribute to the OKE response. At peptide concentrations above 0.5 M the measured relaxation time slows appreciably and the data no longer extrapolate to the bulk water relaxation time. This slowdown occurs when the number of solvent molecules is sufficient for at most two complete solvation shells, and, at the highest peptide concentrations, there is less than one complete solvation shell per solute. The extended relaxation time observed here is also consistent with the strong nonlinear concentration dependence reported in THz transmission spectroscopy,[15] and with observations of slow dynamics in dielectric relaxation at high concentrations.[7]

At the higher peptide concentration both the solute and the solvent can contribute to the measured OKE signal. The solute could in principle contribute a slow component due to orientational relaxation. However, the degree of pump induced alignment of a relatively massive peptide molecule will be small for the low intensity pulses used here, making it likely that any such effect is more than a minor component of the relaxation. In the constant electric field, the larger moment of inertia of the molecule the more difficult is to align with the electric field. Very low frequency intramolecular modes of the peptide (such as torsional reorganisation) may also contribute to the observed relaxation, but such modes will themselves be strongly coupled to the solvent dynamics, since they reflect the solvent friction,[16] and solvent molecules must reorganise to accommodate them. Finally the crowding of the solvation layer between adjacent solute molecules can itself contribute to a slowing down of structural

reorganization within the solvating water molecules. One such mechanism has been highlighted in the simulations of Hynes, Laage and co-workers[14] and was already discussed in chapter 4 regarding amphiphilic solutes. The appearance of such a restricted geometry at high solute concentration is expected to correlate with the attenuation of the signal due to tetrahedral structure in water seen in the Im $D'(\omega)$, as discussed below. The effect of solute on the water dynamics is expected to be the largest when effectively all molecules are in the solvation shell.

5.3 Frequency Domain Analysis

The evolution of the low frequency spectral density with increasing peptide concentration is shown in Figure 5.7. In Figure 5.8 the frequencies, and relative weights of the Bucaro-Litovitz, antisymmetrized Gaussian and Gaussian components (section 2.4.2) fit to the Im $D'(\omega)$ are shown for all three peptides studied. The fit parameters are shown in Table 5.2.

The spectral densities were fitted with two functions: Bucaro-Litovitz and antisymmetrized Gaussian. At concentrations below 0.4M the most significant effect of increasing peptide concentration is a small decrease in the relative amplitude of the higher frequency H-bond stretching mode (Figs 5.8b). This is consistent with a minor change in the distribution of H-bonds. These data suggest that the overall tetrahedral structure of water is largely maintained at these low concentrations, where there are in excess of 100 water molecules per peptide.

Above 0.4 M a third function was needed to accurately fit the spectra (Gaussian), Figure 5.7d. As the peptide concentration increases beyond 0.4 M there is also a more

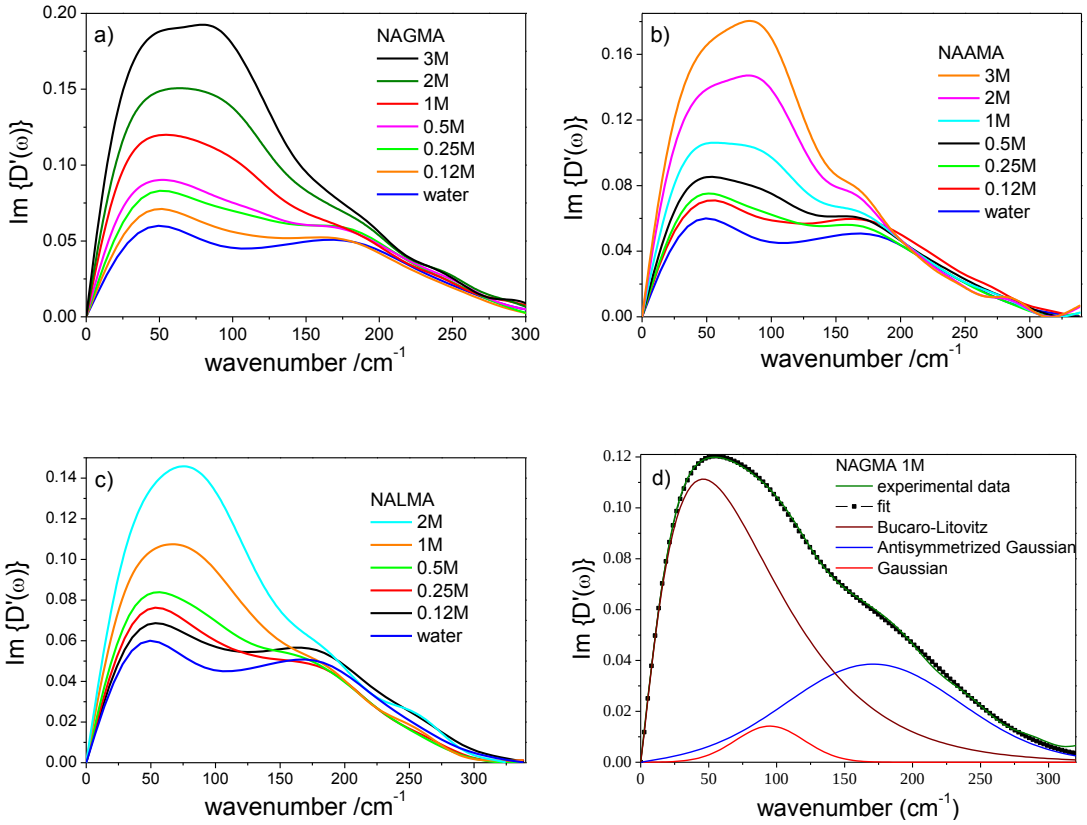

Figure 5.7 Im *D'(ω) for a) NAGMA, b) NAAMA and c) NALMA solutions. The spectrum of pure water is plotted in blue as a reference. d) is a quality of fit to RSD of 1M NAGMA.*

marked change in the Im $D'(\omega)$ (Figure 5.7 and 5.8). Essentially the bi-modal profile collapses to an asymmetric band with a reduced mean frequency. This is accompanied by a decrease in the relative weight of the integrated area of ASG mode. Qualitatively this indicates the disruption of tetrahedral water structure at high peptide concentration (0.4M NAGMA corresponds to two solvation shells per solute). The increase in the intensity of Im *D'(ω)* at the low peptide concentration is associated with the change of distribution of H-bonds in the solution.

Quantitative analysis (Figure 5.8) shows that the main changes in Im *D'(ω)* are a decrease in both the relative weight and the frequency of I_{ASG}, consistent with

disruption of the H-bond structure, and a growth in amplitude of the intermediate Gaussian mode at *ca* 90 cm^{-1} (which has a zero weight at concentrations below 0.4

conc. /mol	A_{BL}	α	ω_{BL} /cm^{-1}	A_G	ω_G /cm^{-1}	$\Delta\omega_G$ /cm^{-1}	A_{ASG}	ω_{ASG} /cm^{-1}	$\Delta\omega_{ASG}$ /cm^{-1}
NAGMA									
0.12	0.001	1.2	40.1	-	-	-	0.035	182.1	118.5
0.2	0.001	1.2	41.0				0.039	180.0	122.0
0.25	0.001	1.2	41.4	-	-	-	0.038	182.0	122.6
0.4	0.001	1.2	40.0	0.002	95.0	40.0	0.037	179.4	129.0
0.5	0.002	1.2	39.7	0.003	95.0	48.7	0.039	179.6	134.7
1	0.003	1.1	38.7	0.014	95.0	59.3	0.038	171.0	150.0
2	0.004	1.1	38.5	0.028	96.1	61.1	0.045	167.7	150.0
3	0.006	1.1	36.23	0.050	95.9	62.1	0.051	157.8	156.4
NAAMA									
0.12	0.001	1.3	36.1	-	-	-	0.046	179.1	125.9
0.25	0.001	1.3	36.5	-	-	-	0.042	178.5	119.2
0.5	0.001	1.3	36.0	0.009	94.2	44.0	0.045	177.0	122.0
1	0.001	1.3	35.7	0.014	95.2	44.6	0.042	175.6	125.1
2	0.002	1.3	34.6	0.033	95.9	46.8	0.040	160.9	125.9
3	0.002	1.3	34.5	0.049	95.9	50.8	0.040	157.6	134.9
NALMA									
0.12	0.0005	1.6	31.0	-	-	-	0.046	182.0	129.9
0.2	0.0006	1.6	31.0				0.038	176.0	128.0
0.25	0.0005	1.6	31.0	-	-	-	0.037	176.4	128.0
0.4	0.0008	1.5	32.0	0.004	86.0	30.0	0.038	173.2	128.0
0.5	0.0008	1.5	31.0	0.005	86.7	49.7	0.039	167.8	136.0
1	0.0009	1.5	31.0	0.017	90.0	56.6	0.040	165.0	142.1
2	0.001	1.4	29.9	0.050	91.0	70.0	0.042	162.9	156.3

Table 5.2 Fit parameters of Fourier Transform Kerr Spectra of NAGMA, NAAMA and NALMA (top, middle and bottom, respectively). BL denotes Bucaro-Litovitz, G Gaussian and ASG antisymmetrized Gaussian.

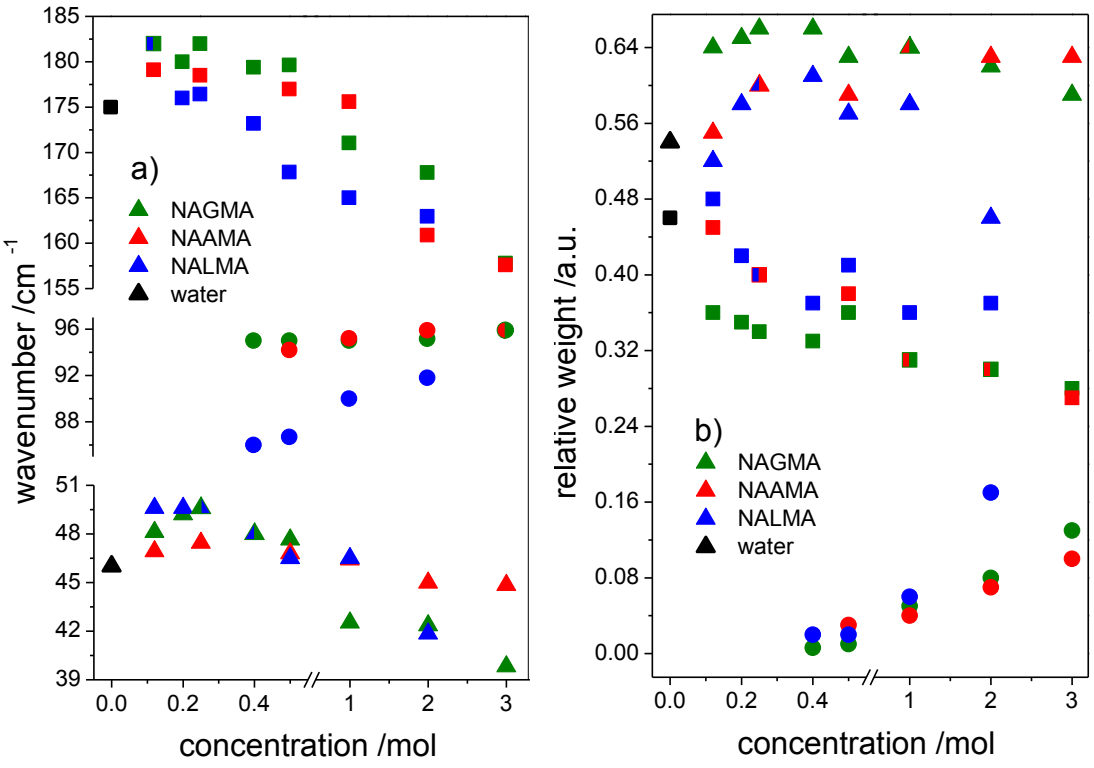

Figure 5.8 a) wavenumber and b) relative weight of spectral components fitted to NAGMA, NAAMA, NALMA and water Im *D'(ω). Squares, dots and triangles denote anisymmetrized Gaussian, Gaussian and Bucaro-Litovitz, respectively. Error ±5 %*

M). There are only small changes in the frequency and relative weight of the low frequency I_{BL} line shape function. The behaviour is quite similar for all three peptides studied. However, the changes in I_{ASG} occur at a slightly lower mole fraction for the amphiphilic NALMA than for NAGMA and NAAMA, Figure 5.8. This may reflect the greater physical size of NALMA, causing it to perturb more water molecules than the smaller peptides. The spectral density evolution observed for peptides resembles that of UA, FA and TMU (chapter 4) where no change in the frequencies of the BL and ASG components were also found.

At 1 M there are only just sufficient water molecules to provide one complete solvation shell for NALMA. Consequently, water molecules which have a peptide as

nearest neighbour are on average more likely to be H-bonded to a water molecule surrounding another (or the same) peptide, rather than to a 'bulk' water molecule. Thus, a plausible interpretation of the data in Figure 5.8 is that the absence of such bulk water molecules at higher concentrations leads to a significant change in the ability of water molecules to occupy the tetrahedral sites characteristic of pure water (and lower peptide concentrations).

The 90 cm^{-1} mode fit by the Gaussian component corresponds to the 500 fs oscillation in the OKE response observed at higher peptide concentrations (Figure 5.2). Its growth in amplitude as a linear function of concentration suggests an assignment to a peptide mode (Figure 5.8). A similar mode has been widely reported in OHD-OKE and low frequency Raman scattering studies of a range of peptides, amides and proteins and UA and FA (chapter 4).[17-19] Therefore for this mode to appear the molecule has to consists of O-C-N-H unit. The linear dependence (over the limited concentration range studied) suggests a mode associated with a peptide monomer. There is convincing evidence for the existence of cyclic dimers and chain like aggregates for model peptides[20] in aqueous solution, and these may support low frequency modes. However, such aggregates cannot be formed by NALMA for steric reasons, yet the mode is certainly not suppressed (Figure 5.8). Consequently, this mode is more likely to be associated with a solvated peptide monomer.

To investigate further the origin of this Gaussian mode we performed DFT calculations on the peptides NAGMA and NAAMA, with one or two added water molecules (the results for NAGMA are summarized in Figure 5.9). The DFT calculations on di-peptides revealed a number of low frequency modes, but did not detect any specific intense Raman active mode around 90 - 100 cm^{-1}. One or two added water molecules significantly perturbed and enhanced the calculated

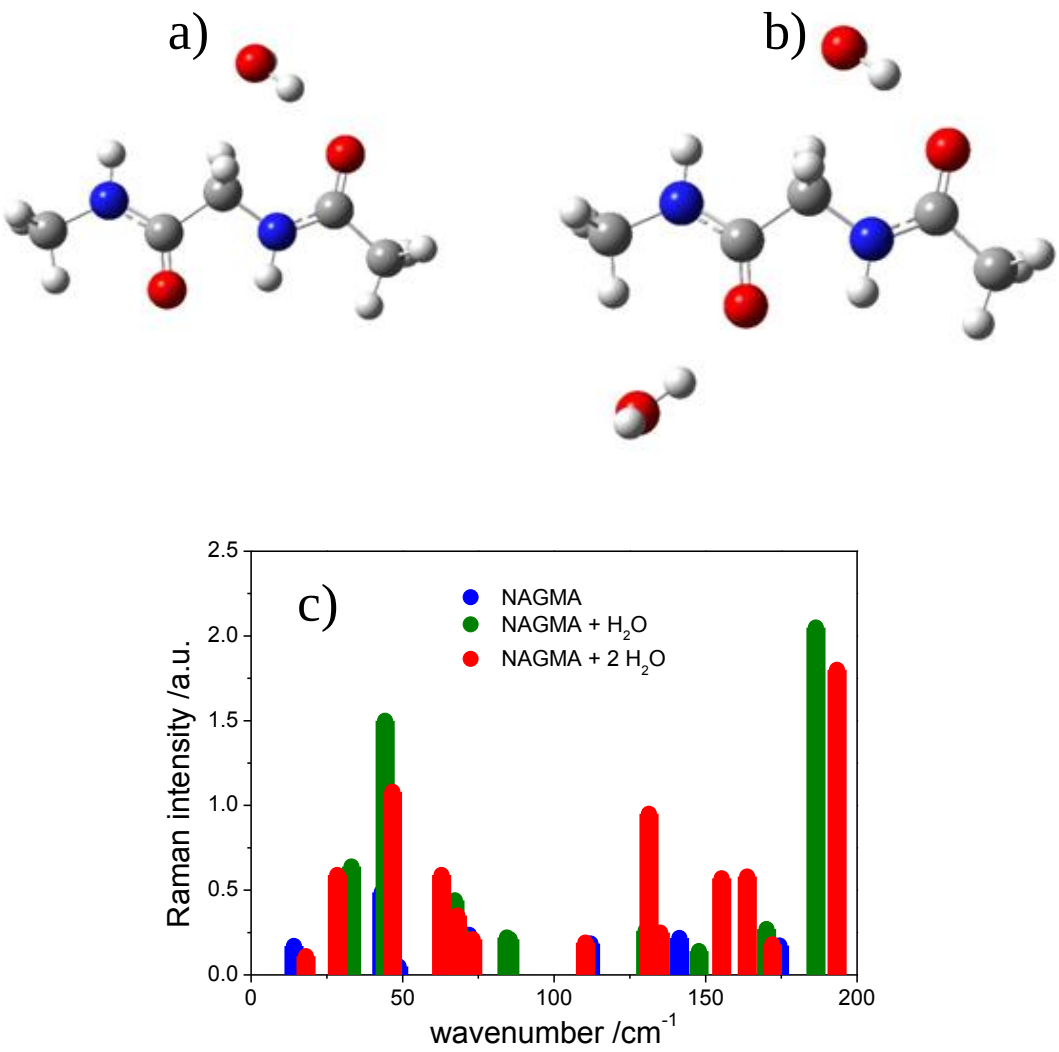

Figure 5.9 Optimized structures of NAGMA and a) one water molecules and b) two water molecules. c) calculated frequencies from DFT. Anisotropic Raman intensities were calculated using Eq. 3.3.

low frequency Raman spectra, as was reported previously,[21] but again no unique mode was observed to which the 90 cm^{-1} component could be assigned. Therefore by analogy to the UA and FA studies (chapter 4) we associate the Gaussian component with vibrational motion in an H-bonded solvated peptide. Although the present data do not allow a definitive assignment, all of the plausible assignments support an intermolecular origin and a role for solvent – solute H-bonded interactions.

5.4 Conclusions

The anisotropic polarizability response of three model peptides was studied through OKE spectroscopy. The experiments revealed two distinct concentration regimes. At concentrations below 0.4 M, where on average less than 40% of water molecules have a peptide as nearest neighbour, the tetrahedral structure of water is largely preserved. The measured relaxation times in the peptide solution are slower than in bulk water at these low peptide concentrations, and increase linearly up to a concentration of 0.4 M. Slower dynamics are observed for the more hydrophilic peptides. The current measurements cannot unambiguously deconvolute the observed relaxation time from the number of solvating water molecules involved. However the large retardation factor calculated for one hydration shell of a solute suggests that peptides influence the water dynamics beyond the first hydration shell. At higher peptide concentrations the tetrahedral water structure is perturbed and the measured dynamics are up to 40 times slower than in bulk water. In this case the observed dynamics are not a property of the water alone, but reflect relaxation in the H-bonded network of solvated peptide molecules. This change in the nature of the relaxation mechanism highlights the importance of concentration dependent experiments when measuring relaxations in aqueous peptide solutions, such as neutron diffraction, NMR or dynamic light scattering.

5.5 References

1. D. Russo, R. K. Murarka, J. R. D. Copley and T. Head-Gordon, *J. Phys. Chem. B*, 2005, **109**, 12966-12975.
2. D. Russo, G. Hura and T. Head-Gordon, *Biophys. J.*, 2004, **86**, 1852-1862.
3. D. Russo, R. K. Murarka, G. Hura, E. Verschell, J. R. A. Copley and T. Head-Gordon, *J. Phys. Chem. B*, 2004, **108**, 19885-19893.
4. C. Malardier-Jugroot, M. E. Johnson, R. K. Murarka and T. Head-Gordon, *PCCP*, 2008, **10**, 4903-4908.

5. J. Qvist and B. Halle, *J. Am. Chem. Soc.*, 2008, **130**, 10345-10353.
6. J. Qvist, E. Persson, C. Mattea and B. Halle, *Faraday Discuss.*, 2009, **141**, 131-144.
7. R. K. Murarka and T. Head-Gordon, *J. Phys. Chem. B*, 2008, **112**, 179-186.
8. B. Born, H. Weingartner, E. Brundermann and M. Havenith, *J. Am. Chem. Soc.*, 2009, **131**, 3752-3755.
9. M. E. Johnson, C. Malardier-Jugroot, R. K. Murarka and T. Head-Gordon, *J. Phys. Chem. B*, 2009, **113**, 4082-4092.
10. M. E. Johnson, C. Malardier-Jugroot and T. Head-Gordon, *Phys Chem Chem Phys*, 2010, **12**, 393-405.
11. B. Halle, *Philosophical Transactions of the Royal Society of London Series B-Biological Sciences*, 2004, **359**, 1207-1223.
12. S. Perticaroli, L. Comez, M. Paolantoni, P. Sassi, A. Morresi and D. Fioretto, *J. Am. Chem. Soc.*, 2011, **133**, 12063-12068.
13. F. Sterpone, G. Stirnemann, J. T. Hynes and D. Laage, *J. Phys. Chem. B*, 2010, **114**, 2083-2089.
14. G. Stirnemann, J. T. Hynes and D. Laage, *J. Phys. Chem. B*, 2010, **114**, 3052-3059.
15. U. Heugen, G. Schwaab, E. Brundermann, M. Heyden, X. Yu, D. M. Leitner and M. Havenith, *P. Natl. Acad. Sci. USA*, 2006, **103**, 12301-12306.
16. N. T. Hunt and S. R. Meech, *Chem. Phys. Lett.*, 2003, **378**, 195-201.
17. Y. J. Chang and E. W. Castner, *J. Chem. Phys.*, 1993, **99**, 113-125.
18. S. E. M. Colaianni and O. F. Nielsen, *J. Mol. Struct.*, 1995, **347**, 267-283.
19. G. Giraud, J. Karolin and K. Wynne, *Biophys. J.*, 2003, **85**, 1903-1913.
20. O. F. Nielsen, *Annual Reports Section C: Physical Chemistry*, 1997, **93**, 57-100.
21. H. Shirota and H. Ushiyama, *J. Phys. Chem. B*, 2008, **112**, 13542-13551.

Chapter 6

Water Dynamics in Aqueous Solutions of Proteins

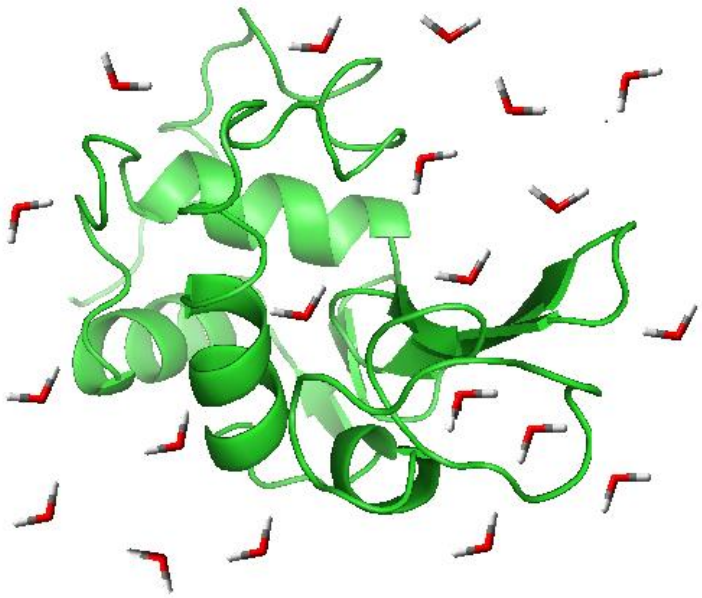

6.1 Introduction

The behaviour of water molecules surrounding a protein can have an important bearing on its structure and function. Consequently, a great deal of attention has been focussed on changes in the relaxation dynamics of water when it is located at the protein-water interface. To gain an insight to the dynamics of aqueous protein solutions, we present an ultrafast OKE study of a series of solutions of globular proteins.

Water molecules in aqueous solutions of proteins can generally be grouped into three broad categories: (1) the internal water which occupies specific sites in the protein and can be identified crystallographically (2) the hydration water immediately surrounding the protein and (3) bulk like water. Hydration water has a direct contact with the protein surface and plays an essential role in protein folding. For example, where the interaction of water with the hydrophobic residues causes them to collapse and become isolated in the protein core. Thus the protein core typically contains more than 80% of the hydrophobic side chains.[1] The water molecules which solvate the external surface of a folded protein are also functionally significant; it has been found that to fully activate the dynamics and functionality of a protein 0.40 grams of water per gram of protein are required.[2] Because of this importance, hydration layers surrounding peptides,[3-5] proteins[6-8] and carbohydrates[9] have been the subject of a large number of studies in recent years. It is established that the dynamics of hydration water are distinct from those of bulk water,[10] however the nature and extent of these differences remain a matter of debate.[6] Molecular dynamics (MD) simulations[11] and NMR studies[12] showed that the H-bonds between protein and water are preferentially formed with the water hydrogen atoms acting as donors. The

number of H-bonds was found to depend strongly on the polar character of the protein surface. MD simulations suggested that the rearrangement of the protein hydration network occurs at subpicosecond to picosecond time scales.[13] This view was consistent with NMR data which found a highly mobile protein solvation layer, in which water molecules are retarded by no more than a factor of two compared to the bulk.[7] Single frequency THz transmission spectroscopy has also been applied to the study of the hydration water of peptides[5] and proteins.[14, 15] This approach suggested that a dynamical solvation layer could extend considerably beyond the monolayer suggested by static experiments. It was suggested that this method was also sensitive to the effect of the folded state of the protein on solvation structure.[16]

6.2 Time Domain Analysis

The OKE response of aqueous solutions of lysozyme, trypsin and BSA were studied over a wide range of concentrations. The time domain data are shown in Figure 6.1. It is evident that for all of the solutions studied the picosecond relaxation dynamics become slower with increasing concentration, and the departure from single exponential relaxation becomes more marked compared to pure water. The OKE traces of protein solutions at low concentrations (< 5 wt. %) are characterized by an oscillatory relaxation on the subpicosecond time scale, characteristic of pure water. With increasing solute concentration a new oscillation appears with a predominant feature at ~ 500 fs, the amplitude of which increases with increasing protein concentration. This oscillation was previously observed in studies of aqueous solutions of urea and formamide (chapter 4) and peptides (chapter 5) and assigned to an out of plane bending mode of the H-bonded solute.

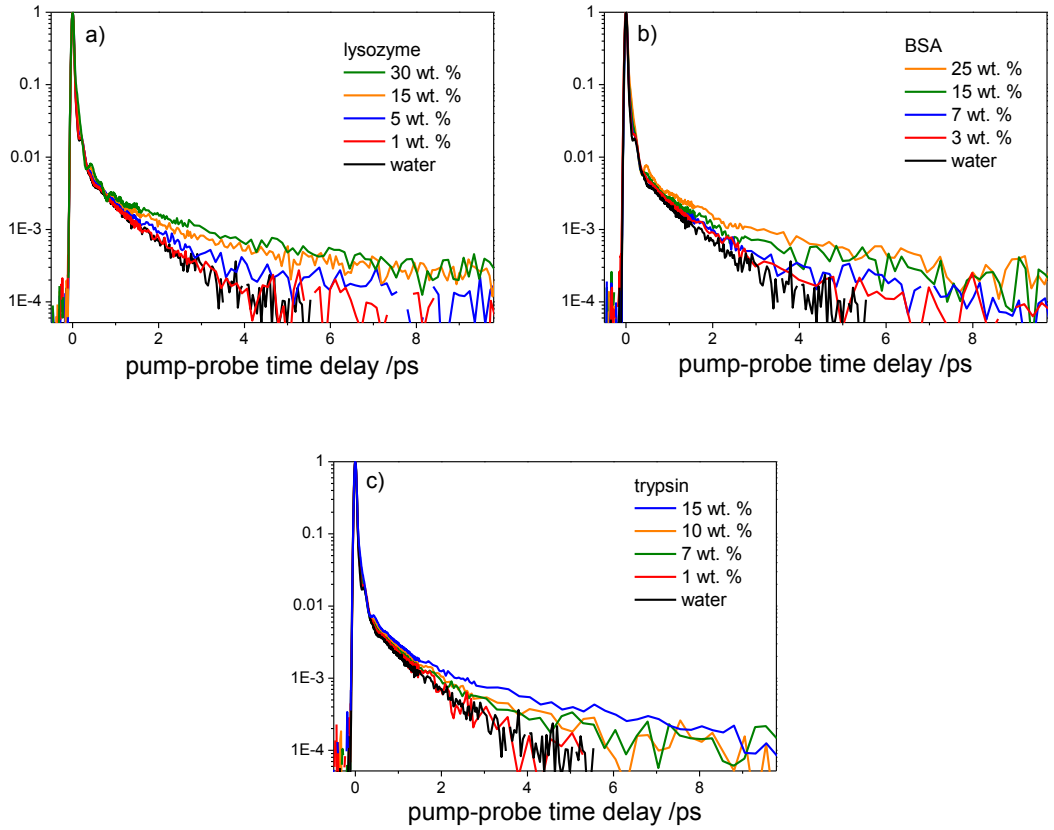

Figure 6.1 OKE-OHD signals for three proteins as a function of their wt% a) lysozyme b) BSA and c) trypsin. Water is plotted in black for reference.

6.2.1 Picosecond Analysis

The picosecond response was fitted with the biexponential function given by Eq. 2.34, with a starting point for the fit at 1 ps. During the measurement it was observed that the signal for the solutions with high concentration of protein did not return to the baseline even after 10 ps. In cases where the protein concentration exceed 7 wt.% a small offset (0.00005) had to be included in the fit to account for this effect giving a better quality fit. The origin of this offset was not investigated further, but may reflect a slow relaxation associated with the protein solute, since at these higher

concentrations protein modes also contribute to the RSD (see below). For example, protein side chain motions may contribute a small amplitude to the observed response.

Parameters obtained from the biexponential fit, listed in Table 6.1, were used to calculate the averaged relaxation time, $<\tau>$, Eq. 2.35. The average relaxation times are plotted as a function of the molar ratio, n_{SW} (moles of solute divided by moles of water) in Figure 6.2.

At the concentrations studied it is unlikely that the protein itself contributes anything other than the constant offset described above to the relaxation times observed. The rotational correlation time of lysozyme and BSA obtained through NMR are 18 ns and

concentration / wt. %	a_1	τ_1 /ps	a_2	τ_2 /ps	$<\tau>$/ps
BSA					
1	0.72	0.42	0.28	1.35	0.68
3	0.70	0.42	0.30	1.46	0.73
5	0.80	0.53	0.20	2.04	0.83
7	0.74	0.50	0.26	1.72	0.81
10	0.85	0.67	0.15	3.08	1.04
15	0.92	0.81	0.08	5.31	1.22
20	0.84	0.72	0.16	4.29	1.25
25	0.83	0.82	0.17	4.29	1.41
lysozyme					
1	0.76	0.46	0.24	1.43	0.69
3	0.73	0.45	0.27	1.47	0.72
5	0.85	0.64	0.15	2.51	0.98
7	0.88	0.68	0.12	3.08	0.97
10	0.86	0.85	0.14	3.73	1.25
15	0.83	0.83	0.17	5.32	1.54
20	0.82	0.65	0.18	4.90	1.37
25	0.84	0.88	0.16	5.98	1.75
30	0.80	1.13	0.20	6.01	2.10
trypsin					
1	0.80	0.47	0.20	1.31	0.70
5	0.71	0.66	0.29	1.54	0.89
7	0.71	0.46	0.29	1.49	0.93
10	0.78	0.64	0.22	1.95	0.94
15	0.84	0.58	0.16	3.39	1.10

Table 6.1 Fitting parameters to the Eq.2.34

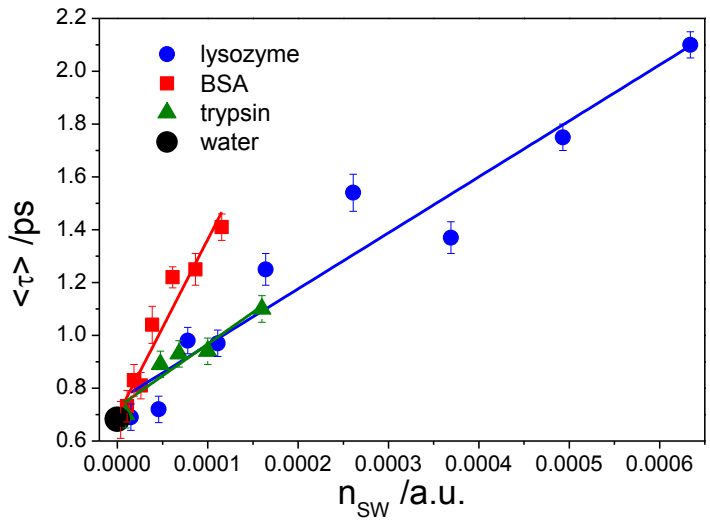

Figure 6.2 Average relaxation time plotted against molar ratio. Solid lines are linear fits to the data.

105 ns, respectively.[17] These values are on a much longer timescale than that probed in the present OHD-OKE experiments. A linear fit to the relaxation times plotted as a function of concentration extrapolates back to the bulk water value. Therefore we assign the observed concentration dependence of the mean relaxation time to the effect of the protein on the dynamics of the water. Tokmakoff *et al.*[18] studied hydrated protein films with OKE spectroscopy and also did not observe any reorientation of protein molecules or any contributions coming from the amino acids. OKE studies of simple peptides (chapter 5) showed that peptides are expected to contribute to the OKE signal on the > 10 ps time scale. Such long relaxation times were not observed in proteins studies. As mentioned earlier, measurements obtained by the OHD-OKE technique do not allow the separate measurement of hydration water and free water so we again employ the two state model to estimate the relaxation time of the hydration shell as described in section 4.3.

Knowing that the proteins studied have roughly spherical shapes (globular proteins), the volumes could be calculated using the radii of 15.9, 18.7, 27.1 Å for lysozyme, trypsin, and BSA, respectively.[19] With this information, the number of water molecules in each hydration shell could be calculated as described in section 4.3. For the first hydration shell, the n_m values obtained were 490, 668 and 1385 for lysozyme, trypsin and BSA, respectively. These values are in good agreement with published data: 436-700 for lysozyme[20-22] 1422 for BSA[23] obtained from molecular dynamics simulations and dielectric measurements. Using the calculated n_m data and the slope, $n_m(\tau_{WH} - \tau_{WF})$, the hydration water relaxation times were estimated.

Firstly, under the assumption that only water dynamics in the first hydration shell are affected by the protein molecules, we estimated the hydration water relaxation times to be 5.5 ps, 5 ps and 4.1 ps for BSA, lysozyme and trypsin respectively. As the relaxation of pure water is ~0.7 ps, the estimated relaxation times correspond to factors of 8.0 (BSA), 7.3 (lysozyme) and 6.1 (± 0.3) (trypsin) times slower than for bulk water. The retardation factor for the reorientational dynamics of water in the protein hydration shells was studied previously.[7, 20, 24] For example, from magnetic relaxation dispersion[7] studies the water retardation factor was found to be 2; from depolarized light scattering (DLS)[24] measurements it was suggested to vary between 6 and 7. Although OHD-OKE accesses translational dynamics (as do DLS), the retardation factor of ~7 is of the same order as these results, though clearly longer than the data obtained from magnetic relaxation measurements. This similarity may indicate that translational and orientational dynamics are correlated, perhaps because both are dominated by the dynamics of the water H-bonded network. This correlation is supported by MD simulations of solvated lysozyme[20] where it was found that the rotational relaxation of water at the protein surface presents the same retardation value

as does translational diffusion. This factor was calculated to be 3 to 7 times slower than in the bulk, with the ratio depending on how the hydration shell was defined prior to calculation.

Next we try to connect the observed relaxation times for the different proteins with their surface hydrophobicity. Protein hydrophobicity was extensively studied in the past using a number of approaches, including hydrophobic interaction chromatography,[25, 26] fluorescence spectroscopy,[27] and osmotic pressure measurements.[28] Lee and Richards[29] estimated the surface hydrophobicity of lysozyme from numerical calculations of the solvent accessible area. They found that lysozyme has an approximately 41% hydrophobic surface. The surface of BSA, was studied through both osmotic pressure measurements and hydrophobic interaction chromatography.[28] It was found to have a significantly more hydrophilic surface than that of lysozyme. Wettability and contact angle analysis[30] of lysozyme and trypsin films indicated trypsin as the protein with the most hydrophobic surface. Therefore on the basis of these measurements, the surface hydrophobicity of the proteins studied can be written in the order trypsin > lysozyme > BSA, with BSA being the most hydrophilic.

Our previous OKE studies of peptides[4] and small solutes[31] found that hydrophilic groups caused a larger retardation of the dynamics of the hydration shell than hydrophobic groups. In this work we also find the largest retardation factor (8.0) for the protein with the most hydrophilic surface (BSA) and the smallest retardation factor (6.1) for the most hydrophobic (trypsin). This is again consistent with the hydrophilic interaction having the greatest retardation effect on the dynamics of the solvating water molecules.

A further factor to be considered is the possibility that water dynamics in a second hydration shell are also affected by the protein. If a second shell is included, the calculated retardation factor will be smaller, yielding values of 4.1, 3.5, 3.1 (±0.2) for BSA, lysozyme and trypsin, respectively. The smaller difference in the retardation factor between different proteins indicates that water relaxation dynamics in the second hydration shell is similar in all proteins studied, regardless of their hydrophobicity. Water molecules in the second hydration shell do not have direct contact with the protein surface, and are therefore not strongly affected by the nature of the surface. We also estimated the number of water molecules affected by each protein, using the analysis described in section 5.2.2. Figure 6.3 represents the number of water molecules exhibiting slow dynamics recovered for lysozyme.

Similarly, as in the case of peptides, the solutions with low concentration are characterized by a broad error range. The number of slow water molecules ranges from 800 to 2750. This would indicate that 2-3 hydration shells of lysozyme exhibit slower dynamics. The same analysis of the aqueous solution of BSA and trypsin also indicate that the effect of the protein on the water dynamics extends to water molecules beyond the second hydration shell (data not shown). The same analysis for aqueous solutions of BSA and trypsin also indicates that the protein retards the dynamics of water molecules in the second and third hydration shell.

Finally we consider the relationship between the macroscopic solution viscosity and the observed picosecond relaxation dynamics. The viscosities of the three protein solutions were measured as a function of concentration and the average relaxation time, $<\tau>$, is plotted against viscosity (Figure 6.4a). The viscosity of trypsin was

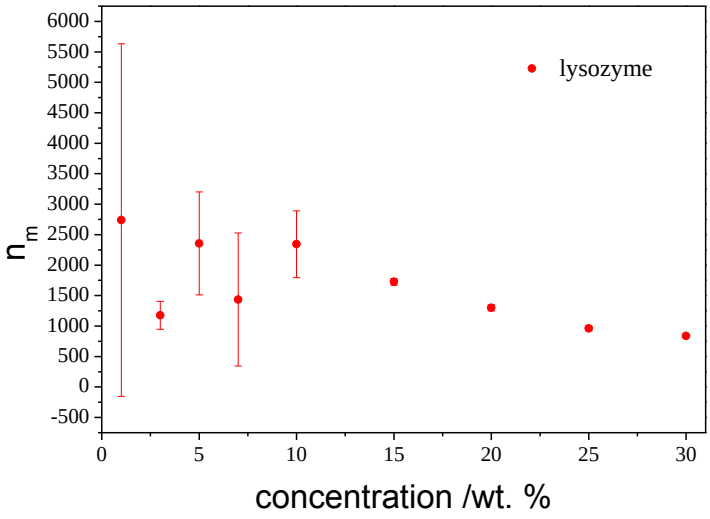

Figure 6.3 Number of water molecules exhibiting slow relaxation in the lysozyme aqueous solutions.

found to be the largest among the proteins studied (Figure 6.4b); at 15 wt. % its viscosity is approximately nine times higher than for BSA solution and twelve times that of lysozyme. However this large viscosity is not reflected in the relaxation times measured in OHD-OKE, since trypsin in fact has the fastest average relaxation time(Figure 6.4a). From these data we can conclude that the macroscopic solution viscosity is not correlated with the observed relaxation times. The relaxation times we observe arise from microscopic intermolecular interactions while the macroscopic viscosity presumably reflects the slower dynamics in the concentrated protein solutions.

The much higher viscosity observed for trypsin might indicate aggregation of trypsin at these high concentrations. If trypsin aggregates there is much more bulk like water, which might be reflected in the fastest relaxation studied. However, in that case it would be expected that the relaxation time depends nonlinearly on concentration and this is not the case here.

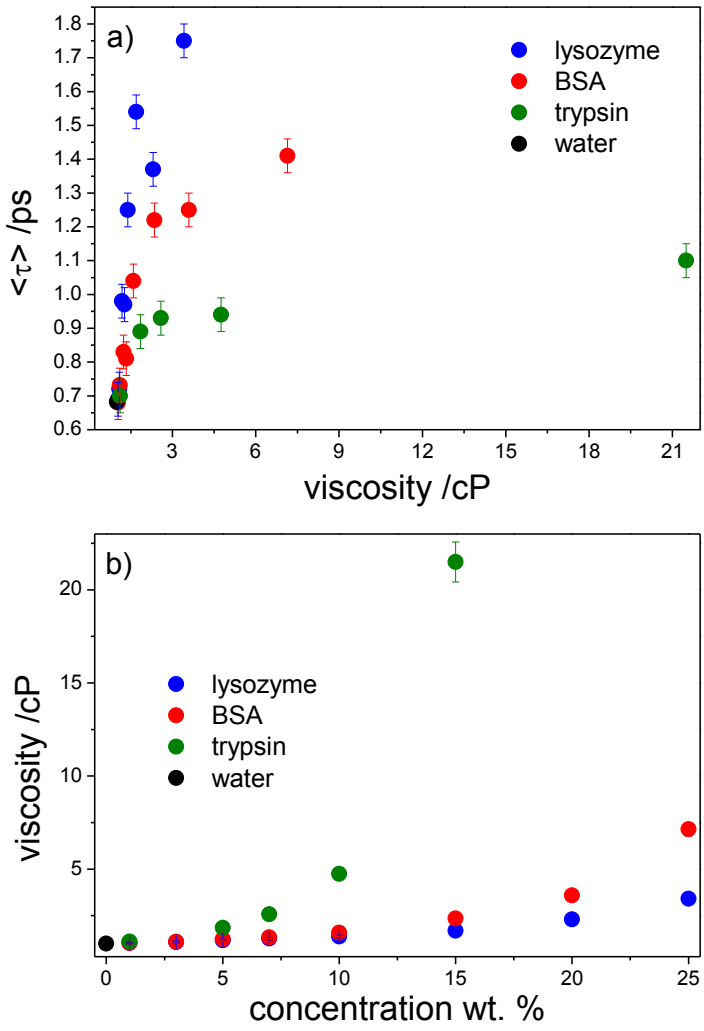

Figure 6.4 a) The dependence of average relaxation time on the solution viscosity, b) dependence of viscosity on the concentration.

6.3 Frequency Domain Analysis

The RSDs of the three proteins at different concentrations are shown in Figure 6.5. Prior to the Fourier transform all data were normalized to the intensity of the electronic response at t = 0 ps. Up to 5 wt. % the RSDs closely resemble that for pure water, characterized by two bands at ~45 cm^{-1} and ~175 cm^{-1}. For the purpose of the analysis of spectral line shapes, the RSDs were fitted with a sum of two (<5 wt. %) or three (>5 wt. %) lineshape functions (BL, ASG and G, see section 2.4.2). However, to accurately fit the more structured lysozyme spectra two more Gaussian functions were

added at concentrations >10 wt. %. The wavenumbers of these two extra components are 108 cm^{-1} and 160 cm^{-1} and are constant for the whole range of concentrations. Modes at approximately the same frequency were previously observed in the Raman spectra[32] of dry lysozyme crystals (at 114 cm^{-1} and 167 cm^{-1}) and were assigned to intramolecular modes. A spectrum of lysozyme (30 wt. %) with these five fitting

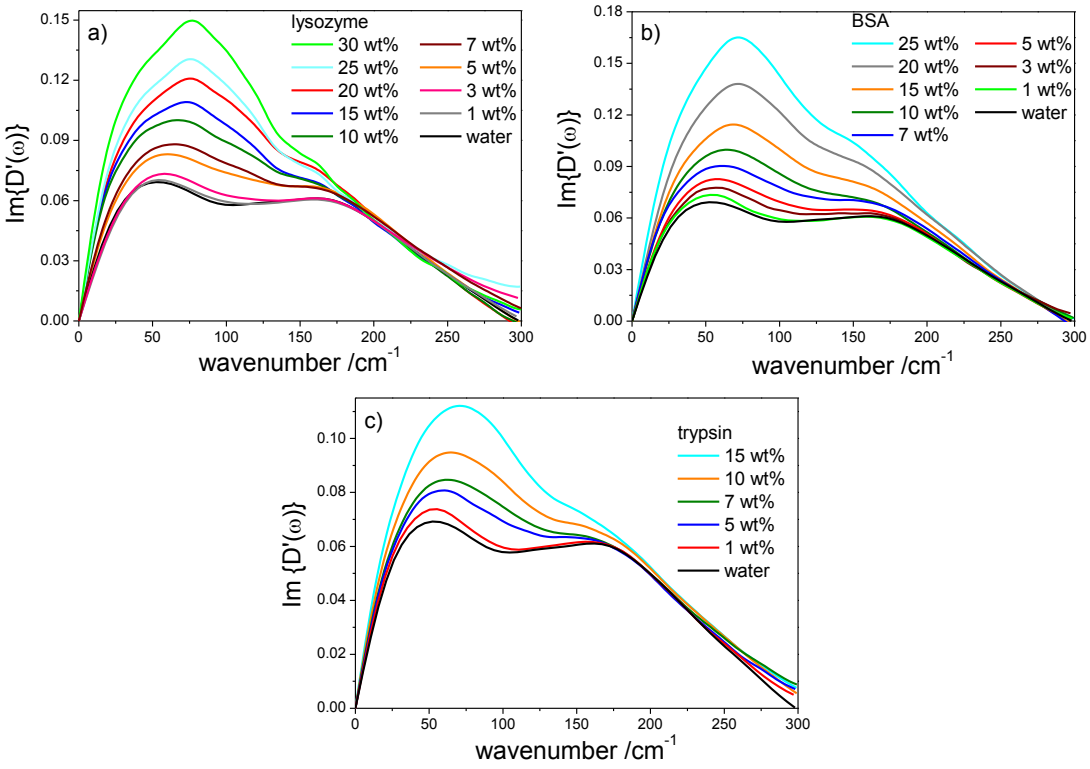

Figure 6.5 Evolution of RSD spectra of a) lysozyme, b) BSA and c) trypsin with concentration. Pure water is plotted in black.

functions is shown in Figure 6.6. The fitting parameters for all three protein solutions are listed in Tables 6.2-6.3 and the wavenumbers recovered are plotted in Figure 6.7.The integrated area relative weight was calculated using Eq. 4.7. There is only a slight shift of the BL mode towards higher frequencies with increasing concentration. However the fraction of the RSD assigned to BL increases significantly with increasing concentration. The increase in the relative amplitude at higher concentrations may be assigned to a contribution originating from protein modes in

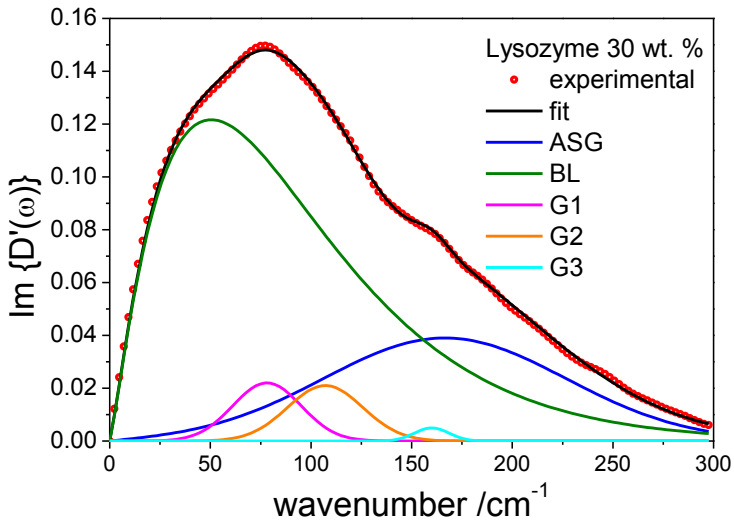

Figure 6.6 RSD of lysozyme 30 wt.% fitted with five functions: Bucaro-Litovitz (BL), antisymmetrized Gaussian (ASG) and Gaussian (G). The dotted line is the experimental data and the black line is a sum of three fitting functions.

conc. /wt. %	I_{BL}	α	ω_{BL} /cm^{-1}	I_G	ω_G /cm^{-1}	$\Delta\omega_G$ /cm^{-1}	I_{ASG}	ω_{ASG} /cm^{-1}	$\Delta\omega_{ASG}$ /cm^{-1}
BSA									
1	0.069	1.48	32.0	-	-	-	0.049	175.6	129.3
3	0.073	1.50	33.0	-	-	-	0.048	175.7	131.6
5	0.079	1.50	33.6	-	-	-	0.048	175.5	127.4
7	0.083	1.20	41.0	0.005	77.0	41.3	0.047	174.0	127.6
10	0.088	1.20	43.2	0.008	77.4	48.0	0.042	173.9	128.8
15	0.093	1.24	41.8	0.016	78.0	54.7	0.050	170.3	128.4
20	0.111	1.26	43.8	0.022	79.3	54.4	0.049	170.0	127.9
25	0.136	1.22	45.8	0.024	79.6	46.2	0.045	165.0	127.0
lysozyme									
1	0.065	1.44	33.5	-	-	-	0.048	176.0	132.8
3	0.065	1.43	34.6	-	-	-	0.047	176.0	143.0
5	0.074	1.23	40.2	0.005	75.2	57.2	0.048	174.0	131.0
7	0.076	1.23	39.1	0.007	76.0	45.9	0.047	174.0	143.0
10	0.091	1.20	40.0	0.008	75.8	40.0	0.044	177.0	120.6
15	0.093	1.20	40.0	0.012	77.4	40.0	0.043	172.6	136.5
20	0.101	1.20	41.1	0.020	76.3	40.0	0.044	174.0	122.7
25	0.104	1.20	41.0	0.020	77.0	40.0	0.042	174.0	143.0
30	0.121	1.20	42.0	0.021	78.1	40.0	0.039	166.4	141.8
trypsin									
1	0.068	1.45	31.7	-	-	-	0.050	174.9	135.7
5	0.073	1.45	33.8	-	-	-	0.047	173.6	146.2
7	0.072	1.25	39.1	0.005	78.1	46.5	0.044	174.3	153.5
10	0.082	1.30	38.9	0.008	78.9	49.6	0.045	175.2	146.2
15	0.088	1.26	40.0	0.016	80.0	52.5	0.045	168.1	158.5

Table 6.2 Parameters obtained from the fitting in the frequency domain.

conc. /wt. %	I_{G2}	ω_{G2} /cm^{-1}	$\Delta\omega_{G2}$ /cm^{-1}	I_{G3}	ω_{G3} /cm^{-1}	$\Delta\omega_{G3}$ /cm^{-1}
lysozyme						
7	0.02	105.3	37.0	-	-	-
10	0.01	109.3	60.0	-	-	-
15	0.01	108.8	42.9	0.003	161.4	25.8
25	0.02	106.7	54.2	0.004	160.1	24.8
25	0.02	108.0	45.0	0.005	160.0	20.0
30	0.02	107.0	43.9	0.005	160.0	20.0

Table 6.3 Additional two Gaussian components required to fit lysozyme at the concentration >7 wt. %.

this frequency region. Such solute modes were previously observed in formamide[33, 34] (chapter 4) and N-Methylacetamide[35] (NMA) which are model compounds for the protein amide backbone. However some other solutes, for example the iodide ion, are known to cause a shift of the water RSD to lower frequency.

Both the wavenumber and the relative weight of the ASG mode decrease with increasing concentration at >5wt% protein. In pure water this mode is associated with the collective water-water H-bond stretching motion, so this observation indicates a weakening or disruption of water-water hydrogen bonds by the protein. A weakening of the H-bond might be expected to lead to faster relaxation dynamics. However, this is not observed (Figure 6.1). Two factors may lead to this result. First, the collective mode disrupted by the solute is replaced by a stronger solute-solvent interaction. Second, Laage and Hynes[36] showed that geometric restrictions may slow water orientational dynamics by restricting the approach of the partner water required to allow the H-bond switch and associated orientational jump. Similar geometric or stronger solvent-solute interaction arguments may apply to the interaction induced dynamics reported by OKE, giving rise to the slower OHD-OKE response even though the characteristic signature of H-bonding is disrupted.

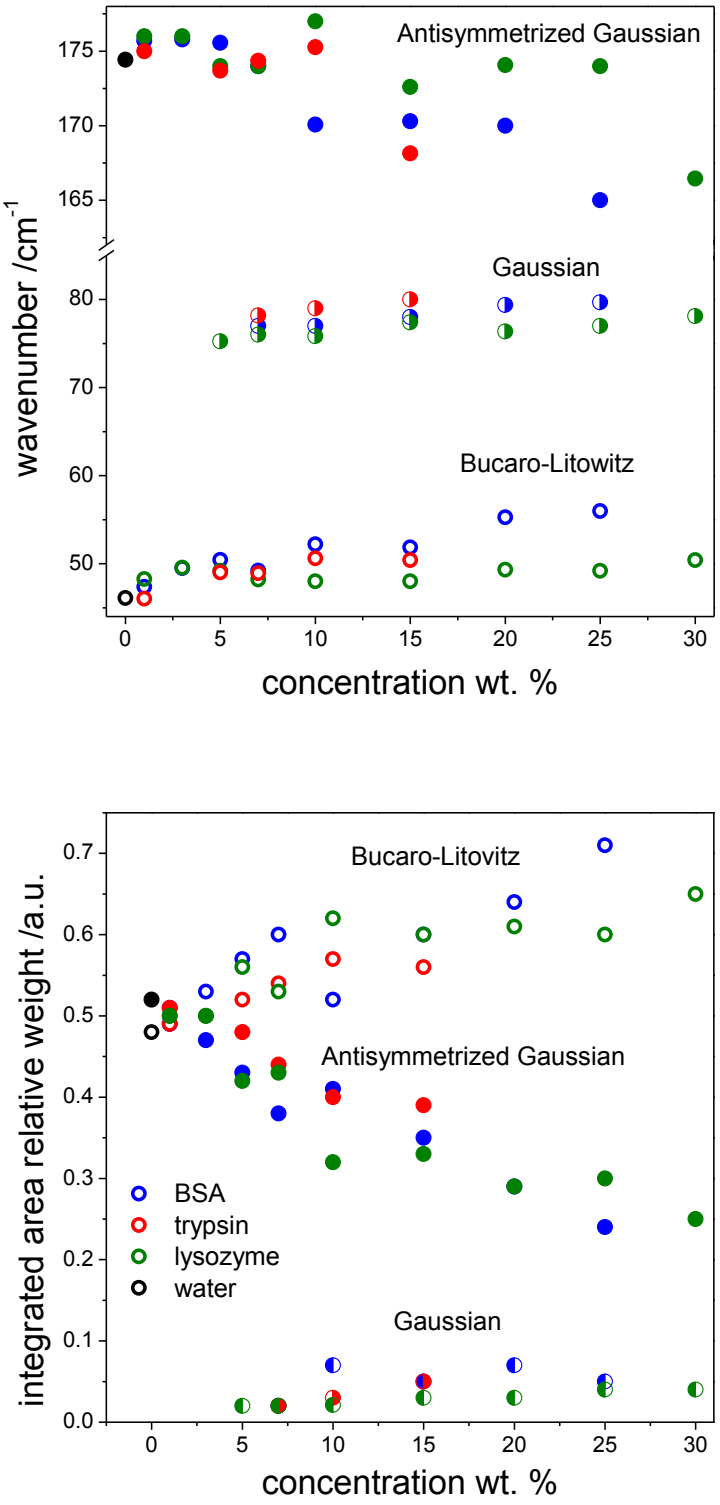

Figure 6.7 Parameters obtained from the fit of the Bucaro-Litovitz (open symbols), antisymmetrized Gaussian (filled symbols) and Gaussian line shape functions (half filled) to the protein RSD of BSA (blue), trypsin (red) and lysozyme (green) as a function of concentration. Error ±5 %.

The intermediate (G) component, which appears at concentrations above 5 wt.% was previously observed in peptides and small solutes (urea, formamide) and assigned to an out of plane bending of the H-bonded solute.[4, 31, 33] An ~80 cm^{-1} mode was also found in the aqueous protein solutions studied through various techniques and was assigned to protein backbone motion.[18, 37, 38] Low frequency Raman spectra of lysozyme crystals (water content 9 wt.%)[32] also exhibit a mode at 83 cm^{-1}. On this basis, and on the basis of our previous studies of small solutes and model peptides, we assign the G mode to a bending mode of H-bonded amino acids in the protein. Even though the three proteins studied differ in their size and structure, the frequency and relative weight of the G mode of each is comparable. This is as expected because the number of amino acid residues in each sample at the same weight fraction is similar. For example, in a 10 wt. % solution there are between $(6.3-6.7)\times10^{23}$ amino acids per litre of protein solution for BSA, lysozyme and trypsin. Therefore the appearance of this mode depends only on the amount of amino acid residues in the solution and not on the protein conformation.

6.4 Conclusions

Direct time domain OHD-OKE measurements on aqueous protein solutions were performed as a function of concentration. At low protein concentrations (below 5 wt. %) the H-bonded structure of water is mainly preserved. Further addition of protein leads to the gradual disruption of the water structure, as judged by the decrease in amplitude and frequency of the collective water-water stretching mode at 175 cm^{-1}. The picosecond relaxation times observed were associated with relaxation of the H-bond network in the solution, chapter 2. This relaxation time was observed to increase with increasing protein concentration. A simple two-state analysis allowed us to

estimate the effect of protein on water dynamics in the hydration shell. In all cases water molecules in the solvation shell of the protein exhibited slower dynamics relative to bulk water. The slowest dynamics were observed for BSA, which has the most hydrophilic surface. A somewhat smaller effect was observed for the most hydrophobic protein, trypsin. These data imply that all water molecules solvating the protein surface exhibit slower relaxations than in bulk, and that hydrophilic sites influence water dynamics in their vicinity to a greater extent than hydrophobic sites. The mode observed at ~80 cm^{-1} in more concentrated protein solutions was assigned to an out of plane bending mode of protein units.

6.5 References

1. Y. Levy and J. N. Onuchic, *Annu. Rev. Biophys. Biomol. Struct.*, 2006, **35**, 389-415.
2. J. A. Rupley and G. Careri, *Adv. Protein Chem.*, 1991, **41**, 37-172.
3. C. Malardier-Jugroot, M. E. Johnson, R. K. Murarka and T. Head-Gordon, *PCCP*, 2008, **10**, 4903-4908.
4. K. Mazur, I. A. Heisler and S. R. Meech, *J. Phys. Chem. B*, 2010, **114**, 10684-10691.
5. B. Born, H. Weingartner, E. Brundermann and M. Havenith, *J. Am. Chem. Soc.*, 2009, **131**, 3752-3755.
6. B. Halle, *Philosophical Transactions of the Royal Society of London Series B-Biological Sciences*, 2004, **359**, 1207-1223.
7. K. Modig, E. Liepinsh, G. Otting and B. Halle, *J. Am. Chem. Soc.*, 2004, **126**, 102-114.
8. J. Qvist, E. Persson, C. Mattea and B. Halle, *Faraday Discuss.*, 2009, **141**, 131-144.
9. M. Paolantoni, P. Sassi, A. Morresi and S. Santini, *J. Chem. Phys.*, 2007, **127**.
10. N. Nandi, K. Bhattacharyya and B. Bagchi, *Chem. Rev.*, 2000, **100**, 2013-2045.
11. A. R. Bizzarri, C. X. Wang, W. Z. Chen and S. Cannistraro, *Chem. Phys.*, 1995, **201**, 463-472.
12. I. D. Kuntz and W. Kauzmann, *Adv. Protein Chem.*, 1974, **28**, 239-345.
13. A. R. Bizzarri and S. Cannistraro, *J. Phys. Chem. B*, 2002, **106**, 6617-6633.
14. S. Ebbinghaus, S. J. Kim, M. Heyden, X. Yu, U. Heugen, M. Gruebele, D. M. Leitner and M. Havenith, *P. Natl. Acad. Sci. USA*, 2007, **104**, 20749-20752.
15. J. Xu, K. W. Plaxco and S. J. Allen, *J. Phys. Chem. B*, 2006, **110**, 24255-24259.

16. N. T. Hunt, L. Kattner, R. P. Shanks and K. Wynne, *J. Am. Chem. Soc.*, 2007, **129**, 3168-3172.
17. T. L. James, G. B. Matson and I. D. Kuntz, *J. Am. Chem. Soc.*, 1978, **100**, 3590-3594.
18. J. D. Eaves, C. J. Fecko, A. L. Stevens, P. Peng and A. Tokmakoff, *Chem. Phys. Lett.*, 2003, **376**, 20-25.
19. B. Lee, *Proceedings of the National Academy of Sciences of the United States of America-Physical Sciences*, 1983, **80**, 622-626.
20. M. Marchi, F. Sterpone and M. Ceccarelli, *J. Am. Chem. Soc.*, 2002, **124**, 6787-6791.
21. A. Rejoumichel, F. Henry, M. Devillardi and M. Delmotte, *Physics in Medicine and Biology*, 1985, **30**, 831-837.
22. A. Lerbret, F. Affouard, P. Bordat, A. Hedoux, Y. Guinet and M. Descamps, *J. Chem. Phys.*, 2009, **131**.
23. K. Yokoyama, T. Kamei, H. Minami and M. Suzuki, *J. Phys. Chem. B*, 2001, **105**, 12622-12627.
24. S. Perticaroli, L. Comez, M. Paolantoni, P. Sassi, L. Lupi, D. Fioretto, A. Paciaroni and A. Morresi, *J. Phys. Chem. B*, 2010, **114**, 8262-8269.
25. A. Mahn and J. A. Asenjo, *Biotechnol. Adv.*, 2005, **23**, 359-368.
26. K. O. Eriksson, A. S. Naidu, F. Kilar, T. Wadstrom and S. Hjerten, *Apmis*, 1989, **97**, 1081-1087.
27. A. Kato and S. Nakai, *Biochim. Biophys. Acta*, 1980, **624**, 13-20.
28. Y. U. Moon, R. A. Curtis, C. O. Anderson, H. W. Blanch and J. M. Prausnitz, *J. Solution Chem.*, 2000, **29**, 699-717.
29. B. Lee and F. M. Richards, *J. Mol. Biol.*, 1971, **55**, 379-&.
30. L. C. de Morais, R. Bernardes and O. Assis, *World Journal of Microbiology & Biotechnology*, 2009, **25**, 123-129.
31. K. Mazur, I. A. Heisler and S. R. Meech, *J. Phys. Chem. B*, 2011, **115**, 2563-2573.
32. H. Urabe, Y. Sugawara, M. Ataka and A. Rupprecht, *Biophys. J.*, 1998, **74**, 1533-1540.
33. O. F. Nielsen, P. A. Lund and E. Praestgaard, *J. Chem. Phys.*, 1982, **77**, 3878-3883.
34. Y. J. Chang and E. W. Castner, *J. Chem. Phys.*, 1993, **99**, 113-125.
35. N. T. Hunt, A. R. Turner, H. Tanaka and K. Wynne, *J. Phys. Chem. B*, 2007, **111**, 9634-9643.
36. D. Laage, G. Stirnemann and J. T. Hynes, *J Phys Chem* 2009, **113**, 2428-2435.
37. G. Giraud, J. Karolin and K. Wynne, *Biophys. J.*, 2003, **85**, 1903-1913.
38. S. E. M. Colaianni and O. F. Nielsen, *J. Mol. Struct.*, 1995, **347**, 267-283.

Chapter 7

Conclusions and further work

In this thesis, we have considered the ultrafast dynamics of of aqueous solutions. The nature of the solutes studied span from simple ions to complex proteins. The main goal was to establish what effect these various solutes have on the water dynamics in their solvation shell.

We studied a series of aqueous alkali halide solutions at wide range of concentrations and revealed a low frequency polarised anion-water mode. With the help of DFT calculations it was established that this mode originates from the symmetric stretch of an ion-water H-bond of asymmetrically solvated ion. This mode was found to shift to a higher frequency with increasing salt concentration. It was suggested that the observed shift might be due to the effect of the electric field of the cation on the intermolecular H-bond stretch. The anisotropic measurement revealed that the iodide ion disrupt the water structure to a greater extent than the smaller chloride.

The effect of hydrophilic and hydrophobic solutes on the dynamics of water was considered next. Two different concentrations regions were observed. At low concentration, below 0.5M for peptides, UA, FA, TMAO, TBA, TMU and below 5 wt. % for proteins the tetrahedral structure of water was largely preserved. The averaged relaxation time reflects slower dynamics than in the solvation water than in the bulk. We applied a two-state model to assess the relaxation time of water

molecules in the hydration shells of solutes at these low concentrations. It was shown that the hydrophilic solutes slow down the water dynamics to a greater extent than hydrophobic ones. This trend was observed for all aqueous solutions studied. The retardation factor of slow water to bulk water recovered gave values between two for the hydrophobic TMAO and 20 for the most hydrophilic peptide. However the retardation factor depends on the assumption of how many hydration shells are affected by the solute. A hydration shell extending beyond one layer results in a smaller retardation factor.

We tried to estimate the number of water molecules in the effective solvation shell by calculating the integrated areas under the picosecond response. We found a large variation in the number of water molecules between the lowest concentration and the 5 wt. % for proteins and 0.5 for other solutions. However from the results obtained it seems likely that the solutes infuence the water dynamics beyond first hydration shell. To improve this evaluation a more detailed analysis of the non-single exponential relaxation dynamics is needed. Also the present determination of an average relaxation time masks the potentially different dynamics associated with different hydration shells. To do this the OKE traces have to be recorded with very good signal to noise ratio, such that they can reliably be analysed with more complex models.

Studies of high concentrations of UA, FA, peptides and proteins revealed a new mode at ~ 80 cm^{-1} in the spectral densities. This mode was associated with the out of plane bending of the H-bonded solute. The spectral densities of TMAO unexpectedly resembled that of bulk water over the whole range of concentration studied. This inicates that the tetrahedral structure of water is retained on addition of TMAO. A similar result was obtained for TBA at room temperature. This may indicate clustering of water in these systems so that they are microscopically inhomogeneous.

The spectral densities of TMAO spectra at different temperature also exhibit behaviour similar to that observed in bulk water. Both of the low frequency modes characteristic of bulk water shift to the lower frequency with increasing temperature and the contribution of the higher frequency one to the spectral density grows with increasing temperature. The temperature dependent studies of TBA showed that the spectral density was more sensitive to increasing temperature than that of TMAO. This was assigned to disaggregation on temperature elevation.

Based on this observation, a number of future areas of studies may prove interesting. The measurement of protein solution with high signal to noise ratio to establish the number of water molecules affected by a single biomolecule. This would require the study of a range of proteins with different surface exposed groups. These studies may extend to a disordered proteins, sugars and DNA.

Further measurement of various salt solutions should be performed using the diffrative optic TG-OKE method (*e.g.* K_3PO_4) to reveal new low frequency modes. These studies might help to establish the precise effect of counterions on the observed low frequency modes.

Appendix A. LabVIEW programs:

Appendix A contains the LabVIEW programs used to analyze the data.

1. Evolutionary fitting program to the time domain data
2. Evolutionary fitting program to the frequency domain data
3. Program for saving fitting components in the time domain
4. Program for saving fitting components in the frequency domain
5. Spectrum generation via a Fourier transform

Programs with accompanied subVIs are included on CD.

Appendix B. Gaussian output files :

CD contains Gaussian output files (.log) with frequencies calculated for studied molecules. Calculations were performed for single molecules and dimers, as well as molecule-water complexes.

1. Chapter 3:

   Br^-, Cl^-

2. Chapetr 4:

   UA, FA, TMAO, TMU and TBA

3. Chapter 5:

   NAGMA, NAAMA, NALMA

Publications:

1. Yamaguchi, S.; **Mazur, K**.; Heisler, I.A.; Shirota, H.; Tominaga, K.; Meech, S.R.; 2011, *Low-frequency Modes of Benzoic Acid Dimer in Chloroform Observed by the Optical Kerr Effect*, Journal of Chemical Physics, 135, 134504
2. **Mazur, K.;** Heisler, I.A.; Meech, S.R.; 2011, *Water dynamics at protein interfaces: Ultrafast Optical Kerr effect study*, Journal of Physical Chemistry A, DOI: 10.1021/jp2074539
3. Heisler, I.A.; **Mazur, K**.; Yamaguchi, S.; Tominaga, K.; Meech, S.R.; 2011, *Measuring acetic acid dimer modes by ultrafast time-domain Raman spectroscopy*, Physical Chemistry Chemical Physics, 13, 15573-15579
4. Heisler, I.A; **Mazur, K.;** Meech, S.R.; 2011, *Hydroxide hydrogen bonding: probing the solvation structure through ultrafast time-domain Raman spectroscopy*, Journal of Physical Chemistry Letters, 2, 1155-1160.
5. **Mazur, K**.; Heisler, I.A.; Meech, S.R.; 2011, *THz Spectra and Dynamics of Aqueous Solutions Studied by the Ultrafast Optical Kerr Effect*, Journal of Physical Chemistry B, 115, 2563-2573.
6. Heisler, I.A.; **Mazur, K.;** Meech, S.R.; 2011, *Low-Frequency Modes of Aqueous Alkali Halide Solutions: An Ultrafast Optical Kerr Effect Study*, Journal of Physical Chemistry B, 115, 1863-1873.
7. **Mazur, K.;** Heisler, I.A.; Meech, S.R.; 2010, *Ultrafast Dynamics and Hydrogen-Bond Structure in Aqueous Solutions of Model Peptides*, Journal of Physical Chemistry B, 114, 10684-10691.